

JOINT SERVICES ELECTRONICS PROGRAM

Seventeenth Annual Report Appendix

The Ohio State University
ElectroScience Laboratory

Department of Electrical Engineering
Columbus, Ohio 43212

This document has been approved
for public release and sale; its
distribution is unlimited.

Annual Report Appendix 721563-7
Contract No. N00014-89-J-1007
November 1994

Department of the Navy
Office of Naval Research
800 North Quincy Street
Arlington, Virginia 22217

DTIC QUALITY ENHANCED 3

19950106 088

NOTICES

When Government drawings, specifications, or other data are used for any purpose other than in connection with a definitely related Government procurement operation, the United States Government thereby incurs no responsibility nor any obligation whatsoever, and the fact that the Government may have formulated, furnished, or in any way supplied the said drawings, specifications, or other data, is not to be regarded by implication or otherwise as in any manner licensing the holder or any other person or corporation, or conveying any rights or permission to manufacture, use, or sell any patented invention that may in any way be related thereto.

REPORT DOCUMENTATION PAGE

*Form Approved
OMB No. 0704-0188*

Public reporting burden for this collection of information is estimated to average 1 hour per response, including the time for reviewing instructions, searching existing data sources, gathering and maintaining the data needed, and completing and reviewing the collection of information. Send comments regarding this burden estimate or any other aspect of this collection of information, including suggestions for reducing this burden, to Washington Headquarters Services, Directorate for Information Operations and Reports, 1215 Jefferson Davis Highway, Suite 1204, Arlington, VA 22202-4302, and to the Office of Management and Budget, Paperwork Reduction Project (0704-0188), Washington, DC 20503.

1. AGENCY USE ONLY (Leave blank)			2. REPORT DATE November 1994		3. REPORT TYPE AND DATES COVERED Annual Report Appendix - Sept. 1993 thru Sept. 1994	
4. TITLE AND SUBTITLE Joint Services Electronics Program - Seventeenth Annual Report Appendix			5. FUNDING NUMBERS N00014-89-J-1007			
6. AUTHOR(S)						
7. PERFORMING ORGANIZATION NAME(S) AND ADDRESS(ES) The Ohio State University ElectroScience Laboratory 1320 Kinnear Road Columbus, Ohio 43212			8. PERFORMING ORGANIZATION REPORT NUMBER 721563-7 Appendix			
9. SPONSORING / MONITORING AGENCY NAME(S) AND ADDRESS(ES) Department of the Navy Office of Naval Research 800 North Quincy Street Arlington, Virginia 22217			10. SPONSORING / MONITORING AGENCY REPORT NUMBER			
11. SUPPLEMENTARY NOTES						
12a. DISTRIBUTION / AVAILABILITY STATEMENT A. Approved for public release; Distribution is unlimited.				12b. DISTRIBUTION CODE		
13. ABSTRACT (Maximum 200 words)						
14. SUBJECT TERMS					15. NUMBER OF PAGES 79	
					16. PRICE CODE	
17. SECURITY CLASSIFICATION OF REPORT UNCLASSIFIED	18. SECURITY CLASSIFICATION OF THIS PAGE UNCLASSIFIED	19. SECURITY CLASSIFICATION OF ABSTRACT UNCLASSIFIED	20. LIMITATION OF ABSTRACT			

Contents

SECTION	PAGE
INTRODUCTION	1
JSEP REFEREED JOURNAL PAPERS PUBLISHED SEPTEMBER 1993 TO SEPTEMBER 1994	2
JSEP RELATED REFEREED JOURNAL PAPERS ACCEPTED FOR PUBLICATION SEPTEMBER 1993 TO SEPTEMBER 1994	3
JSEP RELATED PAPERS SUBMITTED FOR PUBLICATION SEPTEMBER 1993 TO SEPTEMBER 1994	4
JSEP RELATED PAPERS IN PREPARATION FOR PUBLICATION SEPTEMBER 1993 TO SEPTEMBER 1994	5
JSEP RELATED CONFERENCES/ORAL PRESENTATIONS SEPTEMBER 1993 TO SEPTEMBER 1994	7
JSEP RELATED AWARDS, PH.D. DISSERTATIONS AND M.SC. THESES SEPTEMBER 1993 TO SEPTEMBER 1994	8
REPRINTS JSEP REFEREED JOURNAL PAPERS PUBLISHED SEPTEMBER 1993 TO SEPTEMBER 1994	9

Accession For	
NTIS	CRA&I
DTIC	TAB
Unannounced	
Justification	
By	
Date Entered	
Area	Code
Disc	Area
A-1	

INTRODUCTION

This Appendix contains the reprints published under JSEP in the time September 1993 to September 1994.

In addition to the 8 reprints contained herein, there are 10 papers already accepted for publication during the next contract period, 12 papers submitted and 10 papers in preparation.

JSEP REFEREED JOURNAL PAPERS
PUBLISHED SEPTEMBER 1993 TO SEPTEMBER 1994

1. G.A. Somers and P.H. Pathak, "Efficient Numerical and Closed Form Asymptotic Representations of the Dyadic Aperture Green's Function for Material Coated Ground Planes," *Radio Science*, vol. 29, pp. 465-481, March-April 1994.
2. H.C. Ly and R.G. Rojas, "EM Plane Wave Diffraction by a Material Coated Perfectly Conducting Half-Plane—Oblique Incidence," *Microwave and Optical Technology Letters*, vol. 7, no. 6, pp. 262-266, April 1994.
3. R. Torres and E.H. Newman, "Integral Equation Analysis of a Sheet Impedance Coated Window Slot Antenna," *IEEE Transactions on Antennas and Propagation*, vol. 42, pp. 541-544, April 1994.
4. J.L. Blanchard, E.H. Newman and M.E. Peters, "Integral Equation Analysis of Artificial Media," *IEEE Transactions on Antennas and Propagation*, vol. 42, pp. 727-731, May 1994.
5. R. Lee and V. Chupongstimun, "A Partitioning Technique for the Finite Element Solution of Electromagnetic Scattering from Electrically Large Dielectric Cylinders," *IEEE Transactions on Antennas and Propagation*, vol. 42, pp. 737-741, May 1994.
6. R. Lee and T.T. Chia, "Analysis of Electromagnetic Scattering from a Cavity with a Complex Termination by Means of a Hybrid Ray-FDTD Method," *IEEE Transactions on Antennas and Propagation*, vol. 41, pp. 1560-1569, November 1993.
7. J.O. Jevtic and R. Lee, "On the Choice of Metrons in the MEI Method," *COMPEL — Int. Journal Comp. and Math. in Electrical and Electronic Eng.*, vol. 13, Supplement A, pp. 217-222, 1994.
8. J.O. Jevtic and R. Lee, "A Theoretical and Numerical Analysis of the Measured Equation of Invariance," *IEEE Transactions on Antennas and Propagation*, vol. 42, pp. 1097-1105, August 1994.

**JSEP RELATED REFERRED JOURNAL PAPERS
ACCEPTED FOR PUBLICATION
SEPTEMBER 1993 TO SEPTEMBER 1994**

1. U. Pekel and R. Lee, "An A Posteriori Error Reduction Scheme for the Three Dimensional Finite Element Solution of Maxwell's Equations," *IEEE Trans. Microwave Theory and Techniques*.
2. M.E. Peters and E.H. Newman, "Method of Moments Analysis of Anisotropic Artificial Media Composed of Dielectric Wire Objects," *IEEE Transactions on Microwave Theory and Techniques*.
3. L.M. Chou, R.G. Rojas and P.H. Pathak, "WH/GSMT Based Full-Wave Analysis of Planar Transmission Lines Embedded in Multilayered Dielectric Substrates," *IEEE Trans. on Microwave Theory and Techniques*.
4. R.G. Rojas, "Integral Equations for the EM Scattering by Homogeneous/Inhomogeneous Two Dimensional Chiral Bodies," *IEE Proceedings-H*.
5. M.F. Otero and R.G. Rojas, "Synthesis of the Frequency Response of an Inhomogeneous Resistive Strip," *Annales of Telecommunications*, Special Issue on Radar Cross Section.
6. H.T. Anastassiou and P.H. Pathak, "High Frequency Analysis of Gaussian Beam Scattering by a Two-Dimensional Parabolic Contour of Finite Width," *Radio Science*.
7. P. Munk and P.H. Pathak, "EM Scattering by a Dielectric Filled Rectangular Antenna Cavity Recessed in a Ground Plane and Backed with an Array of Loaded Dominant Mode Waveguides," *IEEE Transactions on Antennas and Propagation*.
8. P. Munk and P.H. Pathak, "A Useful Approximate Analysis of the EM Scattering by a Rectangular Antenna Cavity containing an Array of Dominant Mode Waveguide Loaded Slots," *Journal of EM Waves and Applications*, (special issue on EM Scattering).
9. P. Rousseau and R.J. Burkholder, "A Hybrid Approach for Calculating the Scattering from Obstacles within Large Open Cavities," *IEEE Transactions on Antennas and Propagation*.
10. W.P. Pinello, R. Lee and A.C. Cangellaris, "Finite Element Modeling of Electromagnetic Wave Interactions with Periodic Structures," *IEEE Trans. Microwave Theory and Techniques*.

**JSEP RELATED PAPERS
SUBMITTED FOR PUBLICATION
SEPTEMBER 1993 TO SEPTEMBER 1994**

1. T.T. Chia, R.J. Burkholder and R. Lee, "The Application of FDTD in Hybrid Methods for Cavity Scattering Analysis," submitted to *IEEE Trans. Antennas and Propagat.*
2. T.L. Barkdoll and R. Lee, "Finite Element Analysis of Bodies of Revolution using the Measured Equation of Invariance," submitted to *Radio Science*.
3. J.O. Jevtic and R. Lee, "The Relationship Between the Reflection Coefficient and the Error for Absorbing Boundary Conditions," submitted to *Electromagnetics*.
4. J.O. Jevtic and R. Lee, "An Investigation of the Convergence Properties of the Measured Equation of Invariance," submitted to *IEEE Transactions on Antennas and Propagation*.
5. J.O. Jevtic and R. Lee, "How Invariant is the Measured Equation of Invariance?" submitted to *IEEE Microwave and Guided Wave Letters*.
6. Y.S. Choi-Grogan, K. Eswar, P. Sadayappan and R. Lee, "Sequential and Parallel Implementations of a Partitioning Finite Element Method," submitted to *IEEE Transactions on Antennas and Propagation*.
7. U. Pekel and R. Lee, "A 3-D Application of the Bymoment Method for Electromagnetic Scattering," submitted to *Journal of Electromagnetic Waves and Application*.
8. E.H. Newman and M. Kragalott, "Moment Method Analysis of the Electric Shielding Factor of a Conducting TM Shield at ELF," submitted to *IEEE Trans. on Electromagnetic Compatibility*.
9. L.M. Chou and R.G. Rojas, "Dispersion and Lateral Leakage of Conductor Backed Coplanar Waveguides with Layered Substrate and Finite-Extent Lateral Ground Planes," submitted to *IEEE Transactions on Microwave Theory and Techniques*.
10. P. Rousseau and P.H. Pathak, "Time Domain Uniform Geometrical Theory of Diffraction (TD-UTD) for a Curved Wedge," submitted to *IEEE Transactions on Antennas and Propagation*.
11. F. Obelleiro, J.L. Rodriguez and R.J. Burkholder, "An Iterative Physical Optics Approach for Analyzing the Electromagnetic Scattering by Large Open-Ended Cavities," submitted to *IEEE Transactions on Antennas and Propagation*.
12. P.H. Pathak, H.T. Chou and R.J. Burkholder, "Ray Like Gaussian Basis Functions for Analyzing Propagation into and Scattering from Large Open Cavities with the GRE."

**JSEP RELATED PAPERS
IN PREPARATION FOR PUBLICATION
SEPTEMBER 1993 TO SEPTEMBER 1994**

1. J.O. Jevtic and R. Lee, "Techniques for Improving the Accuracy of the Measured Equation of Invariance," in preparation to be submitted to *Journal of Electromagnetic Waves and Application*.
2. R.G. Rojas, "Generalized Impedance/Resistive Boundary Conditions for a Planar Homogeneous Chiral Slab."
3. M.F. Otero and R.G. Rojas, "Two Dimensional Green's Function for an Impedance Wedge."
4. M.F. Otero and R.G. Rojas, "Scattering of a Complex Material Body of Arbitrary Shape in the Presence of an Impedance Wedge."
5. Y.M. Hwang, R.G. Kouyoumjian and M. Hsu, "Asymptotic Analysis of the Scattering by a Wedge Illuminated by a Field with a Rapid Spatial Variation."
6. R.J. Burkholder and P.H. Pathak, "A Generalized Ray Expansion for Computing the EM Fields Radiated by an Antenna in a Complex Environment."
7. M. Hsu, P.H. Pathak and C.W. Chuang, "Analysis of the Asymptotic HF EM Coupling Between Sources Anywhere in the Vicinity of a Circular Cylinder."
8. P.H. Pathak, R.J. Burkholder and P. Rousseau, "On the Question of Causality Associated with the Inversion into Time Domain of Ray Fields that Pass Through Caustics."
9. G. Zogbi, R.J. Burkholder and P.H. Pathak, "An Efficient Planar Antenna Near and Far Field Analysis using Gaussian Aperture Elements."
10. P.H. Pathak, A. Nagamune and R.G. Kouyoumjian, "An Analysis of Compact Range Measurements."

JSEP RELATED CONFERENCES/ORAL PRESENTATIONS
SEPTEMBER 1993 TO SEPTEMBER 1994

1. Y.S. Choi-Grogan, R. Lee, K. Eswar and P. Sadayappan, "The Performance of a Partitioning Finite Element Method on the Touchstone Delta," accepted to the 10th Annual Review of Progress in Applied Computational Electromagnetics, Monterey, CA, March 1994.
2. A. Bataineh, R. Lee and F. Ozguner, "Electrical Characterization of High-Speed Interconnects with a Parallel Three-Dimensional Finite Difference Time-Domain Algorithm," High Performance Computing '94, Lojolla, California, April 1994.
3. M.F. Otero and R.G. Rojas, "Radiation/Scattering of Complex Material Body of Arbitrary Shape in the Presence of a Material Loaded Impedance Wedge," IEEE APS/URSI International Symposium, Seattle, Washington, June 1994.
4. R.G. Kouyoumjian, "Roger and Me," IEEE APS/URSI International Symposium, Seattle, Washington, June 1994.
5. P.R. Rousseau and P.H. Pathak, "Time Domain Version of the UTD for a Curved Wedge," IEEE APS/URSI International Symposium, Seattle, Washington, June 1994.
6. C.H. Chuang, P.H. Pathak and R.J. Burkholder, "Hybrid Analysis of EM Scattering by Large Open Cavities including Effects of Aperture Shape and Interior Obstacle," IEEE APS/URSI International Symposium, Seattle, Washington, June 1994.
7. E.H. Newman and I. Tekin, "An Overview of the Method of Moments Analysis of Large Systems," Board of Mathematical Sciences National Research Council Symposium on Large-Scale Structures in Acoustics and Electromagnetics, National Academy of Sciences, Washington, DC, September 26-27, 1994.
8. M. Hsu and P.H. Pathak, "Hybrid Analysis (MM-UTD) of EM Scattering by Finned Objects," IEEE APS/URSI International Symposium, Seattle, Washington, June 1994.
9. R.J. Burkholder, "A Progressive Physical Optics Algorithm for Computing the EM Scattering by Jet Inlet Cavities," IEEE APS/URSI International Symposium, Seattle, Washington, June 1994.
10. G. Manara, P. Nepa and R.G. Kouyoumjian, "Three Dimensional Solution for the Diffraction of an Inhomogeneous Plane Wave by a Wedge," IEEE APS/URSI International Symposium, Seattle, Washington, June 1994.
11. M. Hsu, P.H. Pathak and H. Tseng, "Hybrid (MM-UTD) Analysis of EM Scattering by Large Convex Objects with Appendages," Applied Computational Electromagnetics Society (ACES) Conference, Monterey, CA, March 1994.

12. R.J. Burkholder, P.R. Rousseau and P.H. Pathak, "A Hybrid Approach for Computing the EM Scattering from Complex Terminations Inside Large Open Cavities," Applied Computational Electromagnetics Society (ACES) Conference, Monterey, CA, March 1994.
13. G. Zogbi, H.T. Chou and P.H. Pathak, "Reflection and Transmission of Well Focussed General Astigmatic EM Gaussian Beams," International Symposium on Electromagnetic Environments and Consequences, EURO EM (NEM/HPEM)'94, Bordeaux, France, May-June 1994. (Invited)
14. P.R. Rousseau and P.H. Pathak, "Development of TD-UTD and Its Modifications for Analyzing the Transient Scattering from Curved Wedge Configurations," 5th Symposium on Mathematical Methods in Electromagnetic Theory (MMET*94), Kharkov, Ukraine, September 1994. (Invited)
15. J.O. Jevtic and R. Lee, "On the Choice of Metrons in the MEI Method," 2nd Workshop on Finite Element Methods in Electromagnetic Wave Problems, Siena, Italy, May 1994.
16. R. Lee and J.O. Jevtic, "Several Approaches to Improving the Solution in the Measured Equation of Invariance," Joint AP-S Symposium and URSI Radio Science Meeting, Seattle, WA, June 1994. (Invited)
17. T.T. Chia, R.J. Burkholder and R. Lee, "Implementing the Hybrid Ray-FDTD Method for Computing the RCS of 3-D Open-Ended Waveguide Cavities," Joint AP-S Symposium and URSI Radio Science Meeting, Seattle, WA, June 1994.
18. U. Pekel and R. Lee, "A Three-Dimensional Bymoment Method Approach for the Analysis of Electromagnetic Scattering," Joint AP-S Symposium and URSI Radio Science Meeting, Seattle, WA, June 1994.

**JSEP RELATED AWARDS, PH.D. DISSERTATIONS AND M.SC. THESES
SEPTEMBER 1993 TO SEPTEMBER 1994**

Awards:

1. L.M. Chou, 1993 ESL Best Dissertation Award, "A Novel Hybrid Full-Wave Analysis Method for Planar Transmission Lines Embedded in Multilayered Dielectrics — The WH/GSMT," Supervisor: R.G. Rojas.
2. Prof. Pathak has received the 1994 Lumley Research Award from the College of Engineering at The Ohio State University. This award is based on the previous four years of work.

Dissertations:

1. George Zogbi, "Reflection and Diffraction of General Astigmatic Gaussian Beams from Curved Surfaces and Edges," June 1994.
2. Tse-Tong Chia, "Application of FDTD in Hybrid Methods for EM Scattering Analysis of Cavities with Complex Terminations," June 1994.
3. M.E. Peters, "Method of Moments Analysis of Anisotropic Artificial Media Composed of Dielectric Wire Objects," March 1994.

Theses:

1. Ty Barkdoll, "Finite Element Analysis of Bodies of Revolution using MEI Boundary Conditions," September 1993.
2. Yung Shirley Choi-Grogan, "A Sequential and Parallel Implementation of a Partitioning Finite Element Technique for Electromagnetic Problems," December 1993.
3. Jovan Jevtic, "An Analysis of the Measured Equation of Invariance," May 1994.

**REPRINTS
JSEP REFEREED JOURNAL PAPERS
SEPTEMBER 1993 TO SEPTEMBER 1994**

Efficient numerical and closed-form asymptotic representations of the dyadic aperture Green's function for material-coated ground planes

Gary A. Somers

Lincoln Laboratory, Massachusetts Institute of Technology, Lexington

Prabhakar H. Pathak

The Ohio State University, ElectroScience Laboratory, Columbus

Abstract. This paper provides both numerical and closed-form uniform asymptotic representations of the aperture Green's function which determines the magnetic field due to a point magnetic current source where both the source and field points lie on the ground plane which is covered by a planar material slab. The closed-form asymptotic representation which explicitly contains effects of space, surface, and leaky waves is shown to agree with the numerical evaluation of the exact integral representation for source and field point separations which are only a few tenths of a free space wavelength. An extended envelope extraction technique allows an efficient evaluation of the exact integral representation for source and observation separations too small for the asymptotic solution to be valid. The asymptotic solution is uniform in that it remains valid across all of the relevant surface and leaky wave transition regions. The computation time for this asymptotic result is 2-3 orders of magnitude faster than the numerical evaluation of the exact integral form, and additionally its computation time is independent of the source and field point separations. This aperture Green's function is very useful when computing the mutual coupling elements of the method of moments admittance matrix for an array of slots in a material covered ground plane.

1. INTRODUCTION

There is increasing interest in analyzing electrically large antennas that are embedded in a material coating. A large array of slots in a material-coated ground plane fall into this category. When using an integral equation formulation for the surface field, which is solved via the method of moments (MM), it is necessary to calculate the mutual coupling between all of the slots in the array. These mutual coupling calculations typically involve Sommerfeld integrals whose brute force numerical evaluation can be a formidable task especially when the slots are separated by large electrical distances. In this paper, two very efficient representations of the dyadic aperture Green's function are presented which facilitates these mutual admittance calculations that otherwise might have been intractable for

large arrays. The numerical solution implemented here complements the closed form uniform asymptotic solution in that it is accurate and efficient in the small region surrounding the source point where the asymptotic solution fails. Additionally, the numerical solution serves as a reference solution for the asymptotic formulation. These solutions are useful for analyzing slots in a ground plane which are excited by striplines (or other waveguiding structures) in multilayered substrates below the ground plane.

The aperture dyadic Green's function presented here provides the magnetic fields on a ground plane with a material coating caused by a unit magnetic current point source which is also on the ground plane as shown in Figure 1. It is assumed that the ground plane is a perfect electric conductor (PEC), and the material coating is isotropic and homogeneous. It is also assumed that the material above the slab is free space. Recently, there has been activity in the related area of calculating the electric current/electric field Green's function, where both the

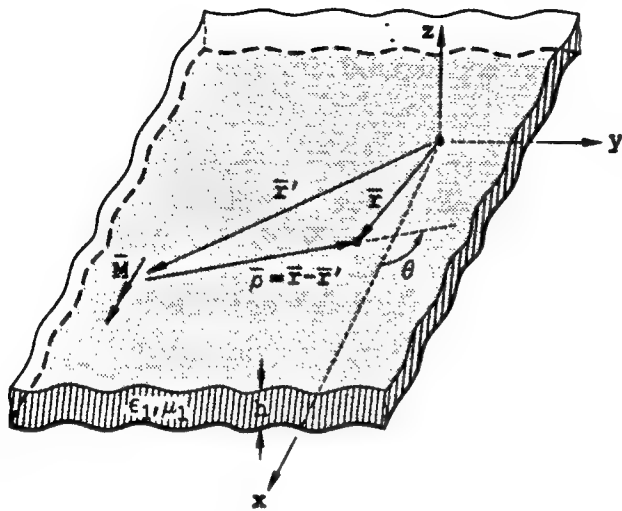


Figure 1. Material-coated ground plane with magnetic current, \bar{M} , at \bar{r}' and observation point at \bar{r} .

source and observation points are on the material-air interface of the grounded planar material slab [Barkeshli *et al.*, 1990; Marin *et al.*, 1989; Marin and Pathak, 1992]. All of these papers share a common formulation in that they calculate potentials which then need to be differentiated either numerically or analytically to find the fields. In this work the Green's function is determined directly which eliminates the need to differentiate an asymptotic series. In general, it is preferable to develop an asymptotic approximation of a differentiated expression rather than differentiating an asymptotic approximation. Additionally, in the previous related approach [Barkeshli *et al.*, 1990; Marin *et al.*, 1989; Marin and Pathak, 1992] the transverse electric (TE) and transverse magnetic (TM) potentials were coupled; in contrast, this work keeps them uncoupled. The coupled solution leads to more complicated integrand topologies in the spectral plane on which the asymptotic approximations are performed when compared to the uncoupled topologies. It is preferable to deal with the simplest possible topology from an accuracy perspective when performing an asymptotic analysis. One final major difference between the analysis presented here and by Barkeshli *et al.* [1990], Marin *et al.* [1989], and Marin and Pathak [1992] is that in the present asymptotic approximation, the influence of any poles on the saddle point contribution is compensated by using the modified Pauli-Clemmow

technique [Clemmow, 1950] which leads to a multiplicative correction factor (transition function), whereas [see Barkeshli *et al.*, 1990; Marin *et al.*, 1989; Marin and Pathak, 1992] the Van der Waerden Method [Van der Waerden, 1951; Felsen and Marcuvitz, 1973] was applied which results in an additive correction term. The multiplicative correction is preferable because calculations are not very sensitive to the computational precision. When the correction factor is additive and a surface or leaky wave pole (LWP) is close to the saddle point, then the solution requires one to take the difference of two very large numbers which numerically might not produce correct results. The advantage to using the Van der Waerden method is that if there are many poles that need to be accounted for, it is a natural extension to simply compensate for each of the poles. When using the modified Pauli-Clemmow technique, a new correction factor must be derived for each multiplicity of poles. It is important to note that in practice, it is unlikely that it will be necessary to compensate for more than three poles, although this paper provides the expressions for an arbitrary number of poles. It will be shown that these expressions are easily calculatable, highly accurate, and efficient.

This paper is organized as follows. Section 2 presents the formulation of dyadic Green's function in terms of Sommerfeld integrals. Section 3 presents a scheme referred to as the envelope extraction technique to numerically evaluate the exact solution in terms of the four Sommerfeld integrals. It is noted once again that the numerical solution is used not only as a reference to validate the accuracy of the asymptotic solution, but also to complement the asymptotic solution in the small region where the latter becomes invalid. The uniform asymptotic evaluation of the Sommerfeld integrals will be presented in section 4 where some common cases will be addressed along with the general formulation. Finally, section 5 will show some numerical results displaying the accuracy of the asymptotic solution, the computation times and some concluding remarks. An $e^{j\omega t}$ time dependence is assumed and suppressed in the following analysis.

2. Dyadic Green's Function Formulation

If we consider an arbitrarily directed, impressed magnetic surface current density, \bar{M}_s , on the ground plane at any point \bar{r}' over some region s , and

we wish to determine the magnetic field \bar{H} on the ground plane at any point \bar{r} , the following expression can be used [Tai, 1973]:

$$\bar{H}(\bar{r}) = \iint_s \bar{\bar{G}}(\bar{r}, \bar{r}') \cdot \bar{M}_s(\bar{r}') ds'. \quad (1)$$

The material coating on the PEC and free space above it have the constitutive parameters ϵ_1, μ_1 and ϵ_0, μ_0 , respectively. Since the normal magnetic field vanishes on a PEC, then by reciprocity, the normal magnetic current does not radiate. We can express the Green's function in a rectangular (x, y, z) basis as follows:

$$\bar{\bar{G}}(\bar{r}, \bar{r}') = \begin{bmatrix} G_{xx}(\bar{r}, \bar{r}') & G_{xy}(\bar{r}, \bar{r}') & 0 \\ G_{yx}(\bar{r}, \bar{r}') & G_{yy}(\bar{r}, \bar{r}') & 0 \\ 0 & 0 & 0 \end{bmatrix}. \quad (2)$$

The first index refers to the polarization of the magnetic field component, and the second index refers to the direction of the magnetic current component in rectangular coordinates. Each of the four nonzero elements of the dyadic Green's function above can be expressed in terms of TE_z and TM_z Sommerfeld integrals:

$$G_{xx}(\bar{r}, \bar{r}') = \frac{1}{2} (I_1^{TM}(\rho) - I_1^{TE}(\rho)) + \frac{\cos(2\theta)}{2} (I_2^{TM}(\rho) + I_2^{TE}(\rho)) \quad (3)$$

$$G_{xy}(\bar{r}, \bar{r}') = G_{yx}(\bar{r}, \bar{r}') = \frac{\sin(2\theta)}{2} (I_2^{TM}(\rho) + I_2^{TE}(\rho)) \quad (4)$$

$$G_{yy}(\bar{r}, \bar{r}') = \frac{1}{2} (I_1^{TM}(\rho) - I_1^{TE}(\rho)) - \frac{\cos(2\theta)}{2} (I_2^{TM}(\rho) + I_2^{TE}(\rho)) \quad (5)$$

where

$$\rho = |\bar{r} - \bar{r}'| \quad (6)$$

$$\theta = \tan^{-1} \left(\frac{(\bar{r} - \bar{r}') \cdot \hat{y}}{(\bar{r} - \bar{r}') \cdot \hat{x}} \right). \quad (7)$$

In other words, ρ is the distance between the source and observation points, and θ is the angle the vector from the source point to the observation point

makes with the positive x axis. These Sommerfeld integral terms are only a function of one variable ρ ; therefore they can be calculated once and stored in a "look-up table" and later recalled to construct the Green's functions. This is particularly useful when analyzing a large two-dimensional array.

The Sommerfeld integrals are given by

$$I_{\{2\}}^{TM}(\rho) = \int_0^\infty \frac{\omega \epsilon_1}{k_z^{(1)}} \frac{A(z)}{TM} J_{\{2\}}^0(\xi \rho) \xi d\xi \quad (8)$$

and

$$I_{\{2\}}^{TE}(\rho) = \int_0^\infty \frac{k_z^{(1)}}{\omega \mu_1} \frac{B(z)}{TE} J_{\{2\}}^0(\xi \rho) \xi d\xi \quad (9)$$

where

$$A(z) = -\epsilon_0 k_z^{(1)} \cos(k_z^{(1)}(h - z)) - j\epsilon_1 k_z^{(0)} \sin(k_z^{(1)}(h - z)) \quad (10)$$

$$B(z) = \mu_1 k_z^{(0)} \cos(k_z^{(1)}(h - z)) + j\mu_0 k_z^{(1)} \sin(k_z^{(1)}(h - z)) \quad (11)$$

$$TM = \epsilon_1 k_z^{(0)} \cos(k_z^{(1)}h) + j\epsilon_0 k_z^{(1)} \sin(k_z^{(1)}h) \quad (12)$$

$$TE = \mu_0 k_z^{(1)} \cos(k_z^{(1)}h) + j\mu_1 k_z^{(0)} \sin(k_z^{(1)}h), \quad (13)$$

where z is the height off the ground plane of the observation point, h is the material thickness, $k_z^{(0)}$ and $k_z^{(1)}$ are the z -directed propagation constants in free space and in the material, respectively. Since $k_z^{(0)}$ corresponds to a semiinfinite region ($z = h \rightarrow \infty$), it contains a branch cut and since $k_z^{(1)}$ corresponds to a finite region ($z = 0 \rightarrow h$), it is single valued. These properties can be verified by the integrands of (8) and (9).

$$k_z^{(0)} = (k_0^2 - \xi^2)^{1/2}; \quad \text{Im}\{k_z^{(0)}\} \leq 0 \quad (14)$$

and

$$k_z^{(1)} = (k_1^2 - \xi^2)^{1/2} \quad (15)$$

where k_0 and k_1 are the propagation constants in free space and in the material, respectively. For the lossless case, there will be at least one surface wave pole (SWP) on the real axis of the Sommerfeld plane (zeros of TM and/or TE). To satisfy the radiation condition, the contour must be skirted above the poles.

As indicated previously, there will be two methods presented to accurately and efficiently compute the Sommerfeld integrals in (8) and (9). One method is a numerical method which works well for very small ρ and hence complements the asymptotic solution since the asymptotic solution is accurate for relatively small to any large value of ρ .

3. Numerical Evaluation of the Exact Solution for the Green's Dyadic (for ρ Small)

In this section a scheme to enhance the convergence of the Sommerfeld integrals which comprise the Green's dyadic, \bar{G} , as indicated in (3)–(5) will be presented. This numerical solution complements the closed-form uniform asymptotic solution (developed in the next section) in a region for ρ small, which is where the asymptotic solution fails. It is noted that the asymptotic solution is useful as long as the separation between the source and field points in greater than only a few tenths of a free space wavelength. This numerical solution is very similar to what was done by *Jackson and Alexopoulos* [1986] with the exception that for the TE type integrals in this paper, two terms were subtracted from the integrand which leads to faster convergence than if one term were subtracted as done previously. A related technique was used by *Pozar* [1984, 1985] to invert the spectral integral of the MM mutual impedance, whereas in this paper the spectral integrals are inverted to produce the spatial domain representation of the various terms of the Green's function.

The behavior of the integrands for large ξ in (8) and (9) are given below:

$$\text{integrand of } I_{\{2\}}^{\text{TM}}(\rho) \sim \begin{cases} - \\ + \end{cases} j\omega\epsilon_1 \left(\frac{2}{\xi\rho\pi} \right)^{1/2} \cdot \cos \left(\xi\rho - \frac{\pi}{4} \right) e^{-\xi z}; \quad \xi \rightarrow \infty \quad (16)$$

$$\text{integrand of } I_{\{2\}}^{\text{TE}}(\rho) \sim \begin{cases} - \\ + \end{cases} \frac{j}{\omega\mu_1} \xi^{3/2} \left(\frac{2}{\rho\pi} \right)^{1/2} \cdot \cos \left(\xi\rho - \frac{\pi}{4} \right) e^{-\xi z}; \quad \xi \rightarrow \infty \quad (17)$$

If these integrands are examined for the case when the observation point is on the ground plane, that is, when $z = 0$, (as is necessary in the mutual coupling

problem for slots), then the integrands no longer exhibit an exponential decay. The TM integrands have an algebraic $\xi^{-1/2}$ decay, and the TE integrands show an algebraic $\xi^{3/2}$ growth. The $\xi\rho$ term in the argument of the cosine functions leads to

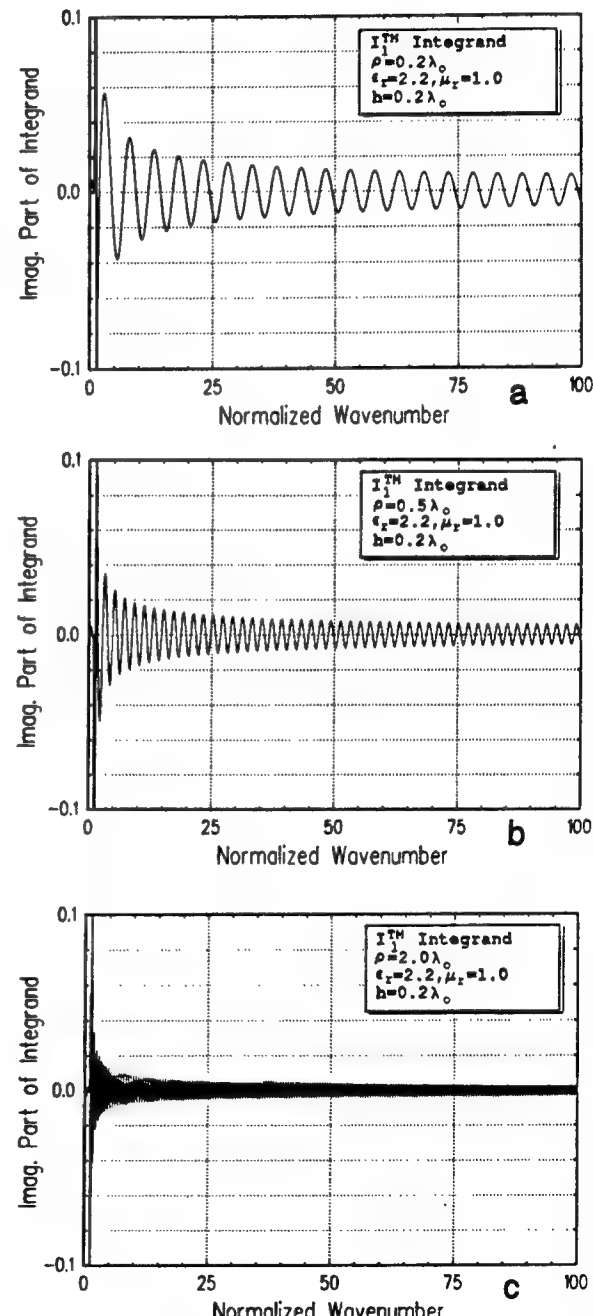


Figure 2. Integrand of I_1^{TM} for (a) $\rho = 0.2\lambda_0$, (b) $\rho = 0.5\lambda_0$ and (c) $\rho = 2.0\lambda_0$. The material slab is characterized by $\epsilon_r = 2.2$, $\mu_r = 1.0$, and a height of $0.2\lambda_0$.

faster integrand oscillation when the separation between the source and observation points ρ becomes large. These TM and TE integrands are shown in Figures 2 and 3, respectively, for various values of ρ . These integrands have such poor convergence (and

divergence in the TE case if $z = 0$) properties because the Sommerfeld representation is a z -propagating representation, and for this case there is no z separation between the source and observation points. If a brute force numerical integration was to be performed, then it would be wise to transform the integrand to a ρ -propagating radial representation [Felsen, 1973]. However, since this solution is also intended to be used for small ρ , a radial representation would not be a wise choice. The envelope extraction technique is applied here [Jackson and Alexopoulos, 1986]. In this technique a large argument form of the integrand is found that can be integrated analytically. This result is then added to one in which the large argument form is subtracted from the original integrand leaving a quickly converging difference to be integrated numerically. The zeros of TM and TE are spectral poles which represent surface wave contributions. In general, there can be a multitude of zeros of both TM and TE. Analogous to the envelope extraction technique, the singularities can be subtracted out of the integrand and replaced analytically since the pole contribution can be integrated in closed form. It is only necessary to subtract the singularities in the region surrounding them, say from ξ_1 to ξ_2 such that $\xi_1 < \xi_{p_n}^{\text{TM}} < \xi_2$ for all pole locations $\xi_{p_n}^{\text{TM}}$, $n = 1, 2, \dots$

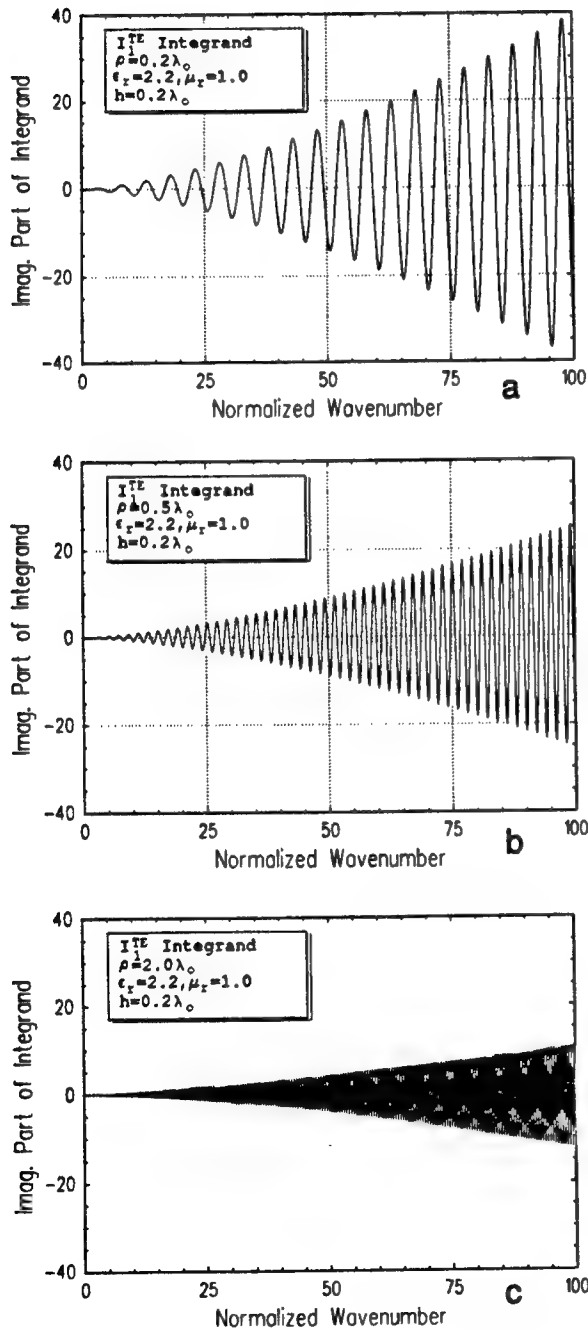


Figure 3. Integrand of I_1^{TE} for (a) $\rho = 0.2\lambda_0$, (b) $\rho = 0.5\lambda_0$ and (c) $\rho = 2.0\lambda_0$. The material slab is characterized by $\epsilon_r = 2.2$, $\mu_r = 1.0$, and a height of $0.2\lambda_0$.

$$\begin{aligned}
 I_{\{2\}}^{\text{TM}}(\rho) = & \int_0^{\xi_1} \left[\frac{\omega \epsilon_1}{k_z^{(1)}} \frac{A(z=0)}{\text{TM}} \xi + j\omega \epsilon_1 \right] J_{\{2\}}^{\{0\}}(\xi \rho) d\xi \\
 & + \int_{\xi_1}^{\xi_2} \left[\left\{ \frac{\omega \epsilon_1}{k_z^{(1)}} \frac{A(z=0)}{\text{TM}} \xi + j\omega \epsilon_1 \right\} \right] J_{\{2\}}^{\{0\}}(\xi \rho) \\
 & - \sum_n \frac{\text{Res} \{F_{\text{TM}}(\xi_{p_n}^{\text{TM}})\}}{\xi - \xi_{p_n}^{\text{TM}}} d\xi \\
 & + \int_{\xi_2}^{\infty} \left[\frac{\omega \epsilon_1}{k_z^{(1)}} \frac{A(z=0)}{\text{TM}} \xi + j\omega \epsilon_1 \right] \\
 & \cdot J_{\{2\}}^{\{0\}}(\xi \rho) d\xi - \frac{j\omega \epsilon_1}{\rho} \\
 & + \sum_n \text{Res} \{F_{\text{TM}}(\xi_{p_n}^{\text{TM}})\} \left[\ln \left(\frac{\xi_2 - \xi_{p_n}^{\text{TM}}}{\xi_{p_n}^{\text{TM}} - \xi_1} \right) - \pi j \right] \quad (18)
 \end{aligned}$$

where n is summed over the finite number of TM SWPs that are solutions to $\text{TM}(\xi_{p_n}^{\text{TM}}) = 0$. The residue is given by

$$\text{Res} \{F_{\text{TM}}(\xi_{p_n}^{\text{TM}})\} = \left[\frac{\omega \varepsilon_1}{k_z^{(1)}} \frac{\partial}{\partial \xi} \frac{A(z=0)}{\text{TM}} \xi J_{\{2\}}^0(\xi \rho) \right]_{\xi=\xi_{p_n}^{\text{TM}}} \quad (19)$$

Figure 4 shows an example of the modified integrand for the cases shown in Figure 2, with the envelope and singularity extraction techniques applied. Note the scale change of both axes. These new integrands are less oscillatory and decay fast; hence they are much easier to numerically integrate. There is only a single SWP for this configuration. The spike in the plots shows that there was not a perfect cancellation at the singularity. Numerically, this is not a problem because a numerical integration technique such as Gauss quadrature that does not integrate at the endpoint of an interval can be used to guarantee that the pole location will not be chosen for evaluation.

The TE Sommerfeld integrals will be handled in much the same manner as the TM Sommerfeld integrals. Mathematically, in the present form the TE integrands are divergent for $z = 0$ and are therefore meaningless. This does not mean that the proper information is not contained in these integrals; rather, it is indicative of the failure of the Sommerfeld representation for $z = 0$. If we consider the fields at a small distance above the ground plane, perform the envelope subtraction, and take the limit as this distance goes to zero, useful expressions are obtained. A minor difference between the TE and TM integrals is that it is possible, and beneficial, to subtract 2 orders of the large argument form of the integrand for the TE case:

$$\begin{aligned} I_{\{2\}}^{\text{TE}}(\rho) &= \int_0^{\infty} \left[\frac{k_z^{(1)}}{\omega \mu_1} \frac{B(z=0)}{\text{TE}} \xi \right. \\ &\quad \left. + \frac{j}{\omega \mu_1} \xi^2 - \frac{jk_1^2}{2\omega \mu_1} \right] J_{\{2\}}^0(\xi \rho) d\xi \\ &\quad + \int_{\xi_1}^{\xi_2} \left\{ \left[\frac{k_z^{(1)}}{\omega \mu_1} \frac{B(z=0)}{\text{TE}} \xi + \frac{j}{\omega \mu_1} \xi^2 - \frac{jk_1^2}{2\omega \mu_1} \right] J_{\{2\}}^0(\xi \rho) \right. \\ &\quad \left. - \sum_n \frac{\text{Res} \{F_{\text{TE}}(\xi_{p_n}^{\text{TE}})\}}{\xi - \xi_{p_n}^{\text{TE}}} \right\} d\xi \end{aligned}$$

$$\begin{aligned} &+ \int_{\xi_2}^{\infty} \left[\frac{k_z^{(1)}}{\omega \mu_1} \frac{B(z=0)}{\text{TE}} \xi \right. \\ &\quad \left. + \frac{j}{\omega \mu_1} \xi^2 - \frac{jk_1^2}{2\omega \mu_1} \right] J_{\{2\}}^0(\xi \rho) d\xi \\ &- \frac{j}{\omega \mu_1} \frac{\begin{Bmatrix} -1 \\ 3 \end{Bmatrix}}{\rho^3} + \frac{jk_1^2}{2\omega \mu_1} \frac{1}{\rho} \\ &+ \sum_n \text{Res} \{F_{\text{TE}}(\xi_{p_n}^{\text{TE}})\} \left[\ln \left(\frac{\xi_2 - \xi_{p_n}^{\text{TE}}}{\xi_{p_n}^{\text{TE}} - \xi_1} \right) - \pi j \right] \quad (20) \end{aligned}$$

where n is summed over the finite number (if any) of TE SWPs, $\xi_{p_n}^{\text{TE}}$, which are solutions to $\text{TE}(\xi_{p_n}^{\text{TE}}) = 0$, and

$$\text{Res} \{F_{\text{TE}}(\xi_{p_n}^{\text{TE}})\} = \left[\frac{k_z^{(1)}}{\omega \mu_1} \frac{\partial}{\partial \xi} \frac{B(z=0)}{\text{TE}} \xi J_{\{2\}}^0(\xi \rho) \right]_{\xi=\xi_{p_n}^{\text{TE}}} \quad (21)$$

It is a common occurrence for substrates that are electrically thin not to have any TE surface wave poles. For this case, (20) takes the following form:

$$\begin{aligned} I_{\{2\}}^{\text{TE}}(\rho) &= \int_0^{\infty} \left[\frac{k_z^{(1)}}{\omega \mu_1} \frac{B(z=0)}{\text{TE}} \xi + \frac{j}{\omega \mu_1} \xi^2 \right. \\ &\quad \left. - \frac{jk_1^2}{2\omega \mu_1} \right] J_{\{2\}}^0(\xi \rho) d\xi - \frac{j}{\omega \mu_1} \frac{\begin{Bmatrix} -1 \\ 3 \end{Bmatrix}}{\rho^3} + \frac{jk_1^2}{2\omega \mu_1} \frac{1}{\rho} \quad (22) \end{aligned}$$

The integrand for the latter case is shown in Figure 5, indicating that it is slowly oscillating and quickly convergent; thus it is in a form amenable to numerical integration.

4. Uniform Asymptotic Closed Form Evaluation of the Green's Dyadic (for ρ Relatively Small to Large)

In this section, closed-form uniform asymptotic solutions for the four Sommerfeld integrals in (8)–(9) are presented. This asymptotic solution complements the numerical solution of the previous section since the asymptotic solution is accurate and efficient for ρ greater than a few tenths of a free space wavelength below which the numerical solu-

tion is useful. These results can be substituted in (3)–(5) to directly arrive at the closed-form asymptotic approximation for the Green's dyadic \tilde{G} of (2). The incentive for using this asymptotic solution is

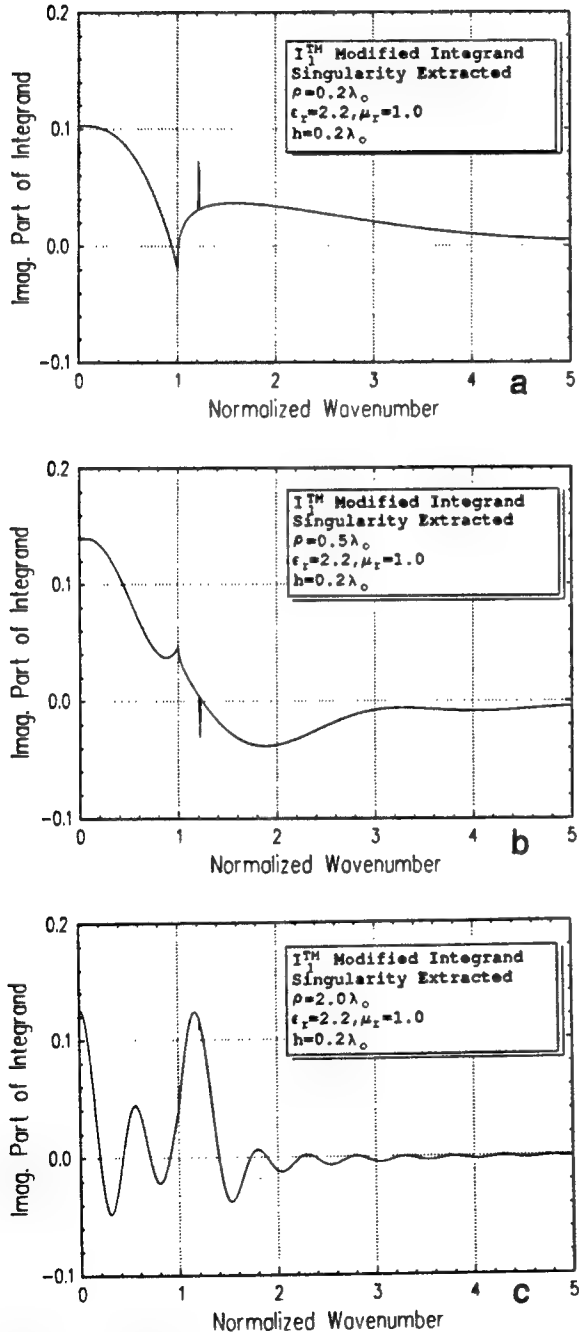


Figure 4. Integrand of I_1^{TM} with the envelope and singularity extracted as indicated in (18) for (a) $\rho = 0.2\lambda_0$, (b) $\rho = 0.5\lambda_0$ and (c) $\rho = 2.0\lambda_0$. The parameters $\epsilon_r = 2.2$, $\mu_r = 1.0$, and $h = 0.2\lambda_0$.

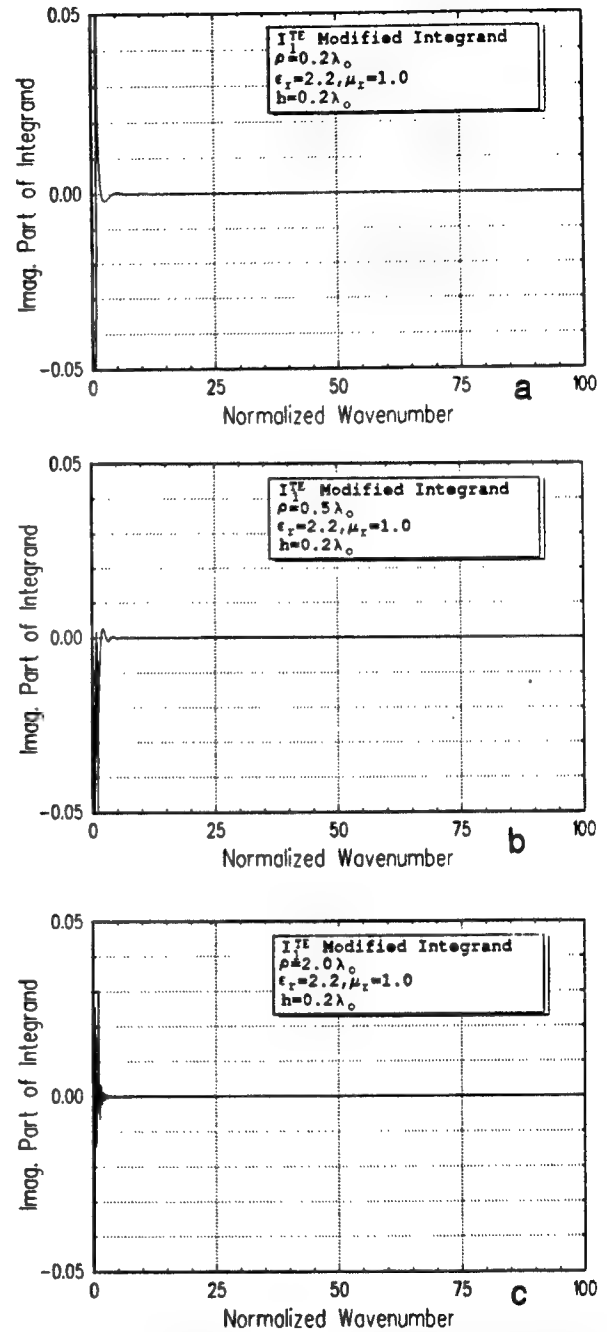


Figure 5. Integrand of I_1^{TE} with the envelope extraction as indicated in (22) for (a) $\rho = 0.2\lambda_0$, (b) $\rho = 0.5\lambda_0$ and (c) $\rho = 2.0\lambda_0$. The parameters $\epsilon_r = 2.2$, $\mu_r = 1.0$, and $h = 0.2\lambda_0$.

that it is extremely computationally efficient and typically remains accurate even for source and observation point separations of only a few tenths of a free space wavelength because of its uniform

nature. All of the relevant transition effects associated with the confluence of surface and leaky domains with the space waves directly radiated by the source are incorporated into the solution.

Equations (8) and (9) are expressed in terms of a semiinfinite contour which is not convenient for function theoretic manipulations of integrals. A more appropriate form is given below:

$$I_{\{2\}}^{TM}(\rho) = \frac{1}{2} \int_{\infty e^{-j\pi}}^{\infty} F_{TM} H_{\{2\}}^{(2)}(\xi\rho) \xi d\xi \quad (23)$$

$$I_{\{2\}}^{TE}(\rho) = \frac{1}{2} \int_{\infty e^{-j\pi}}^{\infty} F_{TE} H_{\{2\}}^{(2)}(\xi\rho) \xi d\xi \quad (24)$$

where

$$F_{TM} = \frac{\omega \epsilon_1}{k_z^{(1)}} \frac{A(z=0)}{TM} \quad (25)$$

$$F_{TE} = \frac{k_z^{(1)}}{\omega \mu_1} \frac{B(z=0)}{TE} \quad (26)$$

Note that $H_0^{(2)}(\xi\rho)$ has a branch cut on the negative real ξ axis, and $H_2^{(2)}(\xi\rho)$ has a double pole at the origin.

The modified Pauli-Clemmow technique [Clemmow, 1950], which is used here, corrects for the influence of the SWPs and LWPs on the saddle point by multiplying the conventional space wave solution by the appropriate transition function. The transition function that should be used depends on the number of poles that are in the saddle point region. For most problems of practical interest, it appears sufficient to consider the influence of one to three poles. The number of poles that need to be considered is discussed by Marin *et al.* [1990].

Unlike the numerical method for evaluating \tilde{G} discussed in section 2, where it is only necessary to be concerned with the proper (or top) Riemann sheet of the Sommerfeld plane, the asymptotic method implicitly incorporates the features of the improper (or bottom) Riemann sheet, and thus one must be cognizant of its topology. It is visually instructive (although not necessary) to map both the improper and proper Riemann sheets of the $k_z^{(0)} = (k_0^2 - \xi^2)^{1/2}$ function onto the angular spectral, γ , plane by the following mapping:

$$\xi = k_0 \sin \gamma \quad (27)$$

The integrals in (23) and (24) under the above mapping take the following form:

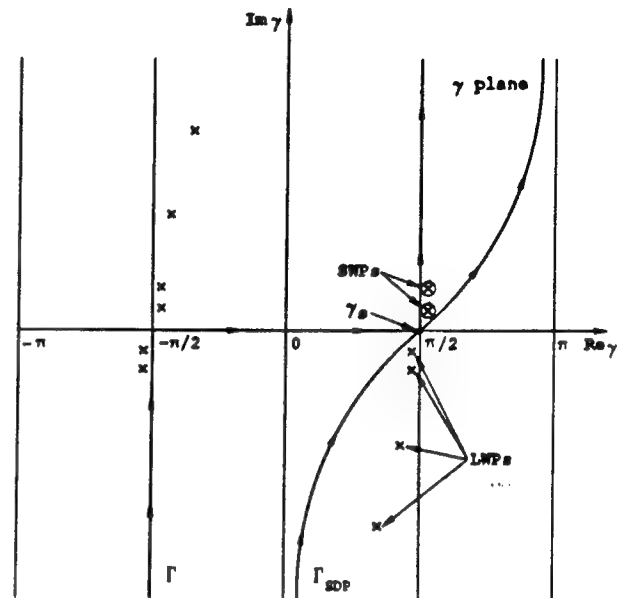


Figure 6. Angular spectral plane with the real axis of the Sommerfeld plane mapped into Γ , and the steepest descent path is indicated by Γ_{SDP} . The saddle point is γ_s .

$$I_{\{2\}}^{TM}(\rho) = \frac{k_0^2}{2} \int_{\Gamma} F_{TM} H_{\{2\}}^{(2)}(k_0 \rho \sin \gamma) \sin \gamma \cos \gamma d\gamma \quad (28)$$

$$I_{\{2\}}^{TE}(\rho) = \frac{k_0^2}{2} \int_{\Gamma} F_{TE} H_{\{2\}}^{(2)}(k_0 \rho \sin \gamma) \sin \gamma \cos \gamma d\gamma \quad (29)$$

where Γ is the γ -plane image of ξ -plane real axis on the proper sheet under the mapping in (27) (see Figure 6). The integrals in (28) and (29) are exact representations of the solution. To facilitate the asymptotic approximation, the Hankel functions are replaced by their two-term large argument form. This is justified (with hindsight) because the saddle point is sufficiently far from the origin:

$$H_{\{2\}}^{(2)}(x) \sim \left\{ \begin{array}{l} + \\ - \end{array} \right\} \left(\frac{2}{\pi x} \right)^{1/2} \cdot \exp \left[-j \left(x - \frac{\pi}{4} \right) \right] \left(1 + \frac{j \left\{ \begin{array}{l} 1 \\ -15 \end{array} \right\}}{8x} \right) \quad (30)$$

In light of the asymptotic approximations for the Hankel functions above, it is clear that the integrands of (28) and (29) possess a saddle point, γ_s , at

$\gamma_s = \pi/2$. The original contour, Γ , can be deformed to the steepest descent path (SDP) shown in Figure 6. All of the surface wave poles are captured in the contour deformation. The relevant poles all lie in the region of the saddle point along the line $\text{Re}(\gamma) = \pi/2$ (for the lossless case). The poles in this region that lie in the upper half of the γ plane ($\text{Im}\{\gamma\} > 0$), are surface wave poles and those which lie in the lower half of the γ -plane ($\text{Im}\{\gamma\} < 0$), are leaky wave poles. The surface wave poles were mapped from the proper sheet of the Sommerfeld ξ plane, and the leaky wave poles were mapped from the improper sheet of the Sommerfeld ξ plane. The Sommerfeld integrals can be expressed as follows:

$$I_{\{2\}}^{\text{TM}}(\rho) \sim -2\pi j \sum_n \text{Res}_{\{2\}}^{\text{TM}} + \text{SDP}I_{\{2\}}^{\text{TM}} \quad (31)$$

$$I_{\{2\}}^{\text{TE}}(\rho) \sim -2\pi j \sum_n \text{Res}_{\{2\}}^{\text{TE}} + \text{SDP}I_{\{2\}}^{\text{TE}} \quad (32)$$

where

$$\begin{aligned} \text{SDP}I_{\{2\}}^{\text{TM}} &= \left\{ \begin{array}{l} + \\ - \end{array} \right\} \frac{k_0^2}{2} \left(\frac{2}{\pi k_0 \rho} \right)^{1/2} e^{j(\pi/4)} \\ &\cdot \int_{\Gamma_{\text{SDP}}} F_{\text{TM}} \sin^{1/2} \gamma \cos \gamma \left(1 + \frac{j \begin{Bmatrix} 1 \\ -15 \end{Bmatrix}}{8k_0 \rho \sin \gamma} \right) \\ &\cdot \exp(-jk_0 \rho \sin \gamma) d\gamma \quad (33) \end{aligned}$$

$$\begin{aligned} \text{SDP}I_{\{2\}}^{\text{TE}} &= \left\{ \begin{array}{l} + \\ - \end{array} \right\} \frac{k_0^2}{2} \left(\frac{2}{\pi k_0 \rho} \right)^{1/2} e^{j(\pi/4)} \\ &\cdot \int_{\Gamma_{\text{SDP}}} F_{\text{TE}} \sin^{1/2} \gamma \cos \gamma \left(1 + \frac{j \begin{Bmatrix} 1 \\ -15 \end{Bmatrix}}{8k_0 \rho \sin \gamma} \right) \\ &\cdot \exp(-jk_0 \rho \sin \gamma) d\gamma. \quad (34) \end{aligned}$$

The sum over n includes all surface wave poles. The residues are given by

$$\begin{aligned} \text{Res}_{\{2\}}^{\text{TM}} &= \left[\frac{k_0^2 \omega \epsilon_1}{2} \frac{A(z=0)}{k_z^{(1)} \frac{\partial}{\partial \gamma} \text{TM}} \right. \\ &\left. \cdot H_{\{2\}}^{(2)}(k_0 \rho \sin \gamma) \sin \gamma \cos \gamma \right]_{\gamma=\gamma_{p_n}^{\text{TM}}} \quad (35) \end{aligned}$$

$$\begin{aligned} \text{Res}_{\{2\}}^{\text{TE}} &= \left[\frac{k_0^2}{2} \frac{k_z^{(1)}}{\omega \mu_1} \frac{B(z=0)}{\frac{\partial}{\partial \gamma} \text{TE}} \right. \\ &\left. \cdot H_{\{2\}}^{(2)}(k_0 \rho \sin \gamma) \sin \gamma \cos \gamma \right]_{\gamma=\gamma_{p_n}^{\text{TE}}} \quad (36) \end{aligned}$$

Note that the residues are extracted from the integral before the Hankel function approximation of (30) is implemented; thus the residue contributions are exact.

The standard form in which to implement the asymptotic approximations of the integrals of (33) and (34) can be realized by mapping this γ -plane representation to the s plane by the following transformation:

$$\sin \gamma = 1 - js^2 \quad \cos \gamma = -s(s^2 + 2j)^{1/2}$$

$$d\gamma = \frac{2j}{(s^2 + 2j)^{1/2}} ds \quad (37)$$

The SDP contribution of (31) and (32) can be expressed in the s plane by

$$\begin{aligned} \text{SDP}I_{\{2\}}^{\text{TM}} &= \left\{ \begin{array}{l} + \\ - \end{array} \right\} \frac{k_0^2}{2} \left(\frac{2}{\pi k_0 \rho} \right)^{1/2} e^{j(\pi/4)} e^{-jk_0 \rho} \\ &\cdot \int_{-\infty}^{\infty} T_{\{2\}}^{\text{TM}}(s) \exp(-k_0 \rho s^2) ds \quad (38) \end{aligned}$$

$$\begin{aligned} \text{SDP}I_{\{2\}}^{\text{TE}} &= \left\{ \begin{array}{l} + \\ - \end{array} \right\} \frac{k_0^2}{2} \left(\frac{2}{\pi k_0 \rho} \right)^{1/2} e^{j(\pi/4)} e^{-jk_0 \rho} \\ &\cdot \int_{-\infty}^{\infty} T_{\{2\}}^{\text{TE}}(s) \exp(-k_0 \rho s^2) ds \quad (39) \end{aligned}$$

where

$$\begin{aligned} T_{\{2\}}^{\text{TM}}(s) &= -F_{\text{TM}} (1 - js^2)^{1/2} s(s^2 + 2j)^{1/2} \\ &\cdot \left(1 + \frac{j \begin{Bmatrix} 1 \\ -15 \end{Bmatrix}}{8k_0 \rho (1 - js^2)} \right) \quad (40) \end{aligned}$$

$$\begin{aligned} T_{\{2\}}^{\text{TE}}(s) &= -F_{\text{TE}} (1 - js^2)^{1/2} s(s^2 + 2j)^{1/2} \\ &\cdot \left(1 + \frac{j \begin{Bmatrix} 1 \\ -15 \end{Bmatrix}}{8k_0 \rho (1 - js^2)} \right). \quad (41) \end{aligned}$$

Since $T_{\{2\}}^{\text{TM}}(0) = T_{\{2\}}^{\text{TE}}(0) = 0$, it is necessary to perform a second-order asymptotic evaluation of the integrals in (38) and (39). For the case of the source and observation points both on the ground plane, which is being addressed in this paper, the SDP is fixed in the γ plane with the saddle point at $\gamma = \pi/2$. When the system parameters vary, the poles migrate and are restricted to the line $\text{Re}\{\gamma\} = \pi/2$ in the vicinity of the saddle point. The only point onto which the poles can intersect the SDP is the saddle point; thus it is appropriate to use the modified Pauli-Clemmow technique [Clemmow, 1950]. In practice, it is typically necessary to consider the influence of one, two, or three poles simultaneously on the SDP contribution. These cases are presented along with the more general N pole case for completeness.

4.1. Uniform Asymptotic Evaluation of an Integral With a Single Pole Influence on the Saddle Point

When implementing the modified Pauli-Clemmow technique, the function $T(s)$ (which represents the integrand in all four cases): $T_{\{2\}}^{\text{TM}}(s)$ and $T_{\{2\}}^{\text{TE}}(s)$ are expressed in terms of a function $T_a(s)$, whose region of analyticity is a disk, centered at $s = 0$, with a radius equal to the distance to the closest pole other than the pole being accounted for at $s = s_p$; s_p can be determined from (37):

$$T(s) = \frac{T_a(s)}{s - s_p} \quad (42)$$

Implementing the standard uniform asymptotic reduction of the integrals, one obtains

$$\begin{aligned} \text{SDP} I_{\{2\}}^{\text{TM}} &\sim \left\{ \begin{array}{l} + \\ - \end{array} \right\} k_0^2 \frac{\partial}{\partial \gamma} F_{\text{TM}, \gamma=\gamma_s} \mathcal{F}_s(jk_0 \rho (s_p^{\text{TM}})^2) \\ &\cdot \left(1 + \frac{j \begin{Bmatrix} 1 \\ -15 \end{Bmatrix}}{8k_0 \rho} \right) \frac{e^{-jk_0 \rho}}{(k_0 \rho)^2} \end{aligned} \quad (43)$$

$$\begin{aligned} \text{SDP} I_{\{2\}}^{\text{TE}} &\sim \left\{ \begin{array}{l} + \\ - \end{array} \right\} k_0^2 \frac{\partial}{\partial \gamma} F_{\text{TE}, \gamma=\gamma_s} \mathcal{F}_s(jk_0 \rho (s_p^{\text{TE}})^2) \\ &\cdot \left(1 + \frac{j \begin{Bmatrix} 1 \\ -15 \end{Bmatrix}}{8k_0 \rho} \right) \frac{e^{-jk_0 \rho}}{(k_0 \rho)^2} \end{aligned} \quad (44)$$

where

$$\frac{\partial}{\partial \gamma} F_{\text{TM}, \gamma=\gamma_s} = \frac{\omega \epsilon_1^2 k_0}{\epsilon_0 (k_1^2 - k_0^2) \sin^2 [(k_1^2 - k_0^2)^{1/2} h]} \quad (45)$$

$$\frac{\partial}{\partial \gamma} F_{\text{TE}, \gamma=\gamma_s} = \frac{k_0}{\omega \mu_0 \cos^2 [(k_1^2 - k_0^2)^{1/2} h]} \quad (46)$$

and $\mathcal{F}_s(x)$ is the slope transition function [Hwang and Kouyoumjian, 1974] given by

$$\mathcal{F}_s(x) = 2jx[1 - \mathcal{F}(x)]. \quad (47)$$

$\mathcal{F}(x)$ is the wedge diffraction transition function [Kouyoumjian and Pathak, 1974], which is easily calculated [Pathak and Kouyoumjian, 1970].

The argument of the transition function can be expressed as follows:

$$jk_0 \rho (s_p^{\text{TM}})^2 = (k_0 - \xi_p^{\text{TM}}) \rho \quad (48)$$

$$jk_0 \rho (s_p^{\text{TE}})^2 = (k_0 - \xi_p^{\text{TE}}) \rho \quad (49)$$

where ξ_p^{TM} and ξ_p^{TE} are the zeros of TM and TE, respectively. If the pole under consideration is a SWP, then the zero lies on the top Riemann sheet of the Sommerfeld plane and if the pole corresponds to a LWP, then the zero would lie on the bottom Riemann sheet. Note that since $\text{Re}\{\xi_p^{\text{TE}}\} \geq k_0$, then the argument of the transition function is not positive, and the following relationship is useful for real arguments:

$$\mathcal{F}(-|x|) = \mathcal{F}^*(|x|) \quad (50)$$

where the asterisk indicates complex conjugate.

4.2. Uniform Asymptotic Evaluation of an Integral With Two Poles Near a Saddle Point

The development of the case where two poles, s_{p_1} and s_{p_2} , are close enough to the saddle point to influence its evaluation is similar to the single pole case developed in the previous section. Now the integrand is represented by the following equation:

$$T(s) = \frac{T_a(s)}{(s - s_{p_1})(s - s_{p_2})} \quad (51)$$

Performing a partial fraction expansion on (51) and implementing an asymptotic procedure similar to the single pole case, the uniform asymptotic solution can be found to be

$$SDP I_{\{2\}}^{\text{TM}} - \begin{cases} + \\ - \end{cases} k_0^2 \left[\frac{e^{-j(\pi/4)} F_{\text{TM}}(\gamma_s) (\mathcal{F}_s(jk_0 \rho(s_{p_1}^{\text{TM}})^2)) - \mathcal{F}_s(jk_0 \rho(s_{p_2}^{\text{TM}})^2)}{2^{1/2} s_{p_1}^{\text{TM}} - s_{p_2}^{\text{TM}}} \right. \right. \\ \left. \left. + \frac{\frac{\partial}{\partial \gamma} F_{\text{TM}}|_{\gamma=\gamma_s} (s_{p_1}^{\text{TM}} \mathcal{F}_s(jk_0 \rho(s_{p_2}^{\text{TM}})^2) - s_{p_2}^{\text{TM}} \mathcal{F}_s(jk_0 \rho(s_{p_1}^{\text{TM}})^2))}{s_{p_1}^{\text{TM}} - s_{p_2}^{\text{TM}}} \right] \left(1 + \frac{j \begin{Bmatrix} 1 \\ -15 \end{Bmatrix}}{8k_0 \rho} \right) \frac{e^{-jk_0 \rho}}{(k_0 \rho)^2} \right] \quad (52)$$

$$SDP I_{\{2\}}^{\text{TE}} - \begin{cases} + \\ - \end{cases} k_0^2 \left[\frac{e^{-j(\pi/4)} F_{\text{TE}}(\gamma_s) (\mathcal{F}_s(jk_0 \rho(s_{p_1}^{\text{TE}})^2)) - \mathcal{F}_s(jk_0 \rho(s_{p_2}^{\text{TE}})^2)}{2^{1/2} s_{p_1}^{\text{TE}} - s_{p_2}^{\text{TE}}} \right. \right. \\ \left. \left. + \frac{\frac{\partial}{\partial \gamma} F_{\text{TE}}|_{\gamma=\gamma_s} (s_{p_1}^{\text{TE}} \mathcal{F}_s(jk_0 \rho(s_{p_2}^{\text{TE}})^2) - s_{p_2}^{\text{TE}} \mathcal{F}_s(jk_0 \rho(s_{p_1}^{\text{TE}})^2))}{s_{p_1}^{\text{TE}} - s_{p_2}^{\text{TE}}} \right] \left(1 + \frac{j \begin{Bmatrix} 1 \\ -15 \end{Bmatrix}}{8k_0 \rho} \right) \frac{e^{-jk_0 \rho}}{(k_0 \rho)^2} \right] \quad (53)$$

where

$$F_{\text{TM}}(\gamma_s) = j \frac{\omega \epsilon_1}{(k_1^2 - k_0^2)^{1/2}} \cot [(k_1^2 - k_0^2)^{1/2} h] \quad (54)$$

$$F_{\text{TE}}(\gamma_s) = j \frac{(k_1^2 - k_0^2)^{1/2}}{\omega \mu_1} \tan [(k_1^2 - k_0^2)^{1/2} h] \quad (55)$$

When evaluating the SDP contribution that is influenced by two or more poles, it is necessary to use the proper branch of $s_p = (s_p^2)^{1/2}$

$$s_p = \pm e^{j(\pi/4)} |s_p| \quad (56)$$

where the plus sign is taken for SWPs and the minus sign is taken for LWPs. The parameter s_p refers to

either a SWP or LWP that is in the vicinity of the saddle point.

4.3. Uniform Asymptotic Evaluation of an Integral With Three Poles Near a Saddle Point

The three-pole case follows the same development as the two-pole case where the integrand is now represented by

$$T(s) = \frac{T_a(s)}{(s - s_{p_1})(s - s_{p_2})(s - s_{p_3})}. \quad (57)$$

Performing the appropriate manipulations and asymptotic analyses, one obtains equations (58) and (59).

$$SDP I_{\{2\}}^{\text{TM}} - \begin{cases} + \\ - \end{cases} k_0^2 \sum_{n=1}^3 \frac{-\frac{e^{-j(\pi/4)}}{2^{1/2}} F_{\text{TM}}(\gamma_s) \sum_{i=1}^3 s_{p_i}^{\text{TM}} + \frac{\partial}{\partial \gamma} F_{\text{TM}}|_{\gamma=\gamma_s} \prod_{l=1}^3 s_{p_l}^{\text{TM}}}{\prod_{m=1}^3 (s_{p_n}^{\text{TM}} - s_{p_m}^{\text{TM}})} \mathcal{F}_s(jk_0 \rho(s_{p_n}^{\text{TM}})^2) \left(1 + \frac{j \begin{Bmatrix} 1 \\ -15 \end{Bmatrix}}{8k_0 \rho} \right) \frac{e^{-jk_0 \rho}}{(k_0 \rho)^2} \quad (58)$$

$$SDP I_{\{2\}}^{\text{TE}} - \begin{cases} + \\ - \end{cases} k_0^2 \sum_{n=1}^3 \frac{-\frac{e^{-j(\pi/4)}}{2^{1/2}} F_{\text{TE}}(\gamma_s) \sum_{i=1}^3 s_{p_i}^{\text{TE}} + \frac{\partial}{\partial \gamma} F_{\text{TE}}|_{\gamma=\gamma_s} \prod_{l=1}^3 s_{p_l}^{\text{TE}}}{\prod_{m=1}^3 (s_{p_n}^{\text{TE}} - s_{p_m}^{\text{TE}})} \mathcal{F}_s(jk_0 \rho(s_{p_n}^{\text{TE}})^2) \left(1 + \frac{j \begin{Bmatrix} 1 \\ -15 \end{Bmatrix}}{8k_0 \rho} \right) \frac{e^{-jk_0 \rho}}{(k_0 \rho)^2} \quad (59)$$

4.4. Uniform Asymptotic Evaluation of an Integral With N Poles Near a Saddle Point

If one wishes to extend the asymptotic analysis to an electrically thick substrate, then the same formulation applies. In general, as the material coating becomes electrically thicker, it becomes necessary to account for more poles (SWPs and LWPs) which move into the proximity of the saddle point. The same technique is used here that was used in sections 4.1-4.3 to evaluate an integral via a uniform asymptotic procedure which accounts for the confluence of N poles near a saddle point. The integrand is written as follows:

$$T(s) = \frac{T_a(s)}{\prod_{m=1}^N (s - s_{p_m})} \quad (60)$$

where N is the number of poles incorporated into the analysis of that particular integral. This leads to the closed-form uniform asymptotic approximation of the SDP integrals of (38) and (39):

5. Results and Conclusions

In this section we will examine the accuracy of the closed-form uniform asymptotic solution developed in section 4 by comparing it with the "exact" numerical solution which is calculated by using the envelope extraction technique of section 3. The comparisons will be made directly on the Green's function, since this is the relevant physical quantity rather than on its components, the Sommerfeld integrals. From the asymptotic evaluation of the Sommerfeld integrals, the order of decay of each of the integrals is known and by applying this information to the Green's functions of (3)-(5), the surface wave "radiation" patterns are easily obtained. Finally, the computation times of the numerical and asymptotic solutions will be compared. The closed-form asymptotic solution will be shown to be extremely efficient which is very useful for the numerical computation of mutual coupling of electrically large slot arrays that otherwise might have been intractable.

By examining the asymptotic solutions given by (3)-(5), (31)-(36), and (43)-(44), one can determine that the dominant field contribution, away from the source, is dictated by the SWP residue terms (that is, surface waves) which decay as $\rho^{-1/2}$. The SDP

$$\text{SDP} I_{\{1\}}^{\text{TM}} - \left\{ \begin{matrix} + \\ - \end{matrix} \right\} k_0^2 \sum_{n=1}^N \frac{\frac{e^{-j(\pi/4)}}{2^{1/2}} F_{\text{TM}}(\gamma_s) \sum_{\substack{l=1 \\ l \neq n}}^N \prod_{\substack{i=1 \\ i \neq l \\ i \neq n}}^N (-s_{p_i}^{\text{TM}}) + \frac{\partial}{\partial \gamma} F_{\text{TM}}|_{\gamma=\gamma_s} \prod_{\substack{i=1 \\ i \neq n}}^N (-s_{p_i}^{\text{TM}})}{\prod_{\substack{i=1 \\ i \neq n}}^N (s_{p_n}^{\text{TM}} - s_{p_i}^{\text{TM}})} \mathcal{F}_s(jk_0 \rho (s_{p_n}^{\text{TM}})^2) \left(1 + \frac{j \left\{ \begin{matrix} 1 \\ -15 \end{matrix} \right\}}{8k_0 \rho} \right) \frac{e^{-jk_0 \rho}}{(k_0 \rho)^2} \quad (61)$$

$$\text{SDP} I_{\{1\}}^{\text{TE}} - \left\{ \begin{matrix} + \\ - \end{matrix} \right\} k_0^2 \sum_{n=1}^N \frac{\frac{e^{-j(\pi/4)}}{2^{1/2}} F_{\text{TE}}(\gamma_s) \sum_{\substack{l=1 \\ l \neq n}}^N \prod_{\substack{i=1 \\ i \neq l \\ i \neq n}}^N (-s_{p_i}^{\text{TE}}) + \frac{\partial}{\partial \gamma} F_{\text{TE}}|_{\gamma=\gamma_s} \prod_{\substack{i=1 \\ i \neq n}}^N (-s_{p_i}^{\text{TE}})}{\prod_{\substack{i=1 \\ i \neq n}}^N (s_{p_n}^{\text{TE}} - s_{p_i}^{\text{TE}})} \mathcal{F}_s(jk_0 \rho (s_{p_n}^{\text{TE}})^2) \left(1 + \frac{j \left\{ \begin{matrix} 1 \\ -15 \end{matrix} \right\}}{8k_0 \rho} \right) \frac{e^{-jk_0 \rho}}{(k_0 \rho)^2} \quad (62)$$

contribution decays as ρ^{-2} since the slope transition function approaches unity as ρ becomes large. Because of the dominance of the surface wave terms (for purposes of examining the far-field "radiation" pattern of a magnetic current and observation point on the ground plane), it is only necessary to consider the residue contributions. This implies that the Sommerfeld integrals of type 1 are approximately the negative of the Sommerfeld integrals of type 2. This relationship along with the prescription of constructing the Green's dyadic in (3)–(5) yields the copolarization and cross-polarization surface wave radiation patterns in Figure 7. The patterns in both Figures 7a and 7b are due to an x -oriented magnetic current source. The pattern in Figure 7a is

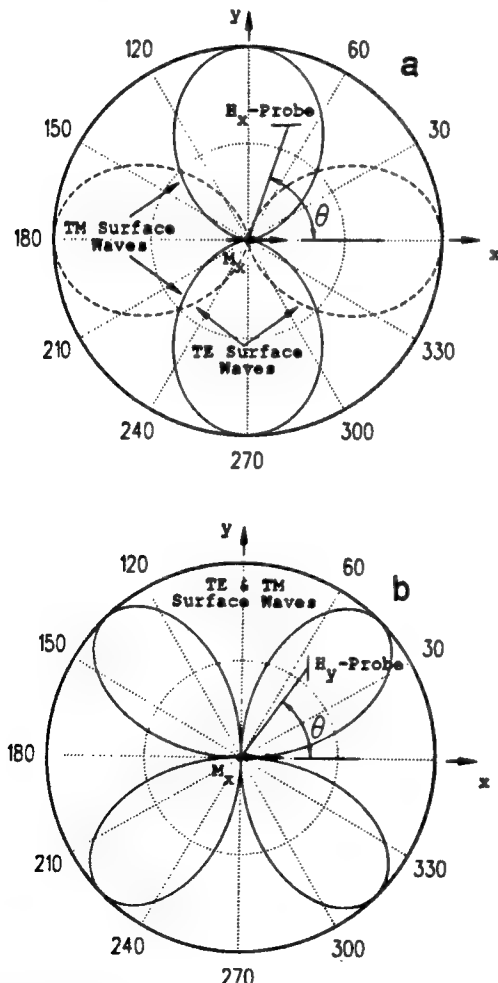


Figure 7. Surface wave "radiation" patterns for an x -directed magnetic current source receiving (a) the x -polarized field (co-pol) and (b) the y -polarized field (cross-pol).

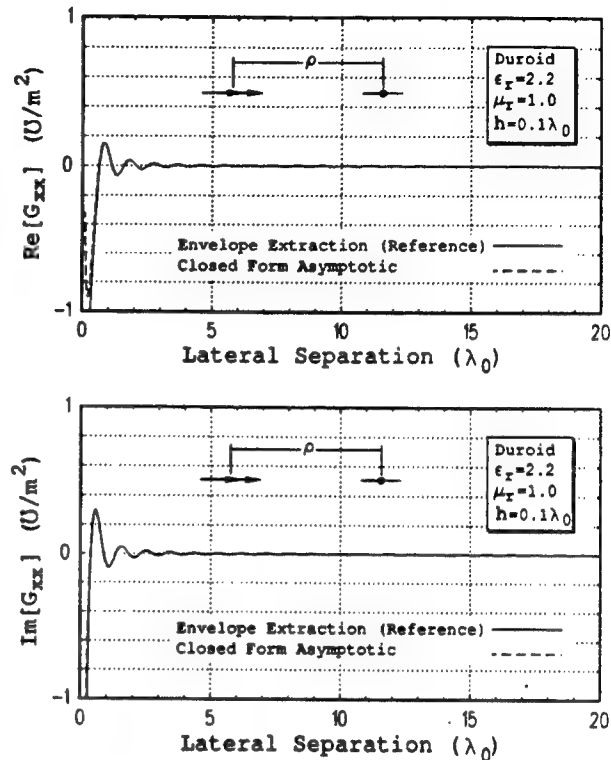


Figure 8. Comparison of closed-form uniform asymptotic G_{xx} component of the dyadic Green's function with "exact" solution computed using the envelope extraction technique. Cut taken in direction of surface wave null. The parameters $\epsilon_r = 2.2$, $\mu_r = 1.0$, and $h = 0.1\lambda_0$.

proportional to the x component of the magnetic field, and the pattern in Figure 7b is proportional to the y component of the magnetic field. Unlike this sketch, the various surface waves typically have different relative magnitudes.

The first example of a closed-form uniform asymptotic calculation is of a material with a relative permittivity of 2.2, a relative permeability of 1.0, and a dielectric thickness of 0.1 free space wavelength. This structure has a single TM SWP and a single TE LWP which need to be incorporated into the uniform asymptotic analysis [Marin *et al.*, 1990]. Since there is only one pole in the proximity of the saddle point in each of the two TM integrands and the two TE integrands, the single pole formulation of section 4.1 was used. Only one surface wave pole exists in each of the TM-type integrals; hence the surface wave will propagate along the dielectric slab broadside to the magnetic current. Figure 8 shows the real and imaginary parts of the

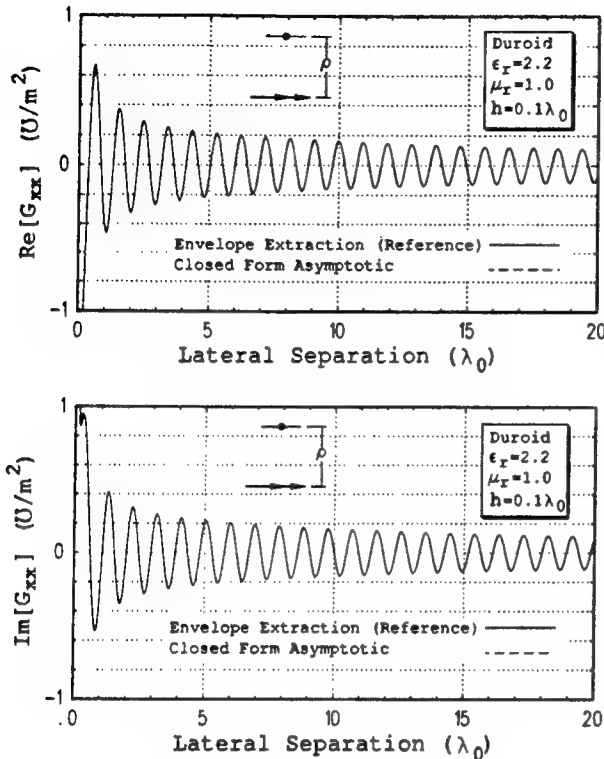


Figure 9. Comparison of closed-form uniform asymptotic G_{xx} component of the dyadic Green's function with "exact" solution computed using the envelope extraction technique. Cut taken in direction of surface wave peak. The parameters $\epsilon_r = 2.2$, $\mu_r = 1.0$, and $h = 0.1\lambda_0$.

G_{xx} component of the dyadic Green's function, \tilde{G} , in the direction of the surface wave null (endfire). The solid lines are the numerical reference solutions, and the dotted lines are the closed-form asymptotic solutions. As we can see, the agreement is excellent for source and field point separations down to a third of a free space wavelength or so. Figure 9 also shows the real and imaginary parts of the G_{xx} component of the dyadic Green's function, \tilde{G} , for the same structure, but this is for the broadside direction along which the lone surface wave propagates. It is evident that the agreement is again excellent, and the closed-form asymptotic solution in this case also proves accurate down to approximately a third of a free space wavelength.

The next case under consideration has a relative permittivity of 9.6, a relative permeability of 1.0, and a dielectric thickness of 0.05 free space wavelengths. As in the previous case there is only one pole in each of TM and TE integrals that need to be

considered [Marin *et al.*, 1990]. Figures 10 and 11 show the comparisons between the numerical and closed-form uniform asymptotic solutions of the G_{xx} component of the dyadic Green's function for the endfire and broadside separations, respectively. The agreement is better than for the previous set of examples in that there appears to be a deviation between the two solutions for source and field point spacings less than 0.2 of a free space wavelength.

The third and final case shown in Figures 12 and 13 is one where there are two poles that influence the TE SDP evaluation and one that influences the TM SDP evaluation. The communication [Marin *et al.*, 1990] predicts that only one TE pole needs to be taken into account; however, we found that two TE poles must be incorporated into the analysis to obtain accurate results. The relative permittivity is 2.2, the relative permeability is 1.0, and the material thickness is 0.2 free space wavelengths. By comparison with the previous two cases there is much

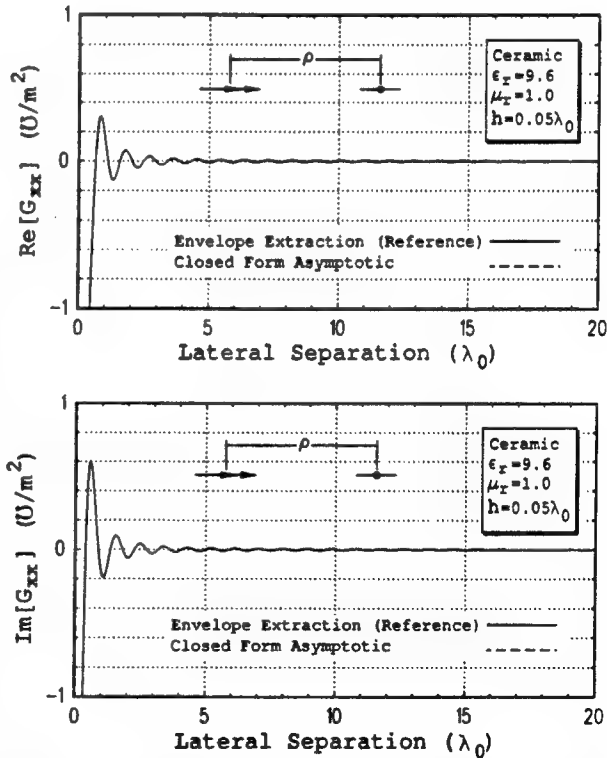


Figure 10. Comparison of closed-form uniform asymptotic G_{xx} component of the dyadic Green's function with "exact" solution computed using the envelope extraction technique. Cut taken in direction of surface wave null. The parameters $\epsilon_r = 9.6$, $\mu_r = 1.0$, and $h = 0.05\lambda_0$.

stronger interference between the various (space wave and pole wave) radiation mechanisms. The influence of these mechanisms is more evident in this case because two TE leaky wave poles are close to the saddle point in the spectral domain. Once again, the agreement is excellent down to a lateral source and field point separation of approximately one third of a free space wavelength.

The major advantage of the closed-form uniform asymptotic evaluation of the Green's function is the computational time savings compared to numerical integration techniques. The CPU time to compute all four Sommerfeld integrals (i.e., all components of the dyadic Green's function) is tabulated in Table 1 for various lateral separations of the source and observation points. It is clear that the closed-form uniform asymptotic representation offers significant computational time savings compared to numerical integration. As the lateral separation increases, the computation time of the numerical integration

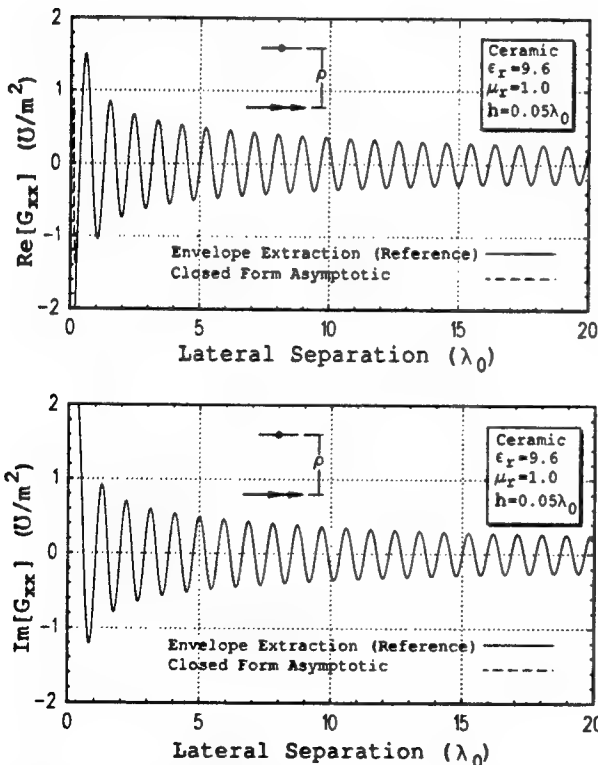


Figure 11. Comparison of closed-form uniform asymptotic G_{xx} component of the dyadic Green's function with "exact" solution computed using the envelope extraction technique. Cut taken in direction of surface wave peak. The parameters $\epsilon_r = 9.6$, $\mu_r = 1.0$, and $h = 0.05\lambda_0$.

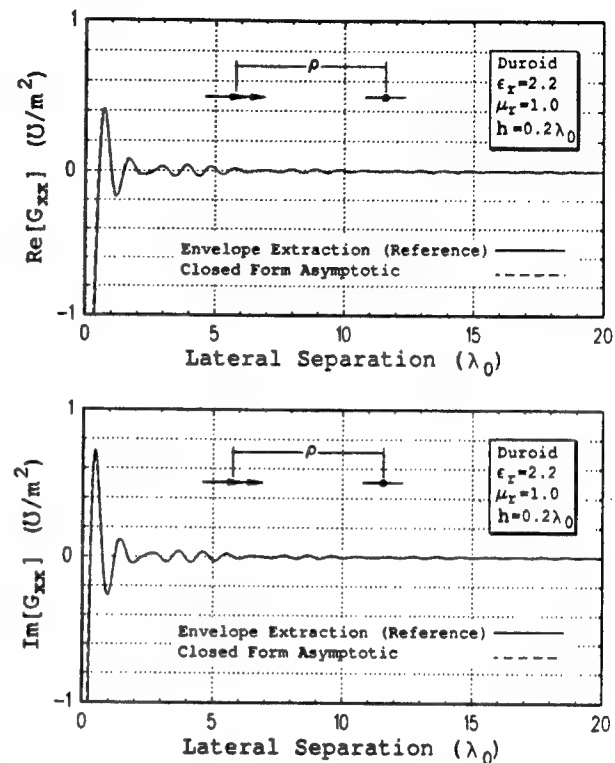


Figure 12. Comparison of closed-form uniform asymptotic G_{xx} component of the dyadic Green's function with "exact" solution computed using the envelope extraction technique. Cut taken in direction of surface wave null. The parameters $\epsilon_r = 2.2$, $\mu_r = 1.0$, and $h = 0.2\lambda_0$.

grows without bound, whereas the computation time of the asymptotic solution remains constant. This along with the high degree of accuracy makes the closed-form uniform asymptotic solution ideal for the analysis of not only large slotted material coated planar structures but also for relatively small structures.

In summary, two methods of computing the dyadic aperture Green's function \tilde{G} of (2) were presented. One was a numerical evaluation of the exact integral representation which is valid for all values of lateral separation of the source and observation points. This solution incorporates the envelope and singularity extraction techniques to enhance the computation efficiency. The second solution and the major contribution of this paper is a closed-form uniform asymptotic representation that is valid for large lateral source and field point separations; however, it was shown to remain valid for lateral separations down to a half of a free space wave-

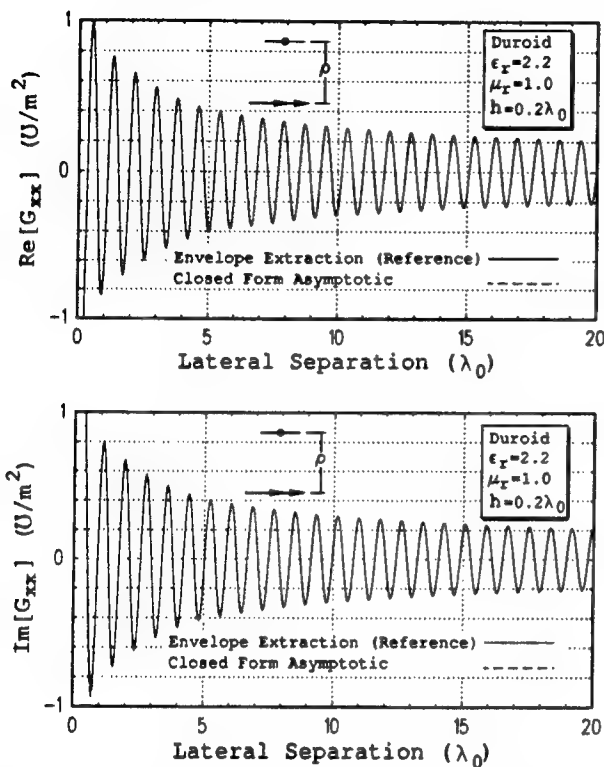


Figure 13. Comparison of closed-form uniform asymptotic G_{xx} component of the dyadic Green's function with "exact" solution computed using the envelope extraction technique. Cut taken in direction of surface wave peak. The parameters $\epsilon_r = 2.2$, $\mu_r = 1.0$, and $h = 0.2\lambda_0$.

length and even two tenths of a free space wavelength in some cases. This asymptotic solution is at least 2 to 3 orders of magnitude computationally more efficient than the numerical representation for distances characteristic of large arrays. The combination of these two solutions is ideal for the efficient calculation of the aperture dyadic Green's function,

Table 1. CPU Time (Milliseconds on a VAX 8550) to Calculate All Elements of the Aperture Dyadic Green's Function for the Case of $\epsilon_r = 9.6$, $\mu_r = 1.0$ and $h = 0.05\lambda_0$

Lateral Distance, $\mu\lambda_0$	CPU Time Numerical Integration	CPU Time Closed-Form Asymptotic
0.5	141	0.84
1.0	228	0.84
2.0	335	0.84
10.0	991	0.84

\tilde{G} , for the entire range of lateral separation. The results developed here can be used for a variety of slot/feed geometries containing material layers below (substrate) and a material layer above (superstrate) the slots in a PEC ground plane.

Acknowledgments. This work was supported in part by an Ohio Aerospace Institute/NASA space grant doctoral fellowship and in part by the Joint Services Electronics Program under contract N00014-89-J-1007.

References

- Barkeshli, S., P. H. Pathak, and M. Marin, An asymptotic closed form microstrip surface Green's function for the efficient moment method analysis of mutual coupling in microstrip antenna arrays, *IEEE Trans. Antennas Propag.*, 38(9), 1374-1383, 1990.
- Clemmow, P. C., Some extensions to the method of integration by steepest descents, *Q. J. Mech. Appl. Math.*, 3, 241-256, 1950.
- Felsen, L. B., and N. Marcuvitz, *Radiation and Scattering of Waves*, Prentice-Hall, Englewood Cliffs, New Jersey, 1973.
- Hwang, Y. M., and R. G. Kouyoumjian, A dyadic diffraction coefficient for an electromagnetic wave which is rapidly varying at an edge, paper presented at USNC-URSI 1974 Annual Meeting, Boulder, Colo., Union Radio Scientifique Internationale, Paris, February 19-23, 1974.
- Jackson, D. R., and N. G. Alexopoulos, An asymptotic extraction technique for evaluating Sommerfeld-type integrals, *IEEE Trans. Antennas Propag.*, 34, 1467-1470, 1986.
- Kouyoumjian, R. G., and P. H. Pathak, A uniform geometrical theory of diffraction for an edge in a perfectly conducting surface, *Proc. IEEE*, 62, 1448-1461, 1974.
- Marin, M. A., and P. H. Pathak, An asymptotic closed-form representation for the grounded double-layer surface Green's function, *IEEE Trans. Antennas Propag.*, 40(11), 1-10, 1992.
- Marin, M. A., S. Barkeshli, and P. H. Pathak, On the location of proper and improper surface wave poles for the grounded dielectric slab, *IEEE Trans. Antennas Propag.*, 38(4), 570-573, 1990.
- Marin, M. A., S. Barkeshli, and P. H. Pathak, Efficient analysis of planar microstrip geometries using an asymptotic closed-form of the grounded dielectric slab Green's function, *IEEE Trans. Microwave Theory Tech.*, 37(4), 669-678, 1989.
- Pathak, P. H., and R. G. Kouyoumjian, The dyadic diffraction coefficient for a perfectly conducting wedge, *Rep. 2183-4*, ElectroSci. Lab., Dep. Electr. Eng., The Ohio State Univ., Columbus, Ohio, June 1970.

Pozar, D. M., Improved computational efficiency for the moment method solution of printed dipoles and patches, *Electromagnetics*, 3, 299-399, 1984.

Pozar, D. M., Analysis of finite phased arrays of printed dipoles, *IEEE Trans. Antennas Propag.*, 33(10), 1045-1053, 1985.

Tai, C. T., On the eigenfunction expansion of dyadic Green's functions, *Proc. IEEE*, 61, 480-481, 1973.

Van der Waerden, B. L., On the method of saddle points, *Appl. Sci. Res.*, B2, 33-45, 1951.

P. H. Pathak, The Ohio State University, Electro-Science Laboratory, 1320 Kinnear Road, Columbus, OH 43212.

G. A. Sodiers, Lincoln Laboratory, Massachusetts Institute of Technology, 244 Wood Street, Lexington, MA 02173.

(Received April 6, 1993; accepted June 23, 1993.)

EM PLANE-WAVE DIFFRACTION BY A MATERIAL-COATED PERFECTLY CONDUCTING HALF-PLANE—OBLIQUE INCIDENCE

H. C. Ly and R. G. Rojas
The ElectroScience Laboratory
Department of Electrical Engineering
The Ohio State University
Columbus, Ohio 43212

KEY TERMS

Coated half-plane, diffraction, Wiener-Hopf, generalized impedance boundary conditions

ABSTRACT

A high-frequency solution is developed for the electromagnetic diffraction of an obliquely incident plane wave by a material-coated perfectly conducting half-plane. It is assumed that the coating is electrically thin so that it can be modeled by a generalized impedance boundary condition of $O(t)$, where t is the coating's thickness.
© 1994 John Wiley & Sons, Inc.

1. INTRODUCTION

The canonical problem to be studied is the high-frequency electromagnetic (EM) diffraction by a material-coated per-

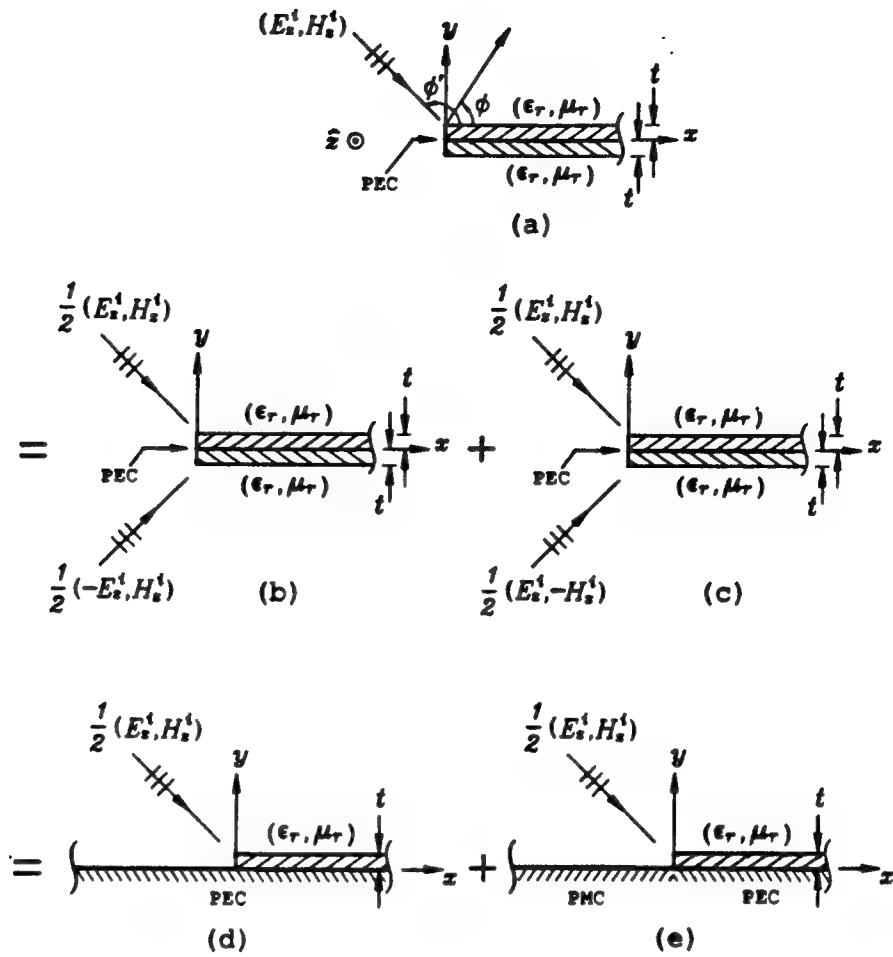


Figure 1 Material-coated PEC half-plane geometry and equivalent configurations

fectly conducting (PEC) half-plane, with the same coatings on the top face $\{x > 0, y = 0^\circ\}$ and the bottom face $\{x > 0, y = 0^\circ\}$. The incident field is a plane wave of arbitrary polarization obliquely incident to the z axis with an angle θ' ($0 < \theta' < \pi$). The geometry pertaining to this problem is shown in Figure 1(a), with ϕ and ϕ' being the scattered and incident angles, respectively. It is important to keep in mind that the half-plane being considered here is opaque, whereas the one considered in Section V of [1] is transparent.

For the coated PEC half-plane depicted in Figure 1(a) with the same material coating on both faces $\{y = 0^\circ\}$, the geometry is symmetrical about the $y = 0$ plane. Hence, the coated half-plane may be decomposed into two equivalent configurations by first expressing the incident field (E_x^i, H_z^i) as a superposition of the even and odd symmetrical components [Figures 1(b) and 1(c)]. These configurations are in turn equivalent (for $y > 0$) to the ones shown in Figures 1(d) and 1(e): a PEC ground plane with semi-infinite coating and a coated PEC half-plane joined with a PMC (perfectly magnetic conducting) half-plane. Note that the latter geometry is not considered in [1]. The solution to the geometry in Figure 1(a) may then be obtained via a superposition of the results for Figures 1(d) and 1(e).

The coating's thickness t is assumed to be electrically small, so that the employment of a generalized impedance boundary condition (GIBC) of $0(t)$ provides an accurate model for the coated half-plane. This GIBC of $0(t)$ may be expressed as

follows ($\hat{n} = \pm\hat{y}$, $y \geq 0$) [2]:

$$\begin{aligned} \left\{ 1 \pm t \left(1 - \frac{1}{\epsilon_r} \right) \frac{\partial}{\partial y} \right\} \hat{n} \times \hat{n} \times \bar{E}(y = 0^\circ) \\ = -ik\eta_0 t \left(\frac{1}{\epsilon_r} - \mu_r \right) \hat{n} \times \bar{H}(y = 0^\circ), \quad x > 0. \quad (1) \end{aligned}$$

where η_0 and k are, respectively, the free-space impedance and wave number. Note that the GIBC of $0(t)$ given above can be rewritten in terms of the z -component fields E_z and H_z only, because the planar geometry in Figure 1(a) is two dimensional, though the incidence is oblique. Also, it has been shown by Ly, Rojas, and Pathak [1] that a complete solution for a boundary-value problem involving GIBC of $0(t)$ can be obtained by imposing a junction (or contact) condition which may be found via a quasistatic analysis. This junction condition is applied in addition to the well-known edge condition. The solution thus obtained automatically satisfies reciprocity even for the case of oblique incidence.

II. PEC GROUND PLANE WITH A SEMI-INFINITE MATERIAL COATING

The partially coated ground plane shown in Figure 1(d) is a special case of the more general two-part coated ground plane discussed by Ly et al. [1]. The configuration in Figure 1(d) is obtained from the one depicted in Figure 2 in [1] as the thick-

ness of the material coating (t_2) on the half-plane ($y = 0, x < 0$) shrinks to zero. Thus, by taking appropriate limits of the corresponding parameters in the solution for the two-part coated PEC ground plane analyzed in [1], one may obtain the spectral function $\tilde{\mathbf{S}}_2(w, \phi'; \theta')$ (i.e., the spectral scattered field in the w domain that would yield a spatial field via an inverse Fourier transform) for the partially coated ground plane as follows:

$$\tilde{\mathbf{S}}_2(w, \phi'; \theta') = \tilde{\mathbf{C}}(w) \tilde{\mathbf{V}}(w) \sin w \left[\frac{\tilde{\mathbf{A}}(w, \phi'; \theta')}{\cos w + \cos \phi'} + \tilde{\mathbf{B}}(w, \phi'; \theta') \right] \sin \phi' \tilde{\mathbf{V}}(\phi') \tilde{\mathbf{C}}(\phi') \tilde{\mathbf{F}}_{0z}, \quad (2)$$

where $\tilde{\mathbf{F}}_{0z} = [E_{0z} \ H_{0z}]$, E_{0z} and H_{0z} are, respectively, the magnitudes of the incident fields E_z^i and H_z^i at the origin. The matrices in (2) are defined as follows:

$$\tilde{\mathbf{C}}(w) = \frac{1}{\Delta(w)} \begin{bmatrix} -\cos w & \sin w \cos \theta' \\ \sin w \cos \theta' & \cos w \end{bmatrix}, \quad \Delta(w) = \cos^2 \theta' + \cos^2 w \sin^2 \theta'; \quad (3a)$$

$$\tilde{\mathbf{V}}(w) = \begin{bmatrix} g_+(w, \zeta) & 0 \\ 0 & g_+(w, \nu_a) g_+(w, \nu_b) / \left(\sqrt{2} \cos \frac{w}{2} \right) \end{bmatrix}, \quad (3b)$$

$$\tilde{\mathbf{A}}(w, \phi'; \theta') = \begin{bmatrix} A_{11} & 0 \\ 0 & A_{22} \end{bmatrix}, \quad \tilde{\mathbf{B}}(w, \phi'; \theta') = \begin{bmatrix} B_{11} & B_{12} \\ B_{21} & B_{22} \end{bmatrix}; \quad (3c)$$

in which

$$A_{11} = \sin^2 \theta' \cos w \cos \phi' - \cos^2 \theta', \quad (4a)$$

$$A_{22} = (\cos w \cos \phi' + \cos^2 w_0)(\cos^2 \theta' - \sin^2 \theta' \cos w \cos \phi')$$

$$+ (\cos w + \cos \phi') \left[\sin^2 \theta' \cos w \cos \phi' \frac{\cos w_0}{h(w_0)} + \cos^2 \theta' \left(\frac{\cos w \cos \phi'}{h(w_0) \cos w_0} - \cos w - \cos \phi' \right) \right], \quad (4b)$$

$$B_{11} = -\frac{i \cos \theta' [\mathfrak{L}(w_0^+) + \mathfrak{L}(w_0^-)] + h(w_0) \cos w_0 \sin \theta' [\mathfrak{L}(w_0^+) - \mathfrak{L}(w_0^-)]}{h(w_0) \cos w_0 \sin \theta' [\mathfrak{L}(w_0^+) + \mathfrak{L}(w_0^-)] + i \cos \theta' [\mathfrak{L}(w_0^+) - \mathfrak{L}(w_0^-)]} \cdot i \cos \theta' \sin \theta', \quad (4c)$$

$$B_{12} = -\frac{\sin \theta' \Delta(w_0) (1/\sin^2 \theta' + a/\sin \theta' + b)^{-1}}{h(w_0) \cos w_0 \sin \theta' [\mathfrak{L}(w_0^+) + \mathfrak{L}(w_0^-)] + i \cos \theta' [\mathfrak{L}(w_0^+) - \mathfrak{L}(w_0^-)]} \cdot 2 \cos \theta' [h(w_0) \cos w_0 - \cos \phi'], \quad (4d)$$

$$B_{21} = -\frac{\sin^2 \theta' (1/\sin \theta' + \sin \zeta)^{-1}}{h(w_0) \cos w_0 \sin \theta' [\mathfrak{L}(w_0^+) + \mathfrak{L}(w_0^-)] + i \cos \theta' [\mathfrak{L}(w_0^+) - \mathfrak{L}(w_0^-)]} \cdot 2 \cos \theta' [h(w_0) \cos w_0 - \cos w], \quad (4e)$$

$$B_{22} = -\frac{\mathfrak{L}(w_0^+) - \mathfrak{L}(w_0^-)}{h(w_0) \cos w_0 \sin \theta' [\mathfrak{L}(w_0^+) + \mathfrak{L}(w_0^-)] + i \cos \theta' [\mathfrak{L}(w_0^+) - \mathfrak{L}(w_0^-)]} \cdot [i \cos \theta' \Delta(w_0) / (h(w_0) \cos w_0)] [h(w_0) \cos w_0 - \cos \phi'] [h(w_0) \cos w_0 - \cos w] \quad (4f)$$

$$h(w_0) = \frac{a(1 - \cos w_0) g_+^2(w_0, \nu_a) g_+^2(w_0, \nu_b) + 1}{a(1 - \cos w_0) g_+^2(w_0, \nu_a) g_+^2(w_0, \nu_b) - 1}, \quad (4g)$$

$$\mathfrak{L}(w_0^{\pm}) = \frac{g_+(w_0^{\pm}, \nu_a) g_+(w_0^{\pm}, \nu_b) g_-(w_0^{\pm}, \zeta)}{\sqrt{2} \cos(w_0^{\pm}/2)}. \quad (4h)$$

Note that the expressions for the functions g_+ were summarized in [3] and are not repeated here. Also, $K = k \sin \theta'$, $\cos^2 w_0 = 1 + b$, $w_0^{\pm} = \pi/2 \pm i \ln(\cot(\theta'/2))$, and the re-

maining terms present in the above expressions are given by

$$\sin \zeta = \frac{i}{K(\mu_r - 1)t}, \quad \sin \nu_a = \frac{a}{2} \mp \sqrt{\left(\frac{a}{2}\right)^2 - b}, \quad (5a)$$

$$a = \sin \nu_a + \sin \nu_b = -\frac{i \epsilon_r}{K(\epsilon_r - 1)t},$$

$$b = \sin \nu_a \sin \nu_b = -\frac{\mu_r \epsilon_r - 1}{\sin^2 \theta' (\epsilon_r - 1)}. \quad (5b)$$

III. PLANAR JUNCTION OF COATED PEC HALF-PLANE WITH PMC HALF-PLANE

The geometry pertaining to this scattering problem is illustrated in Figure 1(e), where one half-plane is a PMC and the other is a coated PEC. Although this geometry is not considered in [1], it can still be obtained from the two-part material-coated PEC ground-plane geometry of Figure 2 in [1] by means of a key step. In other words, the coated PEC half-plane ($x < 0, y = 0$) in Figure 2 in [1] becomes a PMC half-

plane without any coating by applying the limits $t_2 \rightarrow 0$, and $(\mu_r - 1)t_2 \rightarrow \infty$ (which is the key step in this analysis) to the solution for the two-part material-coated PEC ground plane

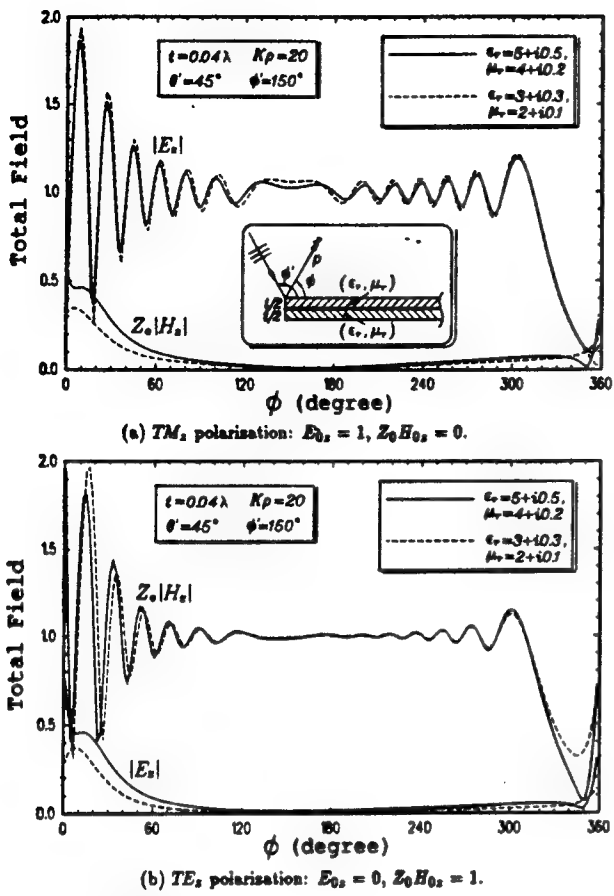


Figure 2 Total field for a material-coated PEC half-plane excited by an obliquely incident plane wave. (a) TM_z polarization: $E_{0z} = 1$, $Z_0 H_{0z} = 0$. (b) TE_z polarization: $E_{0z} = 0$, $Z_0 H_{0z} = 1$.

alluded to above. The above limits yield the following spectral field for the present problem:

$$\bar{\mathcal{F}}_z(w, \phi'; \theta') = \bar{\mathbf{C}}(w) \bar{\Psi}'(w) \sin w \left[\frac{\bar{\mathbf{A}}'(w, \phi'; \theta')}{\cos w + \cos \phi'} + \bar{\mathbf{B}}'(w, \phi'; \theta') \right] \cdot \sin \phi' \bar{\Psi}'(\phi') \bar{\mathbf{Z}} \bar{\mathbf{C}}(\phi') \bar{\mathbf{F}}_{0z}, \quad (6)$$

where the new matrices are defined by

$$\bar{\Psi}'(w) = \begin{bmatrix} g_+(w, \zeta) / \left(\sqrt{2} \cos \frac{w}{2} \right) & 0 \\ 0 & g_+(w, \nu_b) g_+(w, \nu_b) \end{bmatrix}, \quad (7a)$$

$$\bar{\mathbf{Z}} = \begin{bmatrix} -\sin \zeta & 0 \\ 0 & 1 \end{bmatrix}, \quad (7b)$$

$$\bar{\mathbf{A}}'(w, \phi'; \theta') = \begin{bmatrix} A'_{11} & 0 \\ 0 & A'_{22} \end{bmatrix}, \quad \bar{\mathbf{B}}'(w, \phi'; \theta') = \begin{bmatrix} B'_{11} & B'_{12} \\ B'_{21} & B'_{22} \end{bmatrix}, \quad (7c)$$

$$A'_{11} = \sin^2 \theta' \cos w \cos \phi' - \cos^2 \theta', \quad A'_{22} = a \sin^2 \theta' \cos w \cos \phi' - \cos^2 \theta', \quad (7d)$$

$$B'_{11} = -i \cos \theta' \sin \theta' \frac{\mathcal{L}'(w_\theta^+) - \mathcal{L}'(w_\theta^-)}{\mathcal{L}'(w_\theta^+) + \mathcal{L}'(w_\theta^-)}, \quad (7e)$$

$$B'_{12} = 2a \cos \theta' \sin \theta' \frac{(1/\sin^2 \theta' + a/\sin \theta' + b)^{-1}}{\mathcal{L}'(w_\theta^+) + \mathcal{L}'(w_\theta^-)}, \quad (7f)$$

$$B'_{21} = -2 \cos \theta' \sin^2 \theta' \frac{(1/\sin \theta' + \sin \zeta)^{-1}}{\mathcal{L}'(w_\theta^+) + \mathcal{L}'(w_\theta^-)}, \quad B'_{22} = ia \cos \theta' \sin \theta' \frac{\mathcal{L}'(w_\theta^+) - \mathcal{L}'(w_\theta^-)}{\mathcal{L}'(w_\theta^+) + \mathcal{L}'(w_\theta^-)}, \quad (7g)$$

$$\mathcal{L}'(w_\theta^\pm) = \frac{g_+(w_\theta^\pm, \nu_a) g_+(w_\theta^\pm, \nu_b) g_-(w_\theta^\pm, \zeta)}{\sqrt{2} \sin(w_\theta^\pm/2)}. \quad (7h)$$

IV. FINAL RESULT

A superposition of the spectral functions $\bar{\mathcal{F}}$ and $\bar{\mathcal{F}}'$ given in the previous sections yields the spectral field for the material-coated PEC half-plane with the same coatings on both faces. Using the steepest descent method to evaluate the inverse Fourier transform of the spectral field, one may express the total field for the coated PEC half-plane as a sum of the incident-, reflected-, diffracted-, and surface-wave fields. The diffracted field at the point $(\rho, \phi, \pi - \theta')$ may be written as

$$\bar{\mathcal{F}}_z^d = \left[\frac{E_z^{z=0}}{\eta_0 H_z^d} \right] \sim -\frac{e^{iKp/4}}{\sqrt{2\pi Kp}} e^{iKp - ikz \cos \theta'} \left\{ \bar{\mathbf{L}} \left[\bar{\mathcal{F}}_z(|\phi|, \phi'; \theta') \right. \right. \\ \left. \left. + \frac{|\phi|}{\phi'} \bar{\mathcal{F}}_z(|\phi|, \phi'; \theta') \right] + \sum_{i=1}^3 \bar{F}_i \frac{1 - F(-2K\rho\gamma_i^2)}{2\gamma_i} \right\}, \\ 0 < |\phi|, \quad \phi' < \pi, \quad (8)$$

where

$$\bar{\mathbf{L}} = \begin{bmatrix} 1 & 0 \\ 0 & |\phi|/\phi \end{bmatrix}, \quad \gamma_i = \sin \left(\frac{w_i - \phi}{2} \right), \\ i = 1, 2, 3, \quad (9)$$

and $w_1 = \pi - \phi'$, $w_2 = -\nu_b$, $w_3 = -\zeta$. The functions \bar{F}_i , $i = 1, 2, 3$, are the residues of the spectral function $\bar{\mathbf{L}}[\bar{\mathcal{F}}_z(w, \phi'; \theta') + |\phi|/\phi \bar{\mathcal{F}}_z(w, \phi'; \theta')]$ at the poles $w = w_i$. The residue \bar{F}_2 also produces a surface-wave field given by

$$\bar{\mathcal{F}}_z^w = -\bar{F}_2 e^{iKp \cos(\nu_b + i\delta) - ikz \cos \theta'} U(\phi_s - |\phi|), \quad (10)$$

where $\phi_s = -\text{Re } \nu_b + \arccos[1/\cosh(\text{Im } \nu_b)]$. The geometrical optics fields are not included here due to space limitations. A numerical example based on the high-frequency solution obtained above is shown in Figure 2, where the plane wave is obliquely incident ($\theta' = 45^\circ$) to the edge of the coated half-plane. Both fields E_z and H_z are excited by the incident field of either TM_z or TE_z polarization, though the cross-polarized field appears small for most scattering aspects. The effect of the surface wave can clearly be seen in Figure 2 around $\phi = 360^\circ$, where the total field starts to increase in

magnitude due to the surface wave field, especially for the case of larger ϵ_r and μ_r . Note that as the oblique incidence becomes normal incidence (i.e., $\theta' \rightarrow 90^\circ$), the result obtained here reduces to the Maliuzhinets-based solution developed by Ly and Rojas [4] when the expressions in [4] are simplified to the special case of equal coatings on both faces of the half-plane. The accuracy of the two-part material slab solution from which the present solution is obtained has been verified in [1] using a dependent moment-method solution as a reference.

ACKNOWLEDGMENTS

This work was supported in part by the Joint Services Electronics Program (Contract No. N00014-89-J-1007) and by the Ohio State University Research Foundation.

REFERENCES

1. H. C. Ly, R. G. Rojas, and P. H. Pathak, "EM Plane Wave Diffraction by a Planar Junction of Two Thin Material Half-Planes—Oblique Incidence," *IEEE Trans. Antennas Propagat.*, Vol. AP-41, April 1993, pp. 429–441.
2. R. G. Rojas and L. M. Chou, "Generalized Impedance/Resistive Boundary Conditions for a Planar Chiral Slab," *1991 IEEE APS/URSI International Symposium*, London, Ontario, Canada, June 1991.
3. R. G. Rojas and P. H. Pathak, "Diffraction of EM Waves by a Dielectric/Ferrite Half-plane and Related Configurations," *IEEE Trans. Antennas Propagat.*, Vol. AP-37, June 1989, pp. 751–763.
4. H. C. Ly and R. G. Rojas, "Analysis of Diffraction by Material Discontinuities in Thin Material Coated Planar Surfaces Based on Maliuzhinets Method," *Radio Sci.*, Vol. 28, May–June 1993, pp. 281–297.

Received 11-17-93

Microwave and Optical Technology Letters, 7/6, 262–266
© 1994 John Wiley & Sons, Inc.
CCC 0895-2477/94

Integral Equation Analysis of a Sheet Impedance Coated Window Slot Antenna

R. Torres and E. H. Newman

Abstract—This paper will present an integral equation and method of moments analysis of a window slot antenna. The antenna is modeled by a sheet admittance coated rectangular aperture in an infinite ground plane. It is shown that the sheet admittance coated aperture is complementary to a sheet impedance plate, which permits the window slot antenna to be analyzed with existing computer programs. Numerical results are compared with measurements for input impedance and radiation efficiency.

I. INTRODUCTION

This paper will present an integral equation and method of moments (MM) [1] solution for a recently developed rectangular slot antenna, which can be mounted in the outer perimeter of a window [2], [3]. A conventional slot antenna consists of a slot or gap cut in a perfectly conducting ground plane [4], [5]. If the cross-hatched regions of Fig. 1 are considered to be perfectly conducting surfaces, then Fig. 1 represents a conventional rectangular slot antenna placed in the outer perimeter of a rectangular window. The problem with this design is that it is not possible to see through the window since it has been covered with a perfect conductor. Recently, Torres and Walton have solved this problem by replacing the inner perfectly conducting patch by a resistive surface of typically $4-8 \Omega/\square$ [2], [3]. These resistive surfaces can be made almost transparent at optical frequencies, and yet have low enough resistance to serve as a reasonable ground plane for the slot antenna. For example, Torres and Walton designed an automobile windshield slot antenna which is typically 5 dB below the standard whip in the FM band, but about 3 dB above the whip in the AM band.

The next section develops an integral equation for a sheet admittance coated aperture in an infinite ground plane, which serves as an idealized model for the window slot antenna since it neglects antenna/automobile interactions. Next, it is shown that the sheet admittance coated aperture is complementary to a sheet impedance plate, which allows the window antenna to be analyzed with existing computer codes [6]. Finally, numerical results are compared with measurements for the input impedance and radiation efficiency of the window slot antenna.

II. THEORY

A. Introduction

This section will develop an integral equation for a sheet impedance coated slot antenna. As illustrated in Fig. 1, the antenna consists of a rectangular aperture of width W and height L in an infinite perfectly conducting ground plane. The outer edge of the rectangular aperture contains a gap of width g and of sheet impedance Z_{sg} , while the remaining center section (window) of the aperture contains the sheet impedance Z_{sc} . The term sheet impedance implies a generalization of a resistive surface, where the resistivity may be complex.

Manuscript received September 8, 1992; revised June 9, 1993.

The authors are with the ElectroScience Laboratory, Ohio State University, Columbus, OH 43212 USA.

IEEE Log Number 9400499.

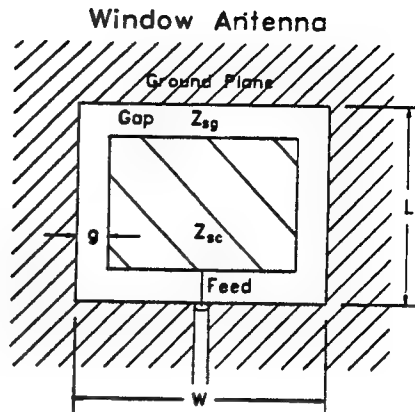


Fig. 1. Geometry for a sheet impedance coated window antenna.

A sheet impedance is a zero thickness model for an electrically thin dielectric slab [7]–[14]. In particular, an electrically thin dielectric slab of thickness T , relative permittivity, ϵ_r , conductivity σ , and complex permittivity $\epsilon = \epsilon_r \epsilon_0 - j(\sigma/\omega)T$ has sheet impedance

$$Z_s = \frac{1}{j\omega(\epsilon - \epsilon_0)T} (\Omega/\square) \quad (1)$$

where ϵ_0 is the permittivity of free space and ω is the radian frequency. Note that for a lossless dielectric, ϵ is pure real, and thus Z_s is pure imaginary. By contrast, for a very lossy dielectric, $\sigma/\omega \gg \epsilon_r \epsilon_0$, and $Z_s = 1/\sigma T$ is pure real. A pure real Z_s is commonly referred to as a resistive surface or a space cloth. A surface of zero sheet impedance is a perfectly conducting surface, while an infinite sheet impedance corresponds to the absence of the dielectric slab. If $Z_{sg} = \infty$ and $Z_{sc} = 0$, then the antenna of Fig. 1 would be a conventional rectangular slot antenna. The volume equivalence [15] can be used to show that the sheet impedance surface can be replaced by free space and the equivalent electric surface current

$$\mathbf{J} = \mathbf{E}/Z_s \quad (2)$$

where \mathbf{E} is the electric field at the surface of the sheet impedance. It is implicit that (2) applies only to the components of \mathbf{E} and \mathbf{J} which are tangential to the sheet impedance surface.

For multilayer dielectrics, the individual sheet impedance of the layers appear as impedances in parallel. For example, the sheet admittance of a two-layer electrically thin dielectric slab is simply [8]

$$Y_s = \frac{1}{Z_s} = Y_{s1} + Y_{s2} = j\omega(\epsilon_1 - \epsilon_0)T_1 + j\omega(\epsilon_2 - \epsilon_0)T_2 (\Omega/\square) \quad (3)$$

where ϵ_1 and T_1 or ϵ_2 and T_2 are the permittivity and thickness of layer 1 or 2, respectively. Equation (3) can be used to determine the sheet impedance of a thin plastic window coated with a resistive film.

B. Sheet Admittance Aperture Integral Equation

Fig. 2(a) shows the side view of a planar aperture A in an infinite and perfectly conducting ground plane. The regions above and below the ground plane will be referred to as Regions a and b , respectively. An infinitesimal distance δ above or below the aperture are the nonuniform sheet admittances Y_{sa} and Y_{sb} , respectively. The

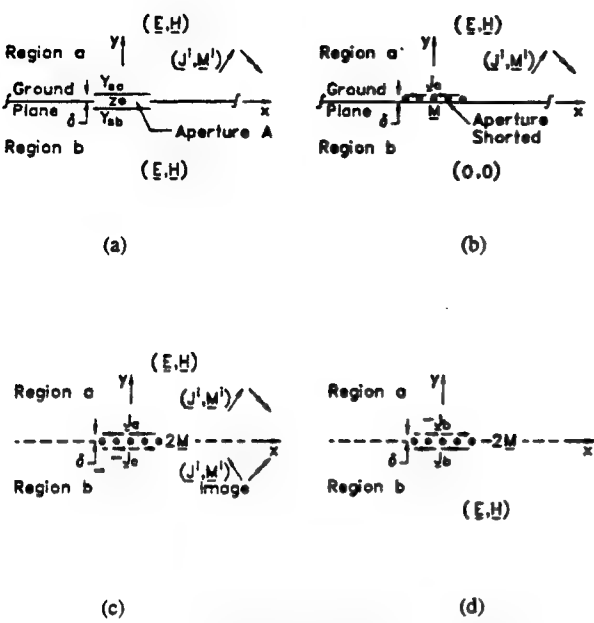


Fig. 2. (a) An aperture coated with a sheet admittance. (b) and (c) Equivalent problems in Region *a*. (d) An equivalent problem in Region *b*.

excitation is by the impressed currents (J^i, M^i) which are assumed to be in Region *a*. (J^i, M^i) produce the unknown total fields (E, H) in either Regions *a* or *b* when radiating in the presence of the aperture and the sheet admittances, and the assumed known incident fields (E^i, H^i) in free space. In this paper, all fields and currents are time harmonic, with the $e^{j\omega t}$ time dependence suppressed.

Following the usual procedure [16], the first step in deriving the aperture integral equation is to construct equivalent problems in Regions *a* and *b*. An equivalent problem for Region *a* is shown in Fig. 2(b) in which the aperture is shorted and the magnetic surface current

$$M = E \times \hat{y} \text{ in } A \quad (4)$$

is placed just above the aperture. Also, (2) is used to replace the sheet admittance Y_{sa} by free space and the equivalent electric surface current

$$J_a = Y_{sa} E \text{ (comp. tang. to } A\text{).} \quad (5)$$

In the equivalent problem of Fig. 2(b), the superposition of the fields of (J^i, M^i), M , and J_a , radiating in the presence of the infinite perfectly conducting ground plane, produce the proper total fields (E, H) above the ground plane and a null field below the ground plane. In the free space equivalent problem of Fig. 2(c), image theory has been used to remove the ground plane and replace it with the images of the above currents. In Region *a* of the free space equivalent problem of Fig. 2(c), the total fields (E, H) are produced by the superposition of the free space fields of the currents (J^i, M^i), and M , and J_a plus their images. Following the same procedure, Fig. 2(d) shows the free space equivalent problem in Region *b*. In Region *b*, the total fields are produced by the superposition of the free space fields of the magnetic surface current $-2M$ located in *A*, the electric surface current

$$J_b = Y_{sb} E \text{ (comp. tang. to } A\text{)} \quad (6)$$

located a distance δ below the aperture, and the current $-J_b$ located a distance δ above the aperture.

The aperture integral equation is an expression of continuity of the total tangential magnetic field across the aperture. Referring to the

free space equivalent problems of Fig. 2(c) and (d),

$$\begin{aligned} & H^i + H^{img} + H(2M) + \{H[J_a(\text{at } y = \delta)] \\ & + H[-J_a(\text{at } y = -\delta)]\} \\ & = H(-2M) + \{H[-J_b(\text{at } y = \delta)] \\ & + H[J_b(\text{at } y = -\delta)]\} \text{ (tang. in } A\text{)} \end{aligned} \quad (7)$$

where H^{img} is the free space magnetic field of the image impressed currents. At almost every point in space, the electromagnetic fields of $J_a(\text{at } y = \delta)$ are exactly cancelled by the image currents $-J_a(\text{at } y = -\delta)$. The one exception is for field points in the aperture *A* where boundary conditions can be used to show that the free space tangential magnetic fields of $J_a(\text{at } y = \delta)$ and $-J_a(\text{at } y = -\delta)$ are identical and equal to $\hat{y} \times J_a/2$. Then, using (2) and (4),

$$\begin{aligned} & H[J_a(\text{at } y = \delta)] + H[-J_a(\text{at } y = -\delta)] \\ & = \hat{y} \times J_a = \hat{y} \times Y_{sa} E = -Y_{sa} M. \end{aligned} \quad (8)$$

Similarly,

$$\begin{aligned} & H[-J_b(\text{at } y = \delta)] + H[J_b(\text{at } y = -\delta)] \\ & = -\hat{y} \times J_b = -\hat{y} \times Y_{sb} E = Y_{sb} M, \end{aligned} \quad (9)$$

and where it is emphasized that (8) and (9) apply to the tangential components in *A*. Inserting (8) and (9) into (7), and using the fact that in the plane of the aperture the tangential components of H^i and H^{img} are equal yields

$$2H(2M) - (Y_{sa} + Y_{sb})M = -2H^i \text{ (tang. in } A\text{).} \quad (10)$$

As expected, M does not depend upon how the sheet admittance is distributed above or below the aperture, but instead is dependent upon the sum or parallel combination of the sheet admittances Y_{sa} and Y_{sb} . Defining the net sheet admittance as

$$Y_s = Y_{sa} + Y_{sb}, \quad (11)$$

(10) becomes

$$H(2M) - \frac{Y_s}{4}(2M) = -H^i \text{ (tang. in } A\text{).} \quad (12)$$

Equation (12) is the desired integral equation for the equivalent magnetic surface current representing the sheet admittance coated aperture. Note that it has been written in terms of $2M$ rather than M since the scattered fields are the free space fields of $+2M$ or $-2M$ in Regions *a* or *b*, respectively.

C. Complementary Sheet Impedance Plate

This section will show that the integral equation for the sheet admittance coated aperture, (12), is complementary to that of a sheet impedance plate. This comparison is useful since it is a relatively simple matter to modify one of the many existing MM computers for perfectly conducting plates so that they can treat sheet impedance plates [16].

Consider electric and magnetic currents related by $J' = M'/\eta$. Directly from Maxwell's equations it can be shown that the electromagnetic fields of J' and M' , in a homogeneous medium with characteristic impedance η , are simply related by

$$E(J') = \eta H(M') \text{ and } H(J') = -E(M')/\eta. \quad (13)$$

Defining the complementary electric surface current density as $J_c = -2M/\eta$, using (13), and multiplying by η , (12) becomes

$$-E(J_c) + \frac{\eta^2 Y_s}{4} J_c = -\eta H^i \text{ (tang. in } A\text{).} \quad (14)$$

Now, consider a sheet impedance plate, with sheet impedance Z_{sp} on the plate surface S , and excited by the impressed currents (J_p^i, M_p^i),

with free space fields (E_p^i, H_p^i). J_p is given by the sheet impedance integral equation [7]–[14]

$$-E(J_p) + Z_{sp}J_p = E_p^i \text{ (tang. on } S\text{).} \quad (15)$$

Assuming that the impressed currents for the sheet impedance plate are the complement of those for the sheet admittance aperture, i.e., $(J_p^i, M_p^i) = (-M^i/\eta, \eta J^i)$, then the incident fields will be related by

$$(E_p^i, H_p^i) = (-\eta H^i, E^i/\eta). \quad (16)$$

In this case, (15) becomes

$$-E(J_p) + Z_{sp}J_p = -\eta H^i \text{ (tang. on } S\text{),} \quad (17)$$

Comparing (14) and (17) shows that if the aperture area A is identical to the plate surface S and

$$Z_{sp} \text{ (sheet impedance plate)} = \frac{\eta^2}{4} Y_s \text{ (sheet admittance aperture),} \quad (18)$$

then

$$J_p = J_c = -2M/\eta. \quad (19)$$

That is, the equivalent magnetic surface current $2M$, representing the sheet admittance aperture, is the complement of the equivalent electric surface current J_p , representing the complementary sheet impedance plate.

III. NUMERICAL RESULTS

This section will present numerical results for the input impedance and radiation efficiency of the window slot antenna. All numerical results were obtained by solving the complementary equation (15) with the authors' *Electromagnetic Surface Patch Code: ESP IV* [6]. Referring to Fig. 1, all data are for a window slot antenna of dimensions $W = L = 31$ mm and with an air gap ($Z_{sg} = \infty$) of width $g = 1$ mm. For the measured results, the infinite perfectly conducting ground plane was simulated with a 90 cm^2 aluminum plate.

Fig. 3 shows a comparison of the computed (solid line) and measured (dashed line) input impedance of the window slot antenna for inner patches of resistivity $Z_{sc} = 0, 25 \Omega/\text{sq}$, and $200 \Omega/\text{sq}$ from 2500 to 3200 MHz. Over this frequency range, the total gap length varies from 1λ to 1.28λ .

Fig. 4 shows a comparison of computed and measured (using the Wheeler cap method [17]) radiation efficiency as a function of the resistivity of the inner patch at $f = 2.5$ GHz. Measured values were obtained only for $Z_{sc} = 25 \Omega/\text{sq}$ and $200 \Omega/\text{sq}$, and are in reasonable agreement with computations. As expected, as the resistivity of the inner patch increases from the zero resistance of a perfectly conducting surface, the radiation efficiency decreases. However, for very large resistivity, the resistance patch is essentially approaching free space, and the efficiency begins to increase.

IV. SUMMARY

This paper has presented an integral equation and method of moments solution for a window slot antenna. The window slot antenna is modeled by a rectangular aperture with a sheet admittance coating. It is shown that the sheet admittance aperture is complementary to a sheet impedance plate, which permits the window slot antenna to be analyzed with existing computer codes [6]. Numerical results for the input impedance and radiation efficiency are found to be in reasonable agreement with measurements.

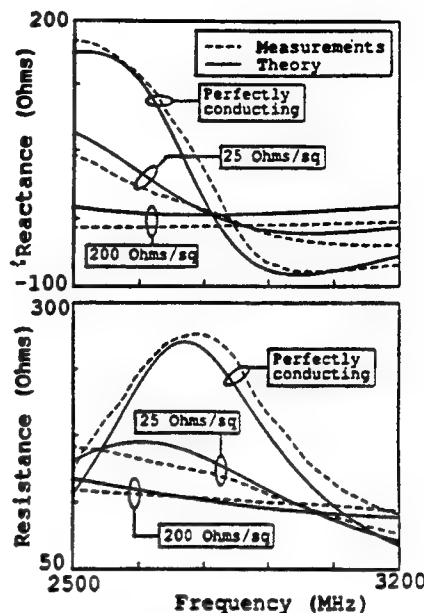


Fig. 3. Comparison of measured and computed input impedance versus frequency for a window slot antenna with resistivity $Z_{sc} = 0, 25 \Omega/\text{sq}$, and $200 \Omega/\text{sq}$ for the inner patch.

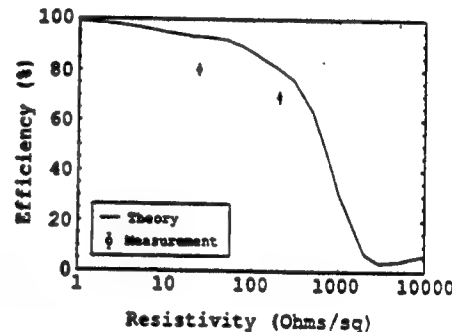


Fig. 4. Comparison of measured and computed radiation efficiency versus the resistivity of the inner patch at $f = 2.5$ GHz.

REFERENCES

- [1] R. F. Harrington, *Field Computations by Moment Methods*. New York: Macmillan, 1968.
- [2] R. Torres, "Analysis and design of a resistively coated windshield slot antenna," Ph.D. dissertation, Dep. Elec. Eng., Ohio State Univ., 1991.
- [3] R. Torres and E. K. Walton, "Analysis and design of a resistively coated windshield antenna," Ohio State Univ., ElectroSci. Lab. Rep. 312559-1, prepared under Contract AA317 C2035 with PPG Industries Inc., Pittsburgh, PA, June 1991.
- [4] J. D. Kraus, *Antennas*. New York: McGraw-Hill, 1988, ch. 13.
- [5] R. C. Johnson and H. Jasik, *Antenna Engineering Handbook*. New York: McGraw-Hill, 1984, ch. 8.
- [6] E. H. Newman, *A User's Manual for the Electromagnetic Surface Patch Code: ESP Version IV*, Ohio State Univ., ElectroSci. Lab. Rep. 716199-11, prepared under Grant NSG-1498 with NASA Langley Res. Cen., Aug. 1988.
- [7] L. N. Medgyesi-Mitschang and J. M. Putman, "Integral equation formulation for imperfectly conducting scatterers," *IEEE Trans. Antennas Propagat.*, vol. AP-33, pp. 206–214, Feb. 1985.
- [8] E. H. Newman and J. L. Blanchard, "TM scattering by an impedance sheet extension of a parabolic cylinder," *IEEE Trans. Antennas Propagat.*, vol. 36, pp. 527–534, Apr. 1988.
- [9] T. B. A. Senior and J. L. Volakis, "Sheet simulation of a thin dielectric layer," *Radio Sci.*, vol. 22, pp. 1261–1272, Dec. 1987.

- [10] R. F. Harrington and J. R. Mautz, "An impedance sheet approximation for thin dielectric shells," *IEEE Trans. Antennas Propagat.*, vol. AP-23, pp. 531-534, July 1975.
- [11] T. B. A. Senior, "Backscattering from resistive strips," *IEEE Trans. Antennas Propagat.*, vol. AP-27, pp. 808-803, Nov. 1979.
- [12] —, "Some extensions of Babinet's principle in electromagnetic theory," *IEEE Trans. Antennas Propagat.*, vol. AP-25, pp. 417-420, May 1977.
- [13] —, "Combined resistive and conductive sheets," *IEEE Trans. Antennas Propagat.*, vol. AP-33, pp. 577-579, May 1985.
- [14] E. H. Newman and M. R. Schrote, "An open surface integral formulation for electromagnetic scattering by material plates," *IEEE Trans. Antennas Propagat.*, vol. AP-32, pp. 672-678, July 1984.
- [15] C. A. Balanis, *Advanced Engineering Electromagnetics*. New York: Wiley, 1989, sect. 7.7.
- [16] R. F. Harrington and J. R. Mautz, "A generalized network formulation for aperture problems," *IEEE Trans. Antennas Propagat.*, vol. AP-24, pp. 870-873, Nov. 1976.
- [17] E. H. Newman, P. Bohley, and C. H. Walter, "Two methods for the measurement of antenna efficiency," *IEEE Trans. Antennas Propagat.*, vol. AP-23, pp. 457-461, July 1975.

Integral Equation Analysis of Artificial Media

J. L. Blanchard, E. H. Newman, and M. E. Peters

Abstract—This paper presents an integral equation and method of moments (MM) solution to determine the effective permittivity and permeability of an artificial medium. The artificial medium is modeled as a triple infinite periodic array of identical scattering elements. A plane wave of unknown phase constant is assumed to propagate in the periodic medium in a given direction, and the periodic moment method (PMM) is used to set up a matrix equation for the currents on the center element of the periodic array. By setting the determinant of the PMM impedance matrix to zero, one can determine the phase constant of the plane wave, and then the effective permittivity and permeability of the artificial medium.

I. INTRODUCTION

An artificial medium consists of a large number of scattering elements placed in some homogeneous background or host medium [1]. Typically there will be a large number of identical electrically small scatterers per cubic wavelength. When an electromagnetic wave propagates through the artificial medium, it will induce currents on or in the scatterers. Thus, the scatterers can be viewed as macroscopic electric and/or magnetic dipole moments, in analogy to the microscopic molecular electric and/or magnetic dipole moments in a real dielectric and/or ferrite medium [2]. These macroscopic dipole moments modify the net electric and/or magnetic dipole moment per unit volume, and thus they also modify the effective permittivity and permeability of the medium.

An interesting and potentially useful feature of artificial media is that by adjusting the size, shape, material composition, and density of the scatterers, one may be able to engineer or design a medium which has desirable permeability, permittivity, and dispersion characteristics. Also, the theory presented here may be useful in modeling composite materials formed by placing lossy dipole filaments or periodic weaves of long lossy filaments in a host medium. The use of artificial dielectrics was first suggested by Kock for making microwave lenses [3]. Brown [4] showed that a two-dimensional periodic array of conducting wires is an artificial dielectric with index of refraction less than unity, and Bahl and Gupta [5] used this idea in the design of a leaky wave antenna. King, Thiel, and Park inserted small pins in a grounded dielectric substrate to synthesize an artificial dielectric with a given surface reactance [6]. Artificial media have also been used in the design of microwave lenses [7]–[9], by Rotman to model plasmas [10], and by Sihvola to model rain and

hail [11]. Hall *et al.* have considered the use of artificial dielectrics in the reduction of the radar cross section of vehicles [12].

Most of the early methods of analysis for artificial media were based upon static approximations, and often included only the lower order multipoles [1, Ch. 12]. For this reason, they were limited to electrically small scatterers, which were not placed too close to one another. More recently, quasistatic solutions have been presented by Poularikas [13] and Sihvola [11]. By contrast, the present method is a full wave analysis based upon a method of moments (MM) [14] solution of an exact integral equation for the equivalent currents representing the scatterers. This MM solution accounts for mutual coupling between the scatterers, is applicable to artificial media comprised of scatterers of essentially arbitrary size, shape, and material composition, and is capable of determining the dispersion characteristics of the artificial medium. As opposed to many other methods [1, Ch. 12], it is not necessary to know the electric and magnetic polarizability of the scatterers, since this is implicitly determined as part of the MM solution. In this and most other analyses of artificial media, the scatterers are assumed to be identical, and to be arranged in a periodic lattice. This simplification allows the artificial media to be analyzed by the periodic moment method (PMM) [15], in which the unknowns in the MM solution are limited to currents on the center element.

Section II presents the general integral equation and PMM analysis of periodic artificial media, and includes a discussion of the computation of the effective permittivity and permeability for anisotropic artificial media. Numerical results for artificial media comprised of a 3-D array of short dipoles are presented in Section III, and are compared with static solutions.

II. PMM ANALYSIS OF ARTIFICIAL MEDIA

A. Overview of the Problem

As illustrated in Fig. 1, the artificial medium is modeled as a triple infinite periodic array of identical scattering elements in some homogeneous and isotropic background or host medium with permittivity and permeability denoted (μ_0, ϵ_0) , wavelength λ_0 , and wavenumber $k_0 = \omega/\sqrt{\mu_0\epsilon_0}$. Although here no assumption is made as to size and density of scatterers, typically there will be a large number of electrically small scatterers per cubic wavelength. The spacing between the elements is denoted by d_1, d_2 , and d_3 in the x, y , and z directions, respectively. The elements in the triple infinite array of scatterers will be identified by the integer indices $Q = (l, m, n)$, $(-\infty \leq (l, m, n) \leq \infty)$. Element $Q = (0, 0, 0)$ will be referred to as the center element, and is assumed to be located in the vicinity of the origin. $\Delta Q = (ld_1\hat{x}, md_2\hat{y}, nd_3\hat{z})$ is a vector from a reference point on the center element to the corresponding point on element Q . In this paper, all fields and currents are assumed to be time harmonic, with the $e^{j\omega t}$ time dependence suppressed.

The basic problem is to determine whether or not the periodic medium of Fig. 1 appears as an artificial medium, and if so, to compute the effective complex permittivity and permeability of the

Manuscript received February 26, 1992; revised September 20, 1993. This work was supported by the Joint Services Electronics Program under Contract N00014-78-C-0049 with the Ohio State University Research Foundation.

The authors are with the ElectroScience Laboratory, Ohio State University, Columbus, OH 43212 USA.

IEEE Log Number 9401355.

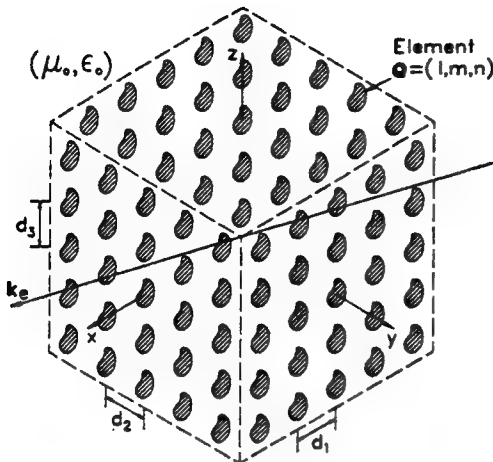


Fig. 1. A triple infinite periodic array of scatterers representing an artificial dielectric.

artificial medium. This will be done by determining whether or not a plane wave is an eigenfunction [16, Ch. 4-1] of the periodic medium of Fig. 1, and if so, what is the eigenvalue or complex phase constant of that plane wave. By an eigenfunction it is meant a source-free solution of Maxwell's equations that satisfies all of the boundary conditions. To find the eigenfunctions, a plane wave of a known frequency ω is assumed to be propagating through the periodic medium in a known direction. In a source-free homogeneous medium (isotropic or anisotropic [17, Ch. 2.3]), a plane wave propagating in the \hat{u} direction will have spatial variation of the form

$$e^{-jk_e \cdot r}, \quad (1)$$

where $k_e = k_e \hat{u}$ is the *unknown* vector phase constant of the plane wave in an artificial medium of wavenumber k_e , and $r = r\hat{r} = x\hat{x} + y\hat{y} + z\hat{z}$ is a vector from the origin to the point (x, y, z) . It is emphasized that at this point in the solution the direction of propagation \hat{u} for the plane wave is known; however, its phase constant k_e and polarization are unknown. Analogous to the methods used by Itoh and Mittra to determine the effective permittivity of a microstrip transmission line [18], if a value of k_e can be found such that this plane wave is an eigenfunction of the periodic medium, then the periodic medium can be viewed as an artificial medium with effective dyadic permeability and permittivity denoted $(\bar{\mu}_e, \bar{\epsilon}_e)$. The evaluation of $(\bar{\mu}_e, \bar{\epsilon}_e)$ is discussed in Section II-C.

B. Integral Equation and Moment Method Solution

The periodic medium of Fig. 1 can be analyzed using the periodic moment method (PMM), which has been extensively applied in the analysis of periodic arrays or frequency selective surfaces [15]. The solution is begun by using the equivalence theorems [2], [16] to replace the periodic array of scatterers by the host medium and by equivalent currents. For example, the volume equivalence theorem [2, Ch. 7.7] can be used to replace dielectric scatterers by electric volume polarization currents located in the volume occupied by the scatterers. For perfectly conducting scatterers, the surface equivalence theorem [2, Ch. 7.8] can be used to replace the scatterers by equivalent electric surface currents on the surface of the scatterers. For the sake of simplicity, here it will be assumed that the equivalent current is electric (as opposed to magnetic), and thus the equivalent electric

current on the elements of the periodic array can be written as

$$\mathbf{J} = \sum_{l,m,n} \mathbf{J}^Q, \quad (2)$$

where \mathbf{J}^Q is the equivalent electric current on element Q , and the summation is over all array elements ($-\infty \leq (l, m, n) \leq \infty$). \mathbf{J}^Q exists over the region R^Q (surface or volume) of element Q . Using the periodicity of the medium and of the plane wave field of (1), the current on each element is identical except for an amplitude and phase shift corresponding to the amplitude and phase of the plane wave at the reference point on each element. Using (1), the complex magnitude of the current on element Q , relative to that of the center element, is

$$C^Q = e^{-jk_e \cdot \Delta Q}. \quad (3)$$

The next step is to formulate an integral equation for the equivalent eigenfunction current \mathbf{J} . Although there are many possible integral equations (surface, volume, electric field, magnetic field, etc.), they can always be written in the form

$$L(\mathbf{J}) = 0 \text{ over } R^0 \quad (4)$$

where L is a linear operator and R^0 is the region over which the center element current \mathbf{J}^0 is defined. Inserting (2) into (4) and using the linearity of L yields

$$\sum_{l,m,n} L(\mathbf{J}^Q) = 0 \text{ over } R^0. \quad (5)$$

In order to solve (5) using the PMM, the current on the entire array is expanded as

$$\mathbf{J} = \sum_{l,m,n} \mathbf{J}^Q = \sum_{l,m,n} C^Q \sum_{j=1}^N I_j \mathbf{J}_j^Q \quad (6)$$

where the \mathbf{J}_j^Q are a sequence of N known expansion functions on element Q , and the I_j are a sequence of N unknown coefficients ($j = 1, 2, \dots, N$). The expansion functions \mathbf{J}_j^Q on element Q are identical to those on the center element, except for a translation of ΔQ .

Inserting (6) into (5), and using the linearity of L , yields

$$\sum_{l,m,n} C^Q \sum_{j=1}^N I_j L(\mathbf{J}_j^Q) = 0 \quad \text{over } R^0. \quad (7)$$

The final step in the PMM solution requires the selection of N linearly independent vector weighting functions over R^0 , denoted \mathbf{w}_i , $i = 1, 2, \dots, N$. Taking the inner product of (7) with each weighting function will reduce (7) to a system of N simultaneous linear equations in the N unknowns I_j ($j = 1, 2, \dots, N$), which can be compactly written as the matrix equation

$$[Z(k_e)]I = 0 \quad (8)$$

where $[Z(k_e)]$ is the order N impedance matrix, and I is the length N current vector containing the N coefficients in the expansion for the current. A typical element of the impedance matrix is

$$\begin{aligned} Z_{ij}(k_e) &= \sum_{l,m,n} C^Q Z_{ij}^Q \\ &= \sum_{l,m,n} C^Q \langle L(\mathbf{J}_j^Q), \mathbf{w}_i \rangle \quad i, j = 1, 2, \dots, N, \end{aligned} \quad (9)$$

where Z_{ij}^Q is the mutual impedance between expansion function j on element Q and weighting function i on the center element, and the

brackets indicate an appropriate inner product. Typically, this inner product will be chosen as

$$Z_{ij}^Q(k_e) = \int_{R^0} L(\mathbf{J}_j^Q) \cdot \mathbf{w}_i d\tau \quad (10)$$

where the integration is over the region (line, surface, volume) of the center element for which \mathbf{w}_i is nonzero. Note that the elements of the impedance matrix depend upon the *unknown* phase constant k_e , which enters through the C^Q of (3). The impedance sums in (9) are typically not absolutely convergent, and some technique to accelerate convergence is usually required for numerical computations [19].

The homogeneous matrix equation (8) will only have a nontrivial solution if

$$|Z(k_e)| = 0, \quad (11)$$

that is, if the determinant of the impedance matrix is zero. Equation (11) must be solved, usually in an iterative fashion, for the eigenvalues k_e , which result in a zero determinant. If a root of this characteristic equation exists, then the periodic medium can be viewed as an artificial medium, with effective permeability and permittivity, as described in the next section.

To find the eigenfunction currents, to within a constant, an arbitrary (nonzero) element of the \mathbf{J} vector is set to unity, and (8) is reduced to an order $N - 1$ matrix equation for the remaining $N - 1$ elements in \mathbf{J} . For example, setting $J_{N,N} = 1$, (8) becomes

$$[Z'(k_e)]\mathbf{J}' = \begin{bmatrix} -Z_{1,N} \\ -Z_{2,N} \\ \vdots \\ -Z_{N-1,N} \end{bmatrix} \quad (12)$$

where the $[Z']$ matrix holds the first $N - 1$ rows and columns of the $[Z]$ matrix, and the \mathbf{J}' vector holds the first $N - 1$ elements of the \mathbf{J} vector.

The eigenfunction field is produced by the superposition of the fields of the currents \mathbf{J}^Q ($-\infty \leq (l, m, n) \leq \infty$) radiating in the homogeneous host medium (μ_0, ϵ_0). This field will appear as a plane wave, with the spatial variation of (1), plus some fine structure or ripple as the field point approaches one of the scatterers.

C. Determination of the Effective Permeability and Permittivity

Discussion of the roots k_e and polarization: The first step in determining the equivalent permeability and permittivity of the artificial medium is to determine the roots k_e from (11). For a given direction of propagation through an anisotropic artificial medium composed of arbitrary scatterers, there are two fundamental roots k_e to (11) [20, Sec. 4.25], [21, Sec. 14.2.2]. Each root corresponds to a distinct polarization of the plane wave in the artificial medium, and its corresponding eigenfunction currents and fields.

For special geometries, the roots may be repeated roots or degenerate to the host medium wavenumber $k_e = k_0$. For example, repeated roots (two roots with the same numerical value for k_e) will occur for propagation normal to a symmetric wire cross with equal-length vertical and horizontal members. One root corresponds to vertical polarization, and the other root corresponds to horizontal polarization. If the scatterer is of 2-D or of 3-D extent, the two roots will be different from the host medium wavenumber. If the scatterer is of 1-D extent (i.e., a linear dipole), then there will be one root $k_e = k_0$, corresponding to a plane wave with polarization perpendicular to the dipole, and one root $k_e \neq k_0$, corresponding to polarization parallel to the dipole.

Note that in developing (11), the polarization of the plane wave was not specified. Thus, when a root of (11) is found, the polarization is unknown. To find the polarization one can first compute the

corresponding eigenfunction currents using (12), and then the eigenfunction electric and magnetic fields. The polarization of the electric field is taken as the polarization corresponding to the chosen value of k_e . Once the eigenfunction fields are known, the characteristic impedance of the artificial medium, denoted η_e , can be evaluated as the ratio of the electric to magnetic eigenfunction fields tangential to the assumed direction of propagation. If the host medium and the scatterers are lossless, then k_e and η_e will be positive real numbers. However, if either the host medium or the scatterers have loss, then k_e will be a complex number in the fourth quadrant, and η_e will be a complex number in the sector $\pm 45^\circ$ of the positive real axis [16, Sec. 2-3].

Since the scatterers in an artificial medium are typically electrically very small, one is usually interested in the lowest order eigenfunction modes with the smallest k_e . However, it is important to note that larger roots, corresponding to higher order modes, may exist. In general, we know of no *a priori* method for distinguishing the roots corresponding to the lowest order modes from those corresponding to the higher order modes. Normally, this should not be a problem, since for the electrically small scatterers commonly used in artificial media, the higher order modes are so far from resonance.

Anisotropic artificial media: Consider the determination of the dyadic effective permeability and permittivity ($\bar{\mu}_e, \bar{\epsilon}_e$) for an anisotropic artificial medium. It is mentioned that artificial media can be chiral or even bianisotropic [17]; however, (3) would no longer be valid, and this is beyond the scope of this article. It is assumed that for a given geometry, the two roots k_e , their corresponding eigenfunction currents \mathbf{J}^0 on the center element, and their eigenfunction fields ($\mathbf{E}^0, \mathbf{H}^0$), averaged over the volume of the center cell, have all been determined. In the limit as $k_e \rightarrow k_0$, the eigenfunction currents vanish and the eigenfunction fields become identical to a plane wave in free space. Note that in anisotropic media ($\mathbf{E}^0, \mathbf{H}^0$) are not in general orthogonal to k_e [17, Ch. 2.3].

The electric and magnetic dipole moment per unit volume in the center cell can now be computed as [1, Ch. 12.5]

$$\mathbf{P}^0 = \frac{1}{j\omega\Delta v} \int_{R^0} \mathbf{J}^0 d\tau = \epsilon_0 \bar{\chi}^e \cdot \mathbf{E}^0, \quad (13)$$

$$\mathbf{M}^0 = \frac{1}{2\Delta v} \int_{R^0} \mathbf{r} \times \mathbf{J}^0 d\tau = \bar{\chi}^m \cdot \mathbf{H}^0 \quad (14)$$

where R^0 is the region of the center cell of volume $\Delta v = d_1 d_2 d_3$, and $\bar{\chi}^e$ and $\bar{\chi}^m$ are the dimensionless symmetric [20, Sec. 4.24], [21, Sec. 14.1] dyadic effective electric and magnetic susceptibilities, respectively, for the artificial medium. Equation (14) shows that even perfectly conducting or pure dielectric scatterers can have a magnetic moment, and thus an effective permeability different from the host medium. Assuming that the usual constitutive relationships, which are valid point by point in a real medium, hold in an average sense in an artificial medium, the average electric and magnetic flux densities in the center cell are given by

$$\mathbf{D}^0 = \epsilon_0 \mathbf{E}^0 + \mathbf{P}^0 = \epsilon_0 \mathbf{E}^0 + \epsilon_0 \bar{\chi}^e \cdot \mathbf{E}^0 = \bar{\epsilon}_e \cdot \mathbf{E}^0 \quad (15)$$

$$\mathbf{B}^0 = \mu_0 (\mathbf{H}^0 + \mathbf{M}^0) = \mu_0 (\mathbf{H}^0 + \bar{\chi}^m \cdot \mathbf{H}^0) = \bar{\mu}_e \cdot \mathbf{H}^0. \quad (16)$$

From (15) and (16), the dyadic effective permittivity and permeability are given by

$$\bar{\epsilon}_e = (\bar{\mathbf{I}} + \bar{\chi}^e) \epsilon_0 \quad (17)$$

$$\bar{\mu}_e = (\bar{\mathbf{I}} + \bar{\chi}^m) \mu_0 \quad (18)$$

where $\bar{\mathbf{I}}$ is the unit dyad.

Explicitly showing the dyadic equation (13) relating the effective electric susceptibility to the average electric field and the electric

dipole moment per unit volume in the center cell,

$$\epsilon_0 \begin{bmatrix} \chi_{xx}^e & \chi_{xy}^e & \chi_{xz}^e \\ \chi_{yx}^e & \chi_{yy}^e & \chi_{yz}^e \\ \chi_{zx}^e & \chi_{zy}^e & \chi_{zz}^e \end{bmatrix} \begin{bmatrix} E_x^0 \\ E_y^0 \\ E_z^0 \end{bmatrix} = \begin{bmatrix} P_x^0 \\ P_y^0 \\ P_z^0 \end{bmatrix}. \quad (19)$$

Equation 19 is equivalent to three equations in the nine components of $\bar{\chi}^e$, and is the result of one of the two roots of (11). The other root will produce a dyadic equation, similar to (19) with the same $\bar{\chi}^e$, but with different E^0 and P^0 . The two dyadic equations, along with the condition that $\bar{\chi}^e$ is symmetric, can now be solved for the nine components of $\bar{\chi}^e$. The determination of $\bar{\mu}_e$ is parallel to that presented for $\bar{\epsilon}_e$. In a real anisotropic medium the elements of the dyadic constitutive parameters are independent of the direction of propagation [20, Ch. 4], [21, Sec. 14.1]; however, this may not hold in an artificial medium.

Uniaxial artificial media: For certain simple anisotropic media, termed uniaxial media, the off diagonal components of $\bar{\chi}^e$ (and $\bar{\chi}^m$) are negligible, and the diagonal components are related to E^0 and P^0 by

$$\chi_{ii}^e = \frac{P_i^0}{\epsilon_0 E_i^0} \quad i = x, y, z. \quad (20)$$

Equation 20 can be used to find the ii component of $\bar{\chi}^e$ provided E_i^0 is nonzero. If for a given direction of propagation and root, $E_i^0 \neq 0$ for $i = x, y, z$, then (20) can be used to find all three diagonal components of $\bar{\chi}^e$. If for a given direction of propagation and root $E_i^0 = 0$, then $P_i^0 = 0$, and (20) is indeterminate. In this case χ_{ii}^e can be determined from the other root, or by a different direction of propagation.

Consider propagation along of one of the three principle axes in a uniaxial media. The two roots will correspond to polarizations in the directions of the two axes transverse to the direction of propagation. For this special case, the effective permittivity and permeability can be determined from the root k_e and the characteristic impedance η_e . It is assumed that k_e and η_e have been determined for a given frequency, polarization, and direction of propagation along one of the principle axes. Since k_e and η_e are related to μ_e and ϵ_e by

$$k_e = \omega \sqrt{\mu_e \epsilon_e} \quad \text{and} \quad \eta_e = \sqrt{\frac{\mu_e}{\epsilon_e}}, \quad (21)$$

then

$$\epsilon_e = \frac{k_e}{\omega \eta_e} \quad \text{and} \quad \mu_e = \frac{\eta_e k_e}{\omega}. \quad (22)$$

If $\mu_e = \mu_0$, then ϵ_e is given by

$$\epsilon_e = \frac{k_e^2}{\omega^2 \mu_0} \quad (23)$$

thus eliminating the need to compute η_e .

III. NUMERICAL RESULTS

This section will present numerical results for artificial media comprised of a 3-D array of short perfectly conducting z directed dipoles of length L and radius a . The MM solution for the 3-D dipole array is based upon the usual thin-wire formulation, employing piecewise sinusoidal (PWS) expansion and weighting functions [22]. In all cases the background medium is free space and the polarization of the electric field is \hat{z} . For this case, the artificial media are lossless artificial dielectrics ($\mu_e = \mu_0$) with real ϵ_e related to k_e by (23). The

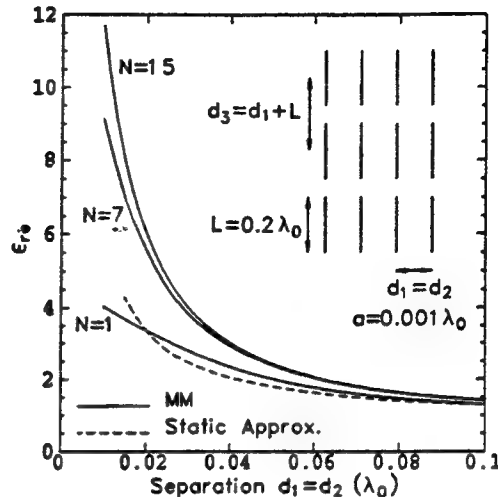


Fig. 2. Relative effective permittivity versus lattice size for a 3-D array of dipoles.

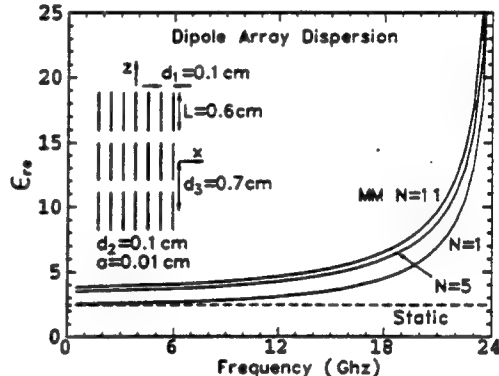


Fig. 3. Dispersion of the effective permittivity for a 3-D array of dipoles (propagation along the z axis).

artificial media are uniaxial, with ϵ_e being the zz component of $\bar{\epsilon}_e$. To the approximations used, the xx and yy components are equal to ϵ_0 , and all off diagonal components are zero.

The insert in Fig. 2 shows a 3-D array of short dipoles of radius $a = 0.001\lambda_0$ and length $L = 0.2\lambda_0$ in a lattice with spacing $d_1 = d_2$ and $d_3 = d_1 + L$. The figure shows the relative effective permittivity of the medium as a function of lattice size d_1 . Curves are shown for $N = 1, 7$, and 15 PWS basis functions, and are compared to the static approximation of Collin [1]. As expected, the effective permittivity increases as the density of the dipoles increases. Note that for relatively large lattice spacing the current on the short dipoles is nearly triangular, and is well approximated by $N = 1$ sinusoidal basis function solutions. However, as $d_1/\lambda_0 \rightarrow 0$, the dipoles are almost touching. This causes the dipole current to take on a more "flat top" shape, and requires more than $N = 1$ basis functions to obtain a converged result.

The final set of data will illustrate dispersion in artificial dielectrics. The insert in Fig. 3 shows an artificial dielectric comprised of dipoles of length $L = 0.6$ cm, radius $a = 0.01$ cm, and with a lattice spacing $d_1 = d_2 = 0.1$ cm and $d_3 = 0.7$ cm. For a wave propagating along the z axis, the $N = 1, 5$, and 11 term MM solutions for the relative effective permittivity of the dipole array is plotted from 0.24 GHz to 24 GHz, corresponding to dipole lengths from $0.0048\lambda_0$ to $0.48\lambda_0$. At low frequencies, the MM solution approaches the static result

(dashed line) of $\epsilon_{re} \approx 2.5$. However, as the frequency increases, the magnitude of the scattered field from each dipole increases, thus causing the effective permittivity to significantly increase.

REFERENCES

- [1] R. E. Collin, *Field Theory of Guided Waves*. New York: IEEE Press, 1991.
- [2] C. A. Balanis, *Advanced Engineering Electromagnetics*. New York: Wiley, 1989.
- [3] W. E. Kock, "Metal-lens antenna design," *IRE Proc.*, vol. 34, pp. 828-836, Nov. 1946.
- [4] J. Brown, "Artificial dielectrics having refractive indices less than unity," *IEE Proc.*, vol. 100, pt. 4, pp. 51-62, 1953.
- [5] I. J. Bahl and K. C. Gupta, "A leaky-wave antenna using an artificial dielectric medium," *IEEE Trans. Antennas Propagat.*, vol. AP-22, no. 1, pp. 119-122, Jan. 1974.
- [6] R. J. King, D. V. Thiel, and K. S. Park, "The synthesis of surface reactance using an artificial dielectric," *IEEE Trans. Antennas Propagat.*, vol. 31, no. 3, pp. 471-476, May 1983.
- [7] J. P. A. Martindale, "Lens aerials at centimeter wavelength," *J. Brit. IRE*, vol. 13, pp. 243-259, May 1953.
- [8] O. M. Stuetzer, "Development of artificial optics in Germany," *IRE Proc.*, vol. 38, pp. 1053-1056, Sept. 1950.
- [9] A. F. Harvey, "Optical techniques at microwave frequencies," *IEE Proc.*, vol. 106, pt. B, pp. 141-157, Mar. 1959.
- [10] W. Rotman, "Plasma simulation by artificial dielectrics and parallel-plate media," *IRE Trans. Antennas Propagat.*, vol. AP-10, no. 1, pp. 82-95, Jan. 1962.
- [11] A. Sihvola, "Macroscopic permittivity of dielectric mixtures with application to microwave attenuation of rain and hail," *IEE Proc.*, vol. 136, pt. H(1), pp. 24-28, Feb. 1989.
- [12] R. C. Hall, R. Mittra, and J. R. Mosig, "Analysis of a parallel resistive plate medium," *IEEE Trans. Antennas Propagat.*, vol. 38, no. 3, pp. 299-304, Mar. 1990.
- [13] A. D. Poularikas, "Effective index of refraction of isotropic media containing layered spheres," *J. Appl. Phys.*, vol. 58, pp. 1044-1046, 1985.
- [14] R. F. Harrington, *Field Computations by Moment Methods*. New York: Macmillan, 1968.
- [15] R. Mittra, C. H. Chan, and T. Cwik, "Techniques for analyzing frequency selective surfaces—a review," *Proc. IEEE*, vol. 76, no. 12, pp. 1593-1615, Dec. 1988.
- [16] R. F. Harrington, *Time-Harmonic Electromagnetic Fields*. New York: McGraw-Hill, 1961.
- [17] J. A. Kong, *Electromagnetic Wave Theory*. New York: Wiley, 1986.
- [18] T. Itoh and R. Mittra, "Spectral-domain approach for calculating the dispersion characteristics of microstrip lines," *IEEE Trans. Microwave Theory Tech.*, vol. MTT-21, pp. 496-499, July 1973.
- [19] S. Singh and R. Singh, "Application of transforms to accelerate the summation of periodic free-space Green's functions," *IEEE Trans. Microwave Theory Tech.*, vol. 38, no. 11, pp. 1746-1748, Nov. 1990.
- [20] A. Sommerfeld, *Optics, Lectures on Theoretical Physics*, vol. IV. New York: Academic, 1954.
- [21] M. Born and E. Wolf, *Principles of Optics*. New York: Pergamon, 1980.
- [22] J. L. Blanchard, "Integral equation analysis of artificial dielectrics," Ph.D. dissertation, Dept. of Mathematics, Ohio State Univ., Columbus, 1991.

A Partitioning Technique for the Finite Element Solution of Electromagnetic Scattering from Electrically Large Dielectric Cylinders

Robert Lee and Veera Chupongstumun

Abstract—A finite element partitioning scheme has been developed to reduce the computational costs of modeling electrically large geometries. In the partitioning scheme, the cylinder is divided into many sections. The finite element method is applied to each section independent of the other sections, and then the solutions in each section are coupled through the use of the tangential field continuity conditions between adjacent sections. Since the coupling matrix is significantly smaller than the original finite element matrix, it is expected that both the CPU time and memory costs can be significantly reduced. The partitioning scheme is coupled to the bymoment method to account for the boundary truncation. Numerical results are presented to demonstrate the efficiency and accuracy of the method.

I. INTRODUCTION

The finite element method (FEM) is being used extensively to perform electromagnetic modeling, because it is efficient in modeling geometries that are both penetrable and inhomogeneous. The efficiency is largely due to the fact that the resulting matrix is sparse. Banded matrix solvers [1] have traditionally been used to solve the FEM stiffness matrix. However, when the electrical size of the geometry of interest is large, the number of unknowns required to obtain an accurate solution may be so large that the use of banded solvers becomes computationally infeasible. The development of direct sparse matrix solvers such as the nested dissection method [2] has been a major area of research. These methods are capable of handling multiple excitations with only a small increase in computation costs. The computational complexity of sparse matrix methods is usually less than that of banded matrix methods. For example, the computation cost of the nested dissection method is proportional to $N^{1.5}$, while the computation cost for the banded matrix methods is proportional to N^2 for two-dimensional geometries. The direct sparse matrix methods rely heavily upon the use of matrix partitioning or reordering schemes to reduce the number of nonzero entries in the factorization of the resulting matrixes.

In numerical electromagnetics, several researchers have developed methods that have characteristics very similar to those used in direct sparse matrix methods. However, rather than formulating it from a mathematical viewpoint of reorganizing the matrix, the researchers considered it from a physical viewpoint where the geometry is divided into subsections. Within each section, a numerical solution is generated independent of the other sections. The coupling between the sections is then performed in either an iterative manner [3], [4] or by employing rigorous and more computationally expensive procedures [5], [6]. It should be noted that all these techniques have been developed for integral equation methods. In this paper, a partitioning technique is presented for the FEM to solve the problem of electromagnetic scattering from a two-dimensional cylinder. Like the integral equation methods, the geometry is divided into subsections in which a set of finite element solutions is generated for each section independent of the other sections. The sections are then coupled together to form a sparse matrix that is significantly smaller than

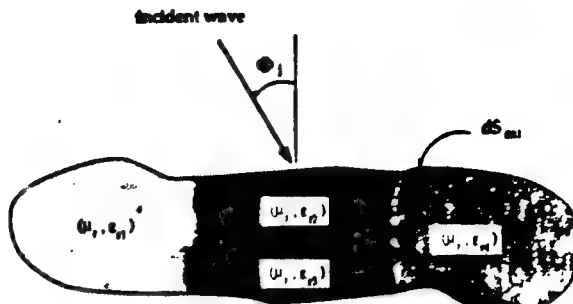


Fig. 1. Cross section of a representative dielectric cylinder.

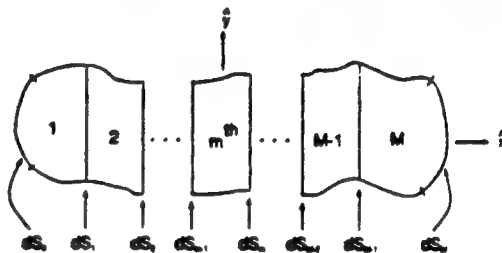


Fig. 2. A representative partitioning of the dielectric cylinder.

the original FEM stiffness matrix. This partitioning technique can be coupled to a boundary truncation method such as the bymoment method [7] to solve the scattering problem. During this research, it was discovered that another group was employing a very similar method for waveguiding geometries [8]. It is expected that both methods will produce the same efficiency.

II. FORMULATION

Let us consider an infinitely long isotropic dielectric cylinder whose shape and material properties are invariant along the z axis, as shown in Fig. 1. The incident wave is also assumed to be invariant in z ; therefore the fields around the cylinder can be decoupled into $TM(E_x, H_z, H_y)$ and $TE(H_x, E_z, E_y)$ polarizations. In this paper, the TM polarization is described. With some slight modifications, the formulation for the TE polarization can also be obtained. To simplify the notation, let us define E to be E_z . E satisfies the generalized Helmholtz equation, which is given by

$$\nabla \cdot \left(\frac{1}{\mu} \nabla E \right) + \omega^2 \epsilon^* E = 0 \quad (1)$$

where $\epsilon^* = \epsilon - j(\sigma/\omega)$. It is assumed that the $\exp(j\omega t)$ time dependence has been suppressed.

Initially, the formulation is presented to solve a boundary value problem in which the Neumann boundary condition is specified on dS_{ext} in Fig. 1. Then the procedure for coupling the partitioning method to the bymoment method is described to solve the scattering problem. In the partitioning method, the cylinder is divided into M sections as shown in Fig. 2, where $dS_0, \dots, dS_m, \dots, dS_{M-1}$ denote the interior boundaries that are created from the partitioning operation. The segments dS_0 and dS_M are artificial constructs that allow us to represent the first and last sections as four-sided sections.

A. FEM Solution in a Single Section

Let us consider the m th section of the partitioned cylinder as shown in Fig. 3. The solution in this section can be obtained from FEM if

Manuscript received November 12, 1993. This work was supported by the Joint Services Electronics Program under Contract N00014-89-J-1007.

The authors are with the ElectroScience Laboratory, Department of Electrical Engineering, Ohio State University, Columbus, OH 43212 USA.

IEEE Log Number 9401347.

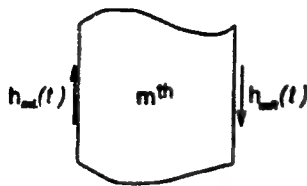


Fig. 3. The m th section of the cylinder. The direction of the tangential magnetic fields, h_{mL} and h_{mR} , are defined as shown.

the correct boundary conditions are specified. However, although the Neumann boundary condition on dS_{ext} is assumed to be known, the boundary conditions on dS_{m-1} and dS_m are not known *a priori*. Let us define h_{mL} and h_{mR} to be the tangential magnetic field on dS_{m-1} and dS_m , respectively, for the m th element. These two quantities can also be written in terms of a derivative of the electric field E where their orientation is shown in Fig. 3. The tangential magnetic fields can be written in terms of an infinite sum of linearly independent functions (Ψ_i , $i = 1, 2, 3, \dots$) multiplied by unknown coefficients $a_i^{(m)}$ and $b_i^{(m)}$.

$$h_{mL}(t) = \frac{1}{j\omega\mu} \frac{\partial E(t)}{\partial n} = \sum_{i=1}^{\infty} a_i^{(m)} \Psi_i(t) \quad t \in [0, d_L] \quad (2)$$

$$h_{mR}(t) = \frac{1}{j\omega\mu} \frac{\partial E(t)}{\partial n} = \sum_{i=1}^{\infty} b_i^{(m)} \Psi_i(t) \quad t \in [0, d_R] \quad (3)$$

where $\partial/\partial n$ represents a directional derivative whose direction is outward normal from a point on the surface of the m th section. The variable t represents a parametric mapping of the (x, y) coordinates along dS_{m-1} to the line defined by the endpoints $t = 0$ and $t = d_L$, where d_L is the length of dS_{m-1} . A similar parametric mapping is made for dS_m , where d_R is the length of dS_m .

In the numerical implementation of (2) and (3) the infinite sums are truncated to I_{mL} and I_{mR} for dS_{m-1} and dS_m , respectively. Using the properties of linearity, we can determine the electric field E_m in the m th section by superimposing the three boundary value problems shown in Fig. 4, where E_m^L , E_m^R , and E_m^L represent the electric field solution for the corresponding boundary value problems in the figure. Note that the boundary conditions for E_m^R and E_m^L are given by (2) and (3); therefore, these field solutions are given by

$$E_m^L(x, y) = \sum_{i=1}^{I_{mL}} a_i^{(m)} \Lambda_{i,m}^L(x, y) \quad (4)$$

$$E_m^R(x, y) = \sum_{i=1}^{I_{mR}} b_i^{(m)} \Lambda_{i,m}^R(x, y) \quad (5)$$

where $\Lambda_{i,m}^L$ is the finite element solution for the boundary value problem in Fig. 4 associated with E_m^L except that $\Psi_i(t)$ replaces $h_{mL}(t)$ as the boundary condition. Similarly, $\Lambda_{i,m}^R$ is generated from the replacement of $h_{mR}(t)$ by $\Psi_i(t)$ in the boundary value problem associated with E_m^R . The total field in the m th section can thus be written as

$$E_m(x, y) = E_m^F + \sum_{i=1}^{I_{mL}} a_i^{(m)} \Lambda_{i,m}^L + \sum_{i=1}^{I_{mR}} b_i^{(m)} \Lambda_{i,m}^R. \quad (6)$$

Equation (6) is true for all sections except the first and last ones. For the first section, the Neumann boundary condition on dS_0 is known. Thus, the second term in (6) can be directly incorporated into E_m^F . Similarly, for the last section, the third term in (6) can be incorporated into E_m^F .

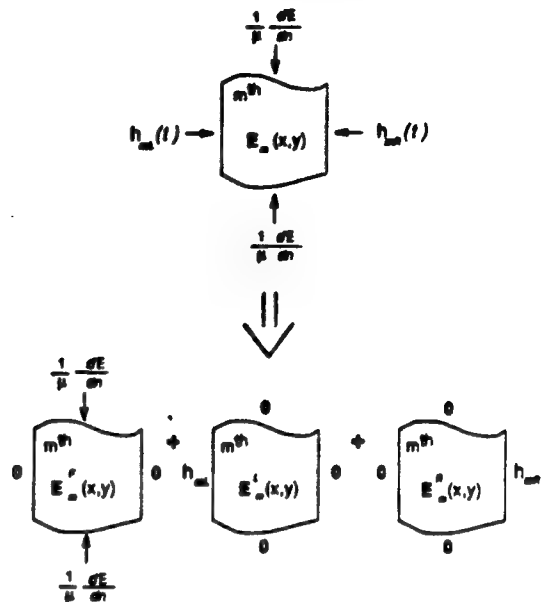


Fig. 4. The boundary value problem in the m th section is broken down into the three boundary value problems shown.

B. Coupling the Solution Between Sections

Once the solutions have been generated for every section as described above, it is necessary to couple them together in order to determine the coefficients $a_i^{(m)}$ and $b_i^{(m)}$. The coupling is accomplished by enforcing the continuity of the tangential magnetic and electric fields at the interface between adjacent sections. From (2) and (3), the continuity of the tangential magnetic field is specified by

$$\sum_{i=1}^{I_{mR}} b_i^{(m)} \Psi_i(t) = - \sum_{i=1}^{I_{(m+1)L}} a_i^{(m+1)} \Psi_i(t) \quad m = 1, 2, \dots, M-1. \quad (7)$$

The negative sign on the right hand side of (7) is due to the orientation of the tangential magnetic field quantities in Fig. 3. Due to this continuity condition, it is appropriate to assume that $I_{mR} = I_{(m+1)L} \equiv I_m$. The sum in (7) can be equated term by term to obtain

$$a_i^{(m+1)} = -b_i^{(m)} \quad m = 1, 2, \dots, M-1. \quad (8)$$

The use of (8) in (6) eliminates half of the unknowns. We determine the remaining unknowns by enforcing the continuity of the tangential electric field on dS_m .

$$E_m(x, y) = E_{m+1}(x, y) \quad (x, y) \in dS_m. \quad (9)$$

In general, it is not possible to choose the coefficients $a_i^{(m)}$ and $b_i^{(m)}$ to satisfy (9) exactly. Instead, (9) is enforced in a weak sense, i.e.,

$$\int_{dS_m} E_m(x, y) w_{j,m} dl = \int_{dS_m} E_{m+1}(x, y) w_{j,m} dl \quad (10)$$

where $w_{j,m}$ ($j = 1, 2, \dots, I_m$) represents a set of linearly independent weighting functions on dS_m . Substituting (8) into (6) and then

Fig. 5. The block tri-diagonal coupling matrix.

(6) into (10), we obtain

$$\begin{aligned}
 & \int_{dS_m} \left[\sum_{i=1}^{J_{m-1}} b_i^{(m-1)} \Lambda_{i,m}^L - \sum_{i=1}^{J_m} b_i^{(m)} (\Lambda_{i,m}^R + \Lambda_{i,(m+1)}^L) \right. \\
 & \quad \left. + \sum_{i=1}^{J_{m+1}} b_i^{(m+1)} \Lambda_{i,(m+1)}^R \right] u_{j,m} \, dl \\
 & = \int_{dS_m} (E_m^F - E_{m+1}^F) u_{j,m} \, dl. \tag{11}
 \end{aligned}$$

This equation is valid for $m = 1$ to $m = M - 1$, where it is assumed that $b_i^{(0)} = 0$ and $b_i^{(M)} = 0$. The matrix that results from (11) can be ordered in such a way that it forms a block tridiagonal matrix as shown in Fig. 5, where the submatrices A_m , B_m , and C_m are full and have dimensions of $J_m \times J_{m-1}$, $J_m \times J_m$, and $J_m \times J_{m+1}$, respectively. The vectors F_m , each of which has a length J_m , represents the right hand side of (11). The solution of this matrix equation can be efficiently computed with a banded matrix solver or a matrix solver specially designed for matrices of this type, such as the Riccati transform [9].

C. Boundary Truncation

To solve the scattering problem, the interior FEM problem must be coupled to the exterior free space region. In this paper, the bymoment method [7] is used to perform the coupling. The bymoment method relies upon the superposition of a multiple number of finite element solutions, which are generated with specified Dirichlet boundary conditions. The number of FEM solutions is equal to the number of expansion functions used to approximate the boundary solution. The bymoment method can be modified such that the multiple finite element solutions are generated from specified Neumann boundary conditions. Thus, the partitioning technique can be used to generate each of the finite element solutions. The actual implementation of the bymoment method can significantly affect the efficiency. In the current scheme, the partitioning technique is used to find the FEM solution for the entire computational domain due to each Neumann boundary condition. This scheme is the simplest to implement, but it is computationally inefficient because the finite element solutions associated with the interior boundaries, $A_{i,m}^L$ and $A_{i,m}^R$, must be recomputed each time the partitioning technique is applied. A much more efficient scheme would be to generate FEM solutions for the bymoment method on each individual section. Then the coefficients associated with the bymoment method on each section can be placed in the coupling matrix. The solution of this coupling matrix provides

a complete solution to the scattering problem. We are currently implementing and testing this scheme.

III. NUMERICAL CONSIDERATIONS

To determine the efficiency of the *partitioning technique*, we perform an asymptotic analysis to determine the number of floating point operations required for this method and compare the results to the *standard method*, in which the FEM solutions are computed with a banded matrix solver based on LU decomposition. In addition, the memory requirements are compared. The analysis is performed for an electrically large two-dimensional square grid consisting of bilinear square elements with N nodes (one unknown per node) in the grid. To simplify the asymptotic analysis, we assume Neumann boundary conditions are enforced. For the standard method, the number of floating point operations for the LU decomposition is proportional to N^2 , while the backsolve is proportional to $N^{3/2}$. In the partitioning technique, the square grid is partitioned into M uniform sections. In this analysis, it is assumed that as the electrical size of the square increases, the number of sections M increases in such a way as to maintain a constant width for each section. The LU decomposition time associated with each section is greatly reduced because the bandwidth of the FEM matrix remains constant. Consequently, the sum of the decomposition times for all the sections is proportional to N . The partitioning method requires performing numerous backsolve operations on each section. The number of floating point operations required to perform the backsolves for all the sections is proportional to $N^{3/2}$. The solution of the final coupling matrix shown in Fig. 5 requires an operation count that is proportional to $M \cdot N^{3/2}$. Since M is proportional to $N^{1/2}$, the complexity of the partitioning method is equal to that of the standard method, but M is usually chosen to have values of $N^{1/2}/20$ to $N^{1/2}/40$. Thus, the operation count can be reduced by a large multiplicative factor. However, in practice, the cylinders must be very large—over 50 wavelengths in both directions—for the computation time associated with the coupling matrix to dominate the overall computation time. For smaller cylinders, we expect the backsolve time to be the dominant factor.

In addition to improving the computational efficiency, the partitioning technique can substantially reduce the memory storage from the standard method. The memory requirements of a banded matrix algorithm is $N^{3/2}$. In the partitioning technique, each section can be handled in a sequential manner; therefore, the same memory locations can be used for each section, resulting in a memory requirement of $N^{3/2}/M^2$. The extra factor of M in the denominator is due to the fact that the half-bandwidth of the FEM matrix for each section has been reduced by a factor of M . For the coupling matrix in Fig. 5, the memory requirement is proportional to NM , where the exact value is dependent upon the type of basis functions used in (2) and (3). For the problems that we consider in this paper, a factor of ten reduction in the memory is typical.

There are several other possible advantages of the partitioning technique. For problems in which the material properties change abruptly, the FEM grid must transition from one grid density to another at the material interface in order to maintain a constant nodal density per wavelength of the material. This transition is not easy to achieve for traditional finite element techniques. However, in the partitioning method each material can be placed in a separate section. Since the grid for each section is independent of the other sections, there is no need to provide a transition between the sections.

In partitioning the geometry into sections, there are many instances where two or more of the sections are geometrically identical. In these instances, the FEM solution need only be computed once for each set of identical sections, thereby further reducing the computational costs. A further advantage of the partitioning technique is that it is

easily parallelized for multiprocessor computers, because each section can be assigned to a processor without any need to communicate between the processors until the final evaluation of the coupling matrix. The final coupling matrix, which is block tridiagonal is also highly parallelizable [10].

IV. NUMERICAL RESULTS

To demonstrate the efficiency of the partitioning technique, we consider two boundary value problems and two associated scattering problems. The excitation for all the geometries is assumed to be a *TM* polarized plane wave of the form

$$E_z^{inc} = E_0 e^{-jk(x \sin \phi_i - y \cos \phi_i)} \quad (12)$$

The geometry for the boundary value problems consists of a rectangular region of free space. This geometry was chosen because the Neumann boundary condition for a free space region is well known. For the scattering problems, rectangular dielectric cylinders are considered. The parameter of interest is the echo width per wavelength L_e/λ [11], and it is given by

$$\frac{L_e}{\lambda} = \lim_{\rho \rightarrow \infty} \frac{2\pi\rho}{\lambda_0} \frac{|E_z^{sc}|^2}{|E_z^{inc}|^2} \quad (13)$$

where E_z^{sc} is the scattered electric field and λ_0 is the free space wavelength. The echo width is computed as a function of θ where θ is the angle defined from the positive *x* axis.

A finite element code based on the eight-node quadrilateral [1] element has been written to test this method. A nodal density of approximately 20 nodes per wavelength has been maintained for the numerical computations. This choice of nodal density is expected to produce accurate results [12]. The geometries of interest are electrically large; therefore, the FEM solutions may be subject to errors produced by the interior resonances of the computational domain [13]. To remove these errors, a small loss has been introduced in the computation domain. Thus, we set $\epsilon_r^* = \epsilon_r - j10^{-4}$, where ϵ_r is the relative permittivity given by the geometry. The computation times shown throughout this section are for the Cray YMP supercomputer. The basis and weighting functions Ψ_i and $w_{j,m}$ may be either entire domain functions such as sinusoidal functions with support over dS_m (Fig. 1) or else subdomain functions such as triangle functions with support over a subsection of S_m . For the numerical results presented in this paper, triangle functions with support over two elements (5 nodes) are used.

The first example is the problem of a plane wave propagating through a $2\lambda_0 \times 24\lambda_0$ region of free space. A finite element mesh of 16141 nodes (5200 elements) is used to discretize the entire computation domain. In Table I, a comparison is made between the standard method and the partitioning technique in which the domain has been divided into either six ($2\lambda_0 \times 4\lambda_0$) or 12 ($2\lambda_0 \times 2\lambda_0$) sections. Since the geometry of each section is the same, only one section is considered in the FEM computation. From the table, it is evident that the reduction in CPU time is undramatic, especially given the fact that the FEM solution is only computed in one section. The improvements that we expect from the asymptotic analysis are not present in this example because the bandwidth of the FEM matrix for each section is the same as the bandwidth for the entire computation domain. Thus, a reduction in CPU time cannot be expected for elongated geometries that are electrically large only along one direction. The reduction in memory requirements, on the other hand, is significant (a factor of more than eight for the 12-section case).

The second example is a scattering problem based on the first example. The scatterer is a $1\lambda_0 \times 12\lambda_0$ dielectric cylinder ($\epsilon_r = 4$). The mesh is the same as the one used in the first example. Because the

TABLE I
A COMPARISON OF CPU TIME AND MEMORY REQUIREMENT BETWEEN THE STANDARD METHOD AND THE PARTITIONING TECHNIQUE FOR FOUR DIFFERENT EXAMPLES

Example Number	Solution Method	CPU Time (Seconds)	Memory (Megawords)
1	Standard	16.2	2.5
	Partitioning (6 sections)	9.2	0.6
	Partitioning (12 sections)	7.4	0.3
2	Standard	156.5	6.7
	Partitioning (6 sections)	221.7	3.1
	Partitioning (12 sections)	288	2.8
3	Standard	388.5	26.1
	Partitioning (5 sections)	34.5	1.3
	Partitioning (10 sections)	27.6	1.1
4	Standard	808.0	28.3
	Partitioning (5 sections)	287.5	3.0
	Partitioning (10 sections)	274.3	2.8

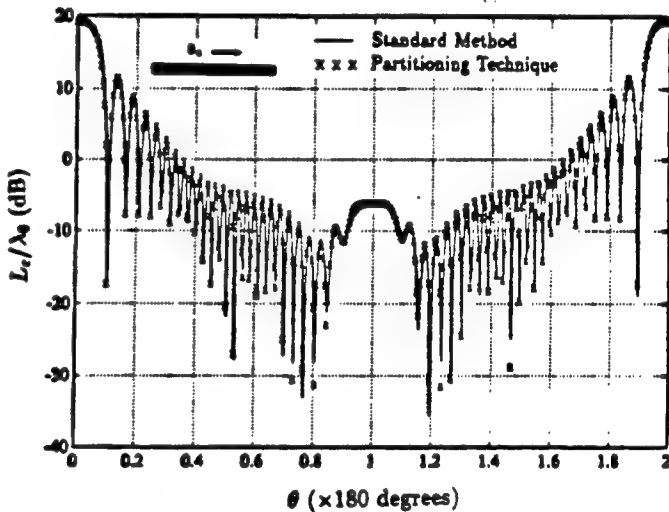


Fig. 6. Plot of the echo width as a function of θ for $1\lambda_0 \times 12\lambda_0$ cylinder with $\phi_i = 90^\circ$, $\epsilon_r = 4$. The solution from the standard method is compared against the solution from the partitioning technique.

geometry is electrically large, 226 expansion functions are required for accurate implementation of the bymoment method, which results in a dramatic increase in computation costs. The echo width solution is shown in Fig. 6 for an incidence angle of 90° . The results from the partitioning technique and the standard method are virtually identical, demonstrating that the partitioning has very little effect on the solution. Because the bandwidth of the FEM matrix is small, the majority of the CPU time is spent on the boundary truncation. From Table I, we see that the partitioning technique is less efficient than the standard FEM solution. This is due to the inefficient manner in which the bymoment method is coupled to the partitioning technique. The efficiency is expected to improve significantly with a better scheme. The memory savings has also been reduced compared to the first example due to the memory requirements of the bymoment method.

For the third example, we consider a plane wave propagating through a $9\lambda_0 \times 9\lambda_0$ region of free space. Because the region is a square, it is expected to exhibit the computational savings described in the asymptotic analysis. The computation domain is discretized with a grid consisting of 29105 nodes (9580 elements). For the partitioning technique, the domain is divided into both five ($9\lambda_0 \times 1.8\lambda_0$) and ten ($9\lambda_0 \times 0.9\lambda_0$) sections. In Table I the computation times are

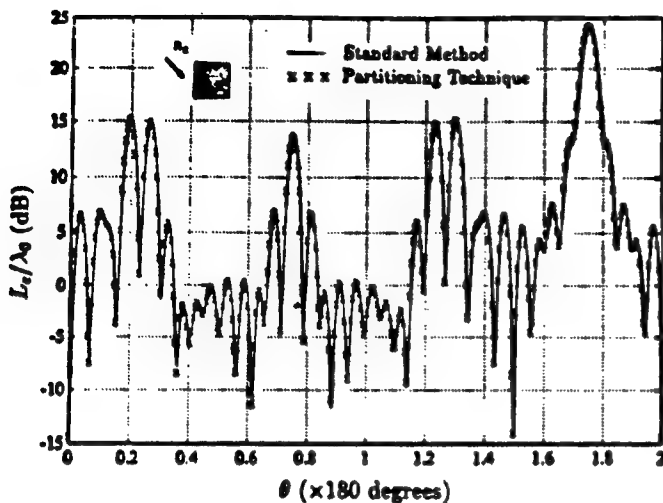


Fig. 7. Plot of the echo width as a function of θ for $4.5\lambda_0 \times 4.5\lambda_0$ cylinder with $\phi_1 = 45^\circ$, $\epsilon_r = 4$. The solution from the standard method is compared against the solution from the partitioning technique.

tabulated for all three cases. The reduction in CPU time is very significant (more than a factor of 14 for the ten-section case). Again, we took advantage of the fact that the FEM solution only needs to be computed in one section since all the sections are identical. However, if the computation is performed for all the sections, the CPU time increases from 34.5 s (for the five-section case) to approximately 65 s. Thus, for square dielectric cylinders with nonidentical sections, the computational savings is still very large. Furthermore, the memory requirements have been reduced from 26 Mwords for the standard method to 1.1 Mwords for the partitioning method.

In the fourth and final example, the plane wave scattering from a square dielectric ($\epsilon_r = 4$) cylinder with sides of length $4.5\lambda_0$ is considered. The FEM grid is the same as the one used in the third example, and the bymoment boundary condition is implemented with 180 expansion functions. The echo width solution is shown in Fig. 7 for $\phi_1 = 45^\circ$. The two methods produce virtually identical results. A comparison of the memory and CPU requirements for this example is shown in Table I. For the partitioning technique, the computation domain is divided into both five and ten sections. The reduction in CPU time is not as dramatic as in the third example because of the inefficient manner in which the bymoment method is coupled to the partitioning technique. However, the savings are still very significant in both computation time and memory costs.

V. SUMMARY

A new method has been presented to decrease the solution time for the finite element modeling of electromagnetic scattering problems. In this method, the geometry is partitioned into smaller sections. Within each section, a set of finite element solutions is generated that are independent of the other sections. The sections are then coupled by the use of the field continuity conditions. The resulting matrix equation is block tridiagonal and significantly smaller than the original FEM matrix equation. An asymptotic analysis was provided to demonstrate the potential efficiency of this method. The method was coupled to the bymoment method in order to solve the scattering problem. Finally, numerical results were presented to demonstrate both its accuracy and efficiency for some canonical geometries.

REFERENCES

- [1] J. E. Akin, *Application and Implementation of Finite Element Methods*. San Diego: Academic, 1982.
- [2] A. George and J. W. Liu, *Computer Solution of Large Sparse Positive Definite Systems*. Englewood Cliffs, NJ: Prentice-Hall, 1981.
- [3] K. R. Umashankar and A. Taflove, "Numerical analysis of electromagnetic scattering from electrically large objects using spatial decomposition techniques," *IEEE Trans. Antennas Propagat.*, vol. 40, pp. 867-877, Aug. 1992.
- [4] C. M. Butler, "Diakoptic theory and the moment method," *IEEE Antennas Propagat. Soc. Int. Sym. Dig.*, vol. 1, pp. 72-75, May 1990.
- [5] W. C. Chew and C. C. Lu, "NEPAL-An $N^{1.5}$ algorithm for solving volume integral equations," *IEEE Antennas Propagat. Soc. Int. Sym. Dig.*, vol. 1, pp. 184-187, July 1992.
- [6] T. M. Wang and H. Ling, "Electromagnetic scattering from three-dimensional cavities via a connection scheme," *IEEE Trans. Antennas Propagat.*, vol. 39, pp. 1505-1513, Oct. 1991.
- [7] A. C. Cangellaris and R. Lee, "The bymoment method for two-dimensional electromagnetic scattering," *IEEE Trans. Antennas Propagat.*, vol. 38, pp. 1429-1437, Sept. 1990.
- [8] C. T. Spring and A. C. Cangellaris, "A partitioning approach to the electromagnetic characterization of large two and three dimensional structures," *1992 URSI Radio Science Meeting Digest*, p. 230.
- [9] K. K. Mei, "Unimoment method of solving antenna and scattering problems," *IEEE Trans. Antennas Propagat.*, vol. 22, pp. 760-766, Nov. 1974.
- [10] M. Berry and A. Sameh, "Multiprocessor schemes for solving block tridiagonal linear systems," *Int. J. Supercomputing Appl.*, vol. 2, pp. 37-57, 1988.
- [11] R. F. Harrington, *Time-Harmonic Electromagnetic Fields*. New York: McGraw-Hill, 1961.
- [12] R. Lee and A. C. Cangellaris, "A study of discretization error in the finite element approximation of wave solutions," *IEEE Trans. Antennas Propagat.*, vol. 40, pp. 542-549, May 1992.
- [13] L. W. Pearson, A. F. Peterson, L. J. Bahrmasel, and R. A. Whitaker, "Inward-looking and outward-looking formulations for scattering from penetrable objects," *IEEE Trans. Antennas Propagat.*, vol. 40, pp. 714-720, June 1992.

Analysis of Electromagnetic Scattering from a Cavity with a Complex Termination by Means of a Hybrid Ray-FDTD Method

Robert Lee, *Member, IEEE*, and Tse-Tong Chi, *Student Member, IEEE*

Abstract—The electromagnetic modeling of engine cavities is a very difficult task because the electrical size of the cavity is very large, while the engine termination is geometrically complex. High-frequency techniques can adequately model the cavity, but perform poorly when applied to the termination. Low-frequency techniques are currently infeasible for such large geometries because of the large memory and computation time requirements. In this paper, we present a hybrid method which combines the most attractive features of the low- and high-frequency techniques. The finite-difference time-domain (FDTD) method is applied to the small region surrounding the termination. The remainder of the cavity is modeled with ray methods. To validate this method, we consider two-dimensional cavities with complex terminations. Our results are compared against those found from a hybrid combination of the modal method and the method of moments.

I. INTRODUCTION

THE PROBLEM of electromagnetic scattering from an open-ended cavity structure is an important problem in the area of radar scattering. Among other things, it models the radar scattering from a jet engine inlet. Traditionally, high-frequency methods have been applied to solve such problems. In recent years, two ray-based methods have been widely used to model the scattering properties of electrically large cavities of arbitrary shape. These are the “shooting and bouncing ray” (SBR) method [1] and the “generalized ray expansion” (GRE) method [2]. However, these two methods have only been shown to work for cavities with planar or very simple terminations. The terminations of practical interest are often geometrically complex (such as the fan blades in a jet engine), and the ray methods are not expected to be able to properly account for the diffraction effects of the termination. In addition, the termination may contain materials which are not perfectly conducting. Thus, a solution based purely on ray methods may be drastically different from the correct solution. Low-frequency techniques such as the moment method (MM) [3], the finite-element method (FEM) [4], and the finite-difference time-domain method (FDTD) [5], [6] can accurately model the complex termination as well as the rest of the cavity, but unfortunately, the computa-

tion costs to model such a large geometry exceed even the most powerful supercomputer.

In this paper, we present a hybrid method which combines both high- and low-frequency methods to overcome the shortcomings of either methods. A ray method is used to track the fields from the mouth of the cavity up to an arbitrarily defined planar surface close to the termination. These fields act as the excitation for the termination region, which is modeled by a low-frequency method. In our case, we have chosen the FDTD method because of its computational efficiency and its capability to obtain multiple-frequency data from a time history solution. It is expected that this hybrid method can provide a solution that is almost as accurate as if the solution had been obtained from low-frequency techniques but at a very small fraction of the computation costs.

The paper is divided into three sections after this introduction. Section II describes the details of the hybrid method including a description of the coupling between the ray method and the FDTD method. Although the formulation of the hybrid method is for the general case of a three-dimensional (3D) cavity with an arbitrary termination, the validation of this method is performed in two dimensions (2D) in order for us to more easily analyze the accuracy and robustness of this method before implementation in 3D. In Section III, results are presented for the 2D geometry of a parallel plate waveguide containing perfectly conducting terminations. These results are compared to a hybrid modal-MM method to demonstrate the accuracy of the hybrid ray-FDTD technique. Finally, a brief summary of this paper is provided in the last section.

II. THE HYBRID RAY-FDTD METHOD

In this section, a brief discussion of the GRE and the FDTD methods is given, followed by a description of how the coupling between the frequency-domain GRE method and the FDTD method is accomplished. The use of absorbing boundary conditions and the computation of the cavity scattered field are then considered.

A. The GRE Method

SBR and GRE are the two ray methods that have been considered for use in combination with FDTD for the hybrid method. Many papers have already been published on the two ray methods and their applications in cavities,

Manuscript received February 3, 1993; revised July 20, 1993. Work supported by NASA grant NAG3-1359.

The authors are with the ElectroScience Laboratory, Department of Electrical Engineering, The Ohio State University, 1320 Kinnear Road, Columbus, Ohio 43212.

IEEE Log Number 9213072.

corner reflectors, and antennas [7]–[12]. For the hybrid method, we have chosen GRE over SBR after due consideration of their accuracy and efficiency. As in any hybrid method, the accuracy of the solution at the interface between the methods is an important factor in the overall accuracy of the hybrid method. It has been shown in [13] that the ray fields predicted by GRE inside a semi infinite parallel-plate waveguide cavity is more accurate than those obtained by SBR. The difference in the accuracy of these ray methods is attributed to the difference in the coupling of the (externally applied) incident fields into the waveguide cavity. GRE intrinsically includes the incident fields diffracted into the cavity by the open end through the integration of the equivalent currents over the aperture of the cavity. SBR, on the other hand, does not include the edge-diffracted fields. Depending on the electrical size of the aperture and the length of the cavity, the edge-diffracted fields may eventually affect the geometrical optics fields intercepted by the aperture. In terms of efficiency, SBR generally requires less rays, which also means less ray tracing to perform, than in GRE for a single incident angle. However, a new set of rays has to be traced in SBR, including computing their divergence factors and reflection coefficients, for every new incident angle, whereas the same set of rays is used in GRE regardless of the incident angle of the field (the latter will become evident later). So GRE is better suited for scattering problems where the scattered field is required over a range of angles. Therefore, for accuracy and efficiency, we have chosen GRE over SBR for the hybrid method.

Because the detailed formulation of the GRE method can be found in [2], only the working principles of the method will be described. In this method, the incident field at the aperture of the cavity is replaced by equivalent surface currents via Kirchhoff's approximation. These equivalent currents radiate the desired fields into the cavity interior as shown in Fig. 1. For large cavities, the aperture is divided into a number of smaller subapertures. A cone of ray tubes is then launched into the cavity from the phase center of each subaperture. The ray tubes are tracked using the central rays of the respective ray tubes. The central rays are tracked as ordinary geometrical optics rays. The exiting ray tubes contribute to the scattered field of the cavity. The scattered field is computed by physical optics approximation, taking into account the wavefront curvature, the size, and the shape of the ray tube associated with each exiting ray [2], [14]. A more efficient method for obtaining the scattered field will be presented in a later section.

In GRE, each ray tube is weighted by the far-field approximation of the radiation pattern of the subaperture (from which that ray tube has originated) with the cavity walls absent. Specifically, the electric field along the p th ray of the l th subaperture prior to any reflection is given by

$$E_{pl}(r) = C_l(\hat{r}_{pl}) \frac{\exp(-jk_0 r_{pl})}{r_{pl}} \quad (1)$$

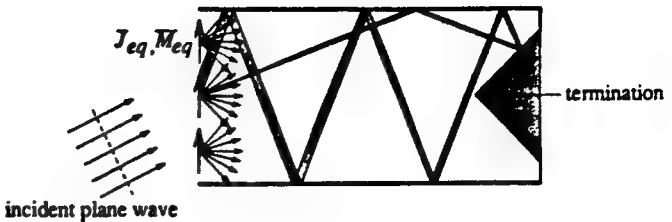


Fig. 1. The generalized ray expansion method.

where k_0 is the propagation constant of the medium in which the cavity is embedded. r_{pl} is the position vector of a point along the p th ray with respect to the phase center O_l of the l th subaperture. $C_l(\hat{r}_{pl})$ is the far-field vector radiation pattern of the electric field evaluated in the direction \hat{r}_{pl} in the absence of the cavity walls. It is given by

$$C_l(\hat{r}_{pl}) = \frac{jk_0 Z_0}{4\pi} \int \int_{S_l} [\hat{r}_{pl} \times \hat{r}_{pl} \times J_s^{eq}(r')] + Y_0 \hat{r}_{pl} \times M_s^{eq}(r')] \exp(jk_0 \hat{r}_{pl} \cdot r') ds', \quad (2)$$

where r' is the vector from O_l to the equivalent sources on the subaperture S_l . Equation (2) can be evaluated numerically or in closed form depending on the field excitation and the shape of the subaperture [9].

As each ray tube undergoes multiple reflections within the cavity, its field amplitude is modified by divergence factors and reflection coefficients. In particular, the electric field $E(r_i)$ of the ray immediately after reflection from the point r_i is found iteratively from the field $E(r_{i-1})$ immediately after the previous reflection point r_{i-1} through the relation

$$E(r_i) = \Gamma \cdot E(r_{i-1})(DF)_{i-1} e^{-jk_0 s}, \quad (3)$$

where $s = |r_i - r_{i-1}|$, Γ is the planar dyadic reflection coefficient evaluated at r_i and $(DF)_{i-1}$ is the divergence factor governing the spreading of the ray tube associated with the ray after reflection from the point at r_{i-1} . The divergence factor is usually evaluated via the Q -matrix formulation of Deschamps [15].

From (1)–(3), it is clear that only one set of rays needs to be traced for all the incident angles because the ray divergence factors and reflection coefficients are functions of the ray paths and not the incident angle; only the initial amplitude of the ray field is a function of the incident angle.

The most serious limitation in ray methods (like the GRE and SBR methods) is their inability to account for fields arising from discontinuities like edges and tips inside the cavities. As such, ray methods are not expected to produce reasonable results for cavities with complex terminations.

B. The FDTD Method

FDTD is a direct solution of Maxwell's time-dependent curl equations [5], [6]. It applies second-order accurate central-difference approximations for both the space and

time derivatives of the electric and magnetic fields directly to the differential operators of the curl equations. We do not derive the difference equations here because they can be found in many papers, including those given above. Instead, we consider some of the attractive features of FDTD that are useful for our hybrid method.

FDTD models the actual real-time behavior of EM fields which makes it suitable for impulsive and transient analysis. The frequency spectrum can also be easily obtained via Fourier transformation of the FDTD time solution. In contrast, the use of frequency-domain methods to get the frequency spectrum or time variation requires solving the problem repeatedly for multiple frequencies in the frequency range of interest.

In FDTD, the field computations involve only simple arithmetic operators with no matrix manipulation. The number of floating-point operations per time step and the memory storage are both proportional to the number of unknowns, n , compared to n^3 and n^2 , respectively, in frequency-domain methods such as the method of moments (assuming LU decomposition). The equations in FDTD can also be easily vectorized for the Cray computer. Despite these advantages, FDTD is computationally costly for solving electrically large problems. For example, a rectangular cavity, with a cross section of $30\lambda \times 40\lambda$ and a depth (or length) of 100λ , requires 5.76 billion unknowns for a mesh density of 20 cells/ λ . Moreover, the FDTD field equations have to be repeatedly evaluated for at least 8000 time steps (or iterations, assuming two time steps for the field to traverse from one cell to another along the length of the cavity) before the interior irradiated field can be observed at the aperture of the cavity. Finally, FDTD cannot easily model curve boundaries/surfaces although some solutions have been proposed to partly overcome this shortcoming [16], [17].

C. Coupling between Ray and FDTD

As was alluded to earlier, FDTD can be computationally inefficient when it is used to solve electrically large geometries. For the previous example of the rectangular cavity, most of the computational time and effort are wasted in the two-way propagation of the field along the length of the cavity. The proposed hybrid ray-FDTD method overcomes this inefficiency by using a ray method, specifically GRE, to propagate the fields from the aperture to the (vicinity of the) termination. However, since it is difficult to apply ray methods to complex terminations, FDTD is used to determine the interaction of the cavity fields with the termination.

As with most EM hybrid methods, the coupling between the individual methods has to be handled with care. Consider the cavity shown in Fig. 2. The cavity has been divided into three regions corresponding roughly to the air intake, the engine, and the exhaust sections of a jet engine inlet. The imaginary surface S_{T_1} separates regions 1 and 2, while S_{T_2} separates regions 2 and 3. In region 1, the cavity is assumed to be smoothly varying for high-frequency methods like ray methods to be valid. Ray

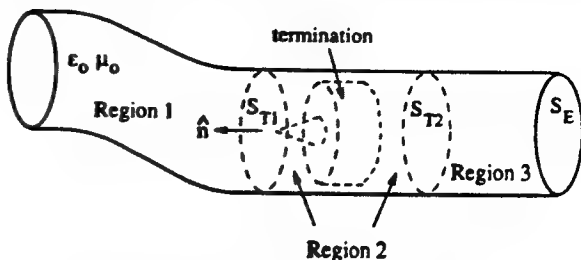


Fig. 2. Geometry of a cavity with termination.

tubes are traced from the aperture of the cavity to S_{T_1} , where they are summed to form a high-frequency solution of the cavity fields across S_{T_1} . This solution on S_{T_1} is used as the excitation for the FDTD computation in region 2.

We will now describe two approaches to the coupling between the GRE and the FDTD methods. Depending on the size of a ray tube when it reaches S_{T_1} , it will either not intersect any of the FDTD grid points on S_{T_1} or it will intersect one or more of those grid points. Therefore, different ray tubes will contribute differently to the total field of a grid point. Moreover, it is possible that some grid points will not have any ray tubes intersecting them. As a result, the *incident* fields on S_{T_1} , evaluated via rays will not be smoothly varying. In order to obtain a smoothly varying as well as an accurate field on S_{T_1} , the size of the ray tube can be restricted so that it will only intersect one FDTD grid point. Alternatively, some form of interpolation can be applied to the ray tubes that intersect more than one grid point. In both of these approaches, a ray tube is launched and tracked via its central ray to S_{T_1} . The projected ray tube *area* (for the 3D case; *width* for the 2D case) on S_{T_1} is then determined. If this area is greater than some specified area, A_p , the ray tube is subdivided and the process of tracking and determining the projected area of the smaller ray tubes is repeated. In the first approach, A_p is equal to the FDTD grid spacing (usually $\lambda/20$) for the 2D case so that if the projected ray tube *width* is less than A_p , that ray tube can intersect at most one FDTD grid point on S_{T_1} . In such an event, the field specified by the central ray will be added to the intersected grid point. Ray tubes that do not intersect any grid point are ignored.

For the second approach, A_p is larger, but no greater than $\lambda/2$ and $(\lambda/2)^2$ for the 2D and 3D cases, respectively, for reasons given in [2]. In our 2D implementation, we have used $A_p = \lambda/4$ for greater accuracy in the evaluation of the fields on S_{T_1} . Since a larger ray tube may intersect more than one FDTD grid point on S_{T_1} , its contribution to the field on S_{T_1} is determined by converting its ray field into modal fields. Specifically, the contribution of the ray field to the modal coefficients are determined by integrating the ray field over the projected area of the ray tube assuming a linear phase variation in the field over the projected area with respect to the field of the central ray. This approach assumes that the fields on S_{T_1} are expressible in terms of parallel-plate waveguide modes for 2D problems. This assumption can usu-

ally be satisfied by a suitable choice of S_{T_1} . In realistic 3D problems, there is usually a narrow section in front of the termination which is cylindrical so that the fields in this narrow section can also be expressed in terms of modes. In any case, when the modal coefficients have been obtained by summing the contributions due to *all* the ray tubes, the desired field at each FDTD grid point on S_{T_1} can be determined.

Comparing the two approaches, it is clear that the first approach requires more ray tracing (which means more computational time and storage) than the second approach because of the smaller A_p . However, once the rays are traced, the first approach uses only a simple summation of the ray fields to obtain the desired fields at the FDTD grid points on S_{T_1} . The second approach is less efficient in this latter aspect because it has to compute the modal coefficients and then sum the modal fields to get the desired fields. However, in realistic 3D problems, the first approach may not be viable because the amount of ray tracing can become overwhelmingly excessive.

Another consideration in the coupling of the GRE and FDTD methods is the selection of a suitable time variation for the excitation since the former is a frequency-domain method while the latter is a time-domain method. There are two possible schemes for the time variation: the sinusoidal steady-state time variation [18] and the pulsed (usually Gaussian or raised-cosine) time variation. For the steady-state FDTD, the ray solution on S_{T_1} is evaluated only at a single frequency of interest. Based on the complex ray field solution at S_{T_1} , the excitation can be made to vary sinusoidally with time. For the pulsed FDTD, there are two possible alternatives. For the first alternative, the ray solution on S_{T_1} is computed over a range of frequencies corresponding to the frequency content of the pulse. The excitation can then be obtained by an inverse Fourier transform of the product of the ray solution and the Fourier transform of the pulse. This alternative is not attractive because the resultant inverse transform will have a wide time window with a number of significant pulses due to the different arrival times at S_{T_1} of the reflected, diffracted, and reflected-diffraction fields. A better alternative is to use a basis (e.g., modes) as excitation for the pulsed FDTD to characterize the termination section in terms of a termination scattering matrix. This scattering matrix, together with the ray solution on S_{T_1} (expressed also in terms of the basis set), can then be used to find the cavity scattered field. The pulsed time variation scheme is more efficient for problems which require multiple frequency solutions while the steady-state scheme is more efficient for problems which require only a single frequency solution.

Regardless of the time variation used, the excitation produces a wave which propagates toward the termination and interacts with it. For the geometry shown in Fig. 2, part of the wave may be transmitted to region 3 through S_{T_2} while the remainder is reflected back toward S_{T_1} . If we assume that the waves leaving region 2 through the imaginary surfaces S_{T_1} and S_{T_2} do not return, then an absor-

ing boundary condition (ABC) such as the ones introduced by Higdon [19], [20] or Mur [21] can be applied in the FDTD computations at each of the two surfaces. The above assumption is reasonable because most jet engine inlets are shaped in such a way that there is very little energy that returns to region 2 upon its exit from there. Otherwise, we can convert the waves leaving region 2 back into rays (using GRE) and track those rays that return to region 2. These returning rays act as an additional excitation.

D. Absorbing Boundary Conditions at S_{T_1} and S_{T_2}

As mentioned previously, absorbing boundary conditions (ABCs) are applied at the imaginary boundary surfaces S_{T_1} and S_{T_2} for the proper transmission of waves through these surfaces. However, the two ABCs cannot be implemented in the same way because of different field conditions at their respective boundary surfaces. With reference to Fig. 2, the ABC at S_{T_1} has to properly account for the waves which pass through S_{T_1} in both directions; it has to account for the *incident* excitation at S_{T_1} and the scattered field due to the termination. In contrast, the absorbing boundary at S_{T_2} only has waves transmitted through it from region 2 to region 3 assuming that there are no waves transmitted through S_{T_2} from region 3 to region 2 (recall discussion in previous section).

The ABC at S_{T_1} has to transmit (or absorb) the waves that are *scattered* by the termination toward S_{T_1} without destroying or affecting the *incident* excitation at S_{T_1} . We will demonstrate how this function can be accomplished with the second-order ABC of Mur [21] in a 2D problem. Applying the ABC given by (17) of [21] to the *scattered* electric field $E_{z,s}$ (for the TM_z case) at S_{T_1} , we have

$$\begin{aligned} E_{z,s}^{n+1}(0, j) = & E_{z,s}^n(1, j) a_1 [E_{z,s}^{n+1}(1, j) - E_{z,s}^n(0, j)] \\ & - a_2 [H_{x,s}^{n+1/2}(0, j + \frac{1}{2}) - H_{x,s}^{n+1/2}(0, j - \frac{1}{2}) \\ & + H_{x,s}^{n+1/2}(1, j + \frac{1}{2}) - H_{x,s}^{n+1/2}(1, j - \frac{1}{2})] \end{aligned} \quad (4)$$

(following Mur's FDTD indexing; see Fig. 3 also for indexing), where $E_{z,s}$ and $H_{x,s}$ are the fields *scattered* by (or reflected from) the termination. The constants a_1 and a_2 are given by

$$a_1 = \frac{c_0 \Delta t - \Delta x}{c_0 \Delta t + \Delta x},$$

$$a_2 = \frac{\mu_0 c_0^2 \Delta t \Delta x}{2 \Delta y (c_0 \Delta t + \Delta x)}.$$

Replacing the scattered field components ($E_{z,s}$, $H_{x,s}$) with

$$(E_{z,s}, H_{x,s}) = (E_z, H_x) - (E_{z,i}, H_{x,i}), \quad (5)$$

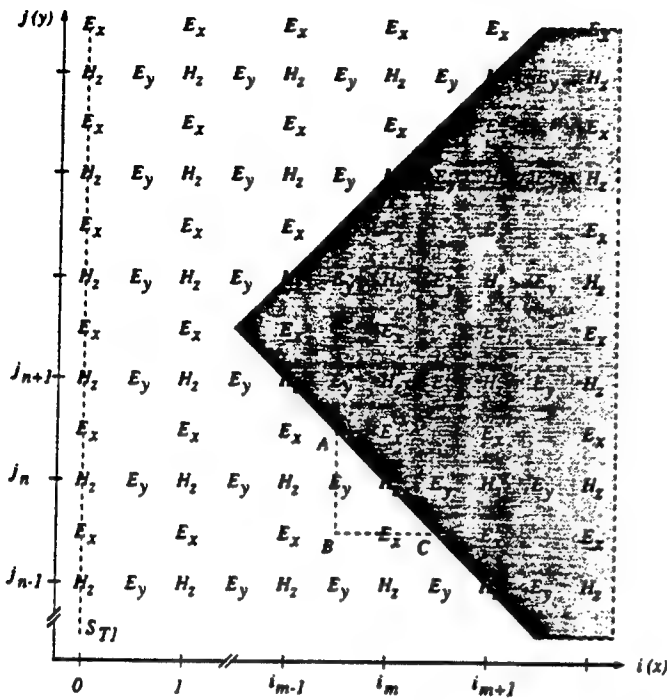


Fig. 3. Geometry of a wedge with respect to the FDTD grid for the TE_z case.

where the subscript i in $E_{z,i}(H_{x,i})$ denotes the *incident* component of the *total* E_z (H_x) field, (4) becomes

$$\begin{aligned}
 E_{z,i}^{n+1}(0,j) = & E_z^n(1,j) - E_{z,i}^n(1,j) + a_1 \\
 & \cdot [E_z^{n+1}(1,j) - E_{z,i}^{n+1}(1,j) - E_{z,i}^n(0,j)] \\
 & - a_2 [H_x^{n+1/2}(0,j + \frac{1}{2}) \\
 & - H_{x,i}^{n+1/2}(0,j + \frac{1}{2}) - H_x^{n+1/2}(0,j - \frac{1}{2}) \\
 & + H_{x,i}^{n+1/2}(0,j - \frac{1}{2}) \\
 & + H_x^{n+1/2}(1,j + \frac{1}{2}) - H_{x,i}^{n+1/2}(1,j + \frac{1}{2}) \\
 & - H_x^{n+1/2}(1,j - \frac{1}{2}) + H_{x,i}^{n+1/2}(1,j - \frac{1}{2})]. \quad (6)
 \end{aligned}$$

Except for $E_z^{n+1}(1,j)$ and $E_{z,i}^{n+1}(1,j)$, all the other field components in (6) are computed values for the previous (one or half) time step. $E_z^{n+1}(1,j)$ can be calculated for the current time step from the regular (total-field) difference equation. $E_{z,i}^{n+1}(1,j)$ can be obtained via the ray method (as was done for the excitation at the absorbing boundary) or from the propagation of the *incident* excitation. After $E_{z,i}$ on S_{T_1} has been found, the total field components of H_x and H_y in region 2 can be updated via the regular FDTD equations.

The procedure described above for obtaining the scattered fields at S_{T_1} due to the reflection of the fields from the termination has to be used whenever the steady-state sinusoidal time variation is chosen for the FDTD computation in region 2. However, this procedure may or may not be necessary when the pulsed time variation is chosen, depending on the time window of the excitation and the closest distance between S_{T_1} and the termination.

The ABC at S_{T_2} does not require any special treatment like the one at S_{T_1} if we assume that waves are transmitted through S_{T_2} only from region 2 to region 3 and not vice versa. In this case, the transmitted field is also the total field. Therefore, any suitable ABC for the absorption of the total field at S_{T_2} can be applied. Note that the ABC (4) can also be applied at S_{T_2} with the scattered field variables replaced appropriately by the total field variables (with the proper spatial indices).

E. Scattered Field Computation

To determine the cavity scattered fields, the appropriate field solutions in regions 1 and 2 have to be used. One possible way of finding the cavity scattered field is to launch GRE rays into region 1 using the FDTD solution at S_{T_1} . These rays are tracked to the front aperture of the cavity where aperture integration can be applied to find the scattered field. Unfortunately, this method requires that rays be traced both into the cavity for the incident excitation at S_{T_1} and out of the cavity for the cavity scattered field computation.

A more suitable and efficient way for finding the cavity scattered field is based on the termination reciprocity integral developed by Pathak and Burkholder [22]. This integral is given by

$$E_s(P) \cdot P_t \equiv \int_{S_{T_1}} (E_s \times H_t - E_t \times H_s) \cdot \hat{n} ds, \quad (7)$$

where $E_s(P)$ is the desired cavity scattered field at the observation point P and P_t is the strength of an electric current point (test) source. (E_s, H_s) are the fields scattered by the termination in the cavity while (E_t, H_t) are the fields radiated by the test source in the presence of the cavity structure without the termination. \hat{n} is the unit vector normal to the surface S_{T_1} as shown in Fig. 2. The approximation in (7) assumes that the source and observer are in direct view of the open front end so that the contribution to $E_s(P)$ from the scattered field exiting through S_E is negligible compared to the fields exiting through S_{T_1} .

To see the usefulness of (7), consider how the cavity scattered fields are obtained using a purely ray-based approach. For example, in the original implementation of SBR [1], [7], two-way (in and out of the cavity) ray tracing has to be performed before the scattered field can be determined via aperture integration. With the reciprocity integral, the rays are only traced from the open end of the cavity to the termination and back to S_{T_1} . Therefore, the amount of ray tracing is basically reduced by about half. This reduction is even more significant when the reciprocity integral is used in the hybrid method because the rays are only traced from the open end to S_{T_1} .

From (7), we see that the integral is independent of the method(s) used to find the two sets of *tangential* fields on S_{T_1} . It is particularly easy to apply the integral to find the backscattered field in our hybrid method since both sets of fields at S_{T_1} are readily available. Specifically, for backscatter computation, (E_t, H_t) is the initial excitation

on S_{T_1} , evaluated by the GRE method for the FDTD computation in region 2; its evaluation has already been described earlier. (E_s, H_s) is the termination scattered field that is transmitted through S_{T_1} from region 2. It has to be evaluated on S_{T_1} from the FDTD algorithm. However, the tangential E and H fields in a Yee cell lie on different planes. In particular, the tangential E and H planes are half a cell width apart in the direction normal to both of these planes. Consider for example, the 2D TE₂ case shown in Fig. 3, where the tangential magnetic field $H_z(0, j)$ lies on S_{T_1} and the tangential electric field $E_y(\frac{1}{2}, j)$ lies on a plane parallel to S_{T_1} at $\Delta x/2$ away. To obtain $E_{y,s}(0, j)$ (which is symbolically, the termination scattered field $E_{y,s}$ on S_{T_1}), an extrapolation of the neighboring values of $E_{y,s}$ is used. Specifically, we assumed that the gradient of the scattered field $E_{y,s}$ in the normal direction of S_{T_1} , $dE_{y,s}/dx$, at $x = \Delta x/4$ is equal to that at $x = \Delta x$, so that

$$E_{y,s}(0, j) = \frac{3}{2}E_{y,s}(\frac{1}{2}, j) - \frac{1}{2}E_{y,s}(\frac{3}{2}, j). \quad (8)$$

For the steady-state FDTD, the scattered field components ($E_{y,s}$) on the right-hand side of (8) are replaced by the difference between their respective total (E_y) and incident ($E_{y,i}$) field components. This extrapolation scheme can be similarly applied to the tangential electric or magnetic field in the 3D case. When all the tangential fields within the integral of (7) have been appropriately manipulated into the frequency domain, the cavity scattered field $E_s(P)$ can be computed.

In summary, the hybrid ray-FDTD method uses high-frequency ray solutions as input excitation for the evaluation of the termination scattered field via the low-frequency FDTD method; the scattering of the cavity is then obtained via the termination reciprocity integral. The hybrid ray-FDTD method combines the efficiency of the ray method (and the reciprocity integral) with the modeling flexibility of the FDTD method. At the same time, it overcomes some of the limitations of the individual methods in analyzing the scattering from a cavity.

III. RESULTS

The hybrid GRE-FDTD method has been implemented in three different programs (see Table I) using various combinations of ray tracing and time variations to determine the radar cross section (RCS) of parallel-plate cavities with different PEC plug terminations. Program 1 implements the GRE method such that the projected areas of the ray tubes are less than $\lambda/20$ to find the *incident* field on S_{T_1} , while the other two programs implement the GRE method such that the ray fields are converted into modes to find the same fields. Programs 1 and 2 implement the FDTD algorithm using the steady-state sinusoidal time variation, while program 3 implements the FDTD algorithm using the basis-pulsed time variation approach.

In all three programs, the aperture of the cavity is divided into three subapertures from which rays are

TABLE I
DIFFERENT IMPLEMENTATIONS OF THE HYBRID
GRE-FDTD METHOD

Program	GRE	FDTD
1	$A_p = \lambda/20$	sinusoidal
2	$A_p = \lambda/4$	sinusoidal
3	$A_p = \lambda/4$	pulsed-basis

launched within an angle of $\pm 75^\circ$ of the cavity axis to compute the excitation at S_{T_1} . S_{T_1} is fixed at 4λ from the closed end of the cavity. For the FDTD algorithm, a $\lambda/20 \times \lambda/20$ spatial grid is used (unless it is specified otherwise) with a time step of $\Delta x/(2c_0)$; Mur's [21] ABC is applied at S_{T_1} to absorb the fields scattered toward S_{T_1} by the termination. No ABC is implemented at S_{T_2} since region 3 (see Fig. 2) is nonexistent for our terminated cavity. The scattered field is obtained via the reciprocity integral (7) which is now exact since S_E is perfectly conducting for the terminated (PEC) parallel-plate waveguide.

In the following examples, we will only present results obtained via program 2. These results are compared with reference solutions obtained via the hybrid asymptotic modal-method of moments (modal-MM) [23]. The results from the other two programs are not presented here because there is little difference between their results and that of program 2. In fact, the purpose of programs 1 and 3 is to check the accuracy of the approach employed in program 2. Moreover, program 3 validates the time-domain (pulsed-basis) approach which has great potential in (2D and 3D) scattering problems where the cavity RCS is required at multiple frequencies. For the purpose of this paper, the results from program 2 are sufficient to illustrate the utility and accuracy of the hybrid method.

Figures 4 and 5 show the RCS patterns of a 9.6λ -wide and 30λ -long parallel-plate waveguide cavity with a $2\lambda \times 4\lambda$ rectangular PEC plug termination for the TM₂ and TE₂ cases, respectively. The GRE-FDTD patterns in both figures show excellent agreement with the corresponding modal-MM patterns. The slight differences between the GRE-FDTD and the modal-MM solutions can be attributed to two causes. One of the causes is the inability of the ABC to absorb the higher-order modes excited by the rectangular plug termination. These higher-order modes result from the reflection and edge diffraction of the fields from the termination. They are particularly significant at larger incident angles since the termination *reflected* fields (which are the incident fields after undergoing multiple reflections in the termination section) are incident at large angles from the normal on the absorbing boundary S_{T_1} . These higher-order modes are not transmitted (or absorbed) as well as the lower-order modes by the second-order Mur's ABC (see Table II [24]). In addition, their multiple reflections between the absorbing boundary and the termination result in appreciable errors in the scattered field. Another source of

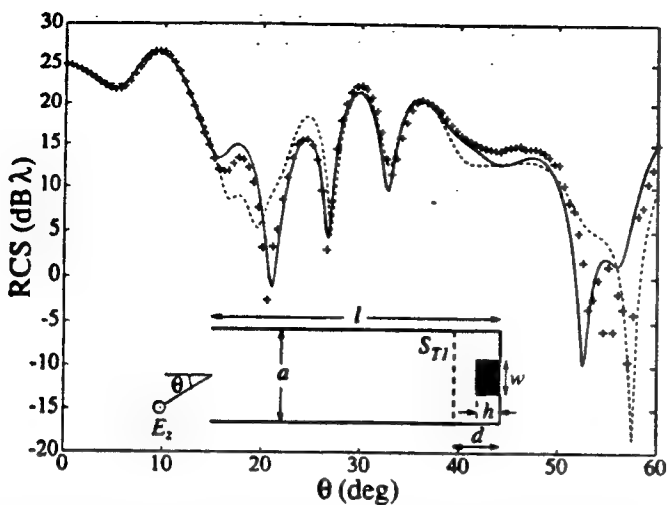


Fig. 4. Radar cross-section patterns of parallel-plate cavity with a rectangular-shaped PEC plug termination using the hybrid modal-MM, GRE-FDTD, and GRE methods. $a = 9.6\lambda$, $l = 30\lambda$, $d = 4\lambda$, $h = 2\lambda$, $w = 4\lambda$; TM_z ; —, modal-MM; + + +, GRE-FDTD; ---, GRE (three subapertures).

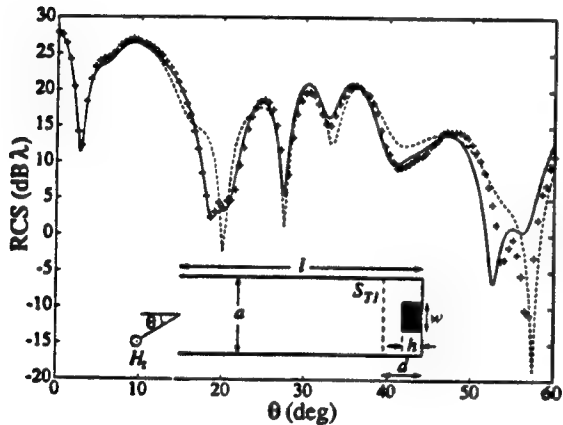


Fig. 5. Radar cross-section patterns of parallel-plate cavity with a rectangular-shaped PEC plug termination using the hybrid modal-MM, GRE-FDTD, and GRE methods. $a = 9.6\lambda$, $l = 30\lambda$, $d = 4\lambda$, $h = 2\lambda$, $w = 4\lambda$; TE_z ; —, modal-MM; + + +, GRE-FDTD; ---, GRE (three subapertures).

error is the ray solution on S_{T_1} . These solutions are less accurate at large incident angle θ than at small θ . This difference in accuracy is a result of limiting the ray solution to those rays whose launch angles are within $\pm 75^\circ$ of the cavity axis. At large θ , this (artificial) angular limit may not be adequate. For example, for an incident angle of 60° , the magnitude of the radiation power pattern of each subaperture at 75° is -8 dB (40%) with respect to the beam maximum, while the magnitude of the first and second side lobes are -9 dB (35%) and -13 dB (22%), respectively. Therefore, significant contribution by rays whose launch angles are greater than 75° are omitted from the final ray solution on S_{T_1} .

Also shown in Figs. 4 and 5 are the respective patterns obtained using the GRE method alone. In this purely

TABLE II
REFLECTION COEFFICIENTS FOR THE MUR ABSORBING BOUNDARY CONDITION AT THE MODAL ANGLES OF THE HIGHER-ORDER MODES IN A 9.6λ -WIDE PARALLEL-PLATE WAVEGUIDE CAVITY

Approx. modal angle of higher-order modes (deg)	Approx. reflection coefficient (percent)
47	3
51	5
56	8
62	10
70	25
82	50

GRE approach, the rays are launched from the aperture and traced to S_{T_1} , where they form the *incident* field. The rays are then traced beyond S_{T_1} to the termination where they are scattered back to S_{T_1} to form the termination *scattered* field. Both the *incident* and *scattered* fields are converted into modal fields before they are used in the reciprocity integral to obtain the cavity scattered fields. It is clear from Figs. 4 and 5 that the GRE solutions agree very well with the reference and hybrid solutions for θ up to about 15° . This agreement suggests that the diffracted fields from the termination are negligible for small θ . Beyond that, the GRE solutions show significant deviations from the reference solutions at certain angles. From these results, it is envisaged that for a complex termination, the hybrid GRE-FDTD method will produce far more accurate results than the purely GRE approach which does not account for the termination diffracted fields.

Figure 6 shows the resultant RCS patterns for the TM_z case when the rectangular plug termination is replaced by a wedge-shaped plug termination. The height and base width of the wedge-shaped plug are 2λ and 4λ , respectively. The wedge is modeled in the FDTD code with the electric field E_z tangent to the wedge surface. The GRE-FDTD pattern is again in excellent agreement with the modal-MM pattern.

Figure 7 shows the RCS patterns of the wedge-terminated cavity for the TE_z case. The wedge is now modeled in the FDTD code with the magnetic field H_z tangent to the wedge surface. In contrast to the TM_z case where the tangential electric field E_z vanishes on the wedge surface, the tangential magnetic field H_z for the TE_z case does not vanish. Instead, it has to be specially treated. Specifically, we apply Stoke's theorem to one of Maxwell's curl equations to obtain a difference equation for updating the tangential H_z correctly. Applying Stoke's theorem to Maxwell's curl- E equation results in

$$\oint_{ABC} E \cdot dI = -\mu_0 \int_{\Delta ABC} \frac{\partial H}{\partial I} \cdot \hat{z} ds, \quad (9)$$

where the line and surface integrals are taken around the closed loop ABC and the triangle ABC , respectively, as shown in Fig. 3. After integration and rearrangement, (9)

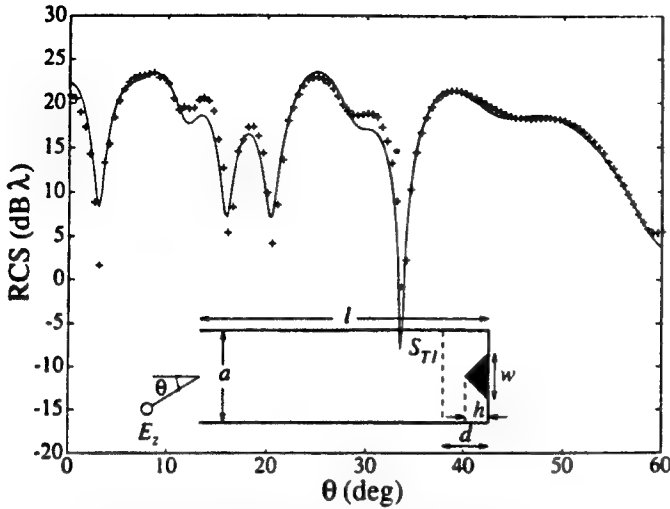


Fig. 6. Radar cross-section patterns of parallel-plate cavity with a wedge-shaped PEC plug termination using the hybrid modal-MM and GRE-FDTD methods. $a = 9.6\lambda$, $l = 30\lambda$, $d = 4\lambda$, $h = 2\lambda$, $w = 4\lambda$; TM_z: —, modal-MM; + + +, GRE-FDTD (three subapertures).

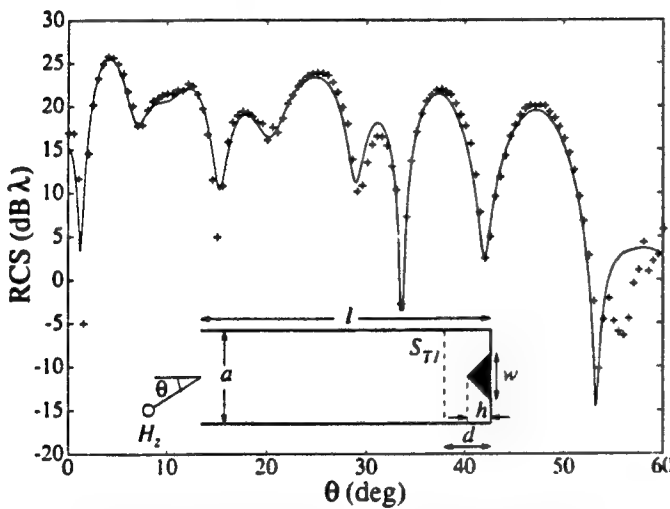


Fig. 7. Radar cross-section patterns of parallel-plate cavity with a wedge-shaped PEC plug termination using the hybrid modal-MM and GRE-FDTD methods. $a = 9.6\lambda$, $l = 30\lambda$, $d = 4\lambda$, $h = 2\lambda$, $w = 4\lambda$; TE_z: —, modal-MM; + + +, GRE-FDTD (three subapertures).

becomes

$$\begin{aligned}
 H_z^{n+1}(i_m, j_n) &= H_z^n(i_m, j_n) \\
 &+ \frac{\Delta t}{\mu_0 \Delta y} \left[E_x^{n+1/2} \left(i_m, j_n + \frac{1}{2} \right) \right. \\
 &\quad \left. - E_x^{n+1/2} \left(i_m, j_n - \frac{1}{2} \right) \right] \\
 &- \frac{\Delta t}{\mu_0 \Delta x} \left[E_y^{n+1/2} \left(i_m + \frac{1}{2}, j_n \right) \right. \\
 &\quad \left. - E_y^{n+1/2} \left(i_m - \frac{1}{2}, j_n \right) \right] + \text{CF}, \quad (10)
 \end{aligned}$$

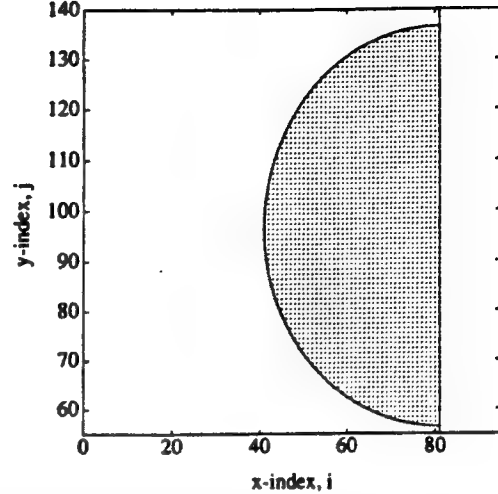


Fig. 8. Geometry of semicircular plug of radius 2λ for the TM_z case: ●, FDTD node where E_z is on or within the plug and thus set to zero; —, outline of surface of plug.

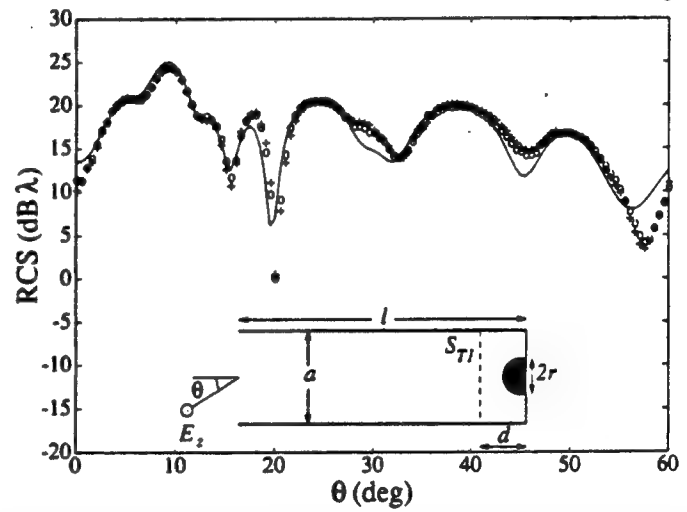


Fig. 9. Radar cross-section patterns of parallel-plate cavity with a semicircular-shaped PEC plug termination using the hybrid modal-MM and GRE-FDTD methods. $a = 9.6\lambda$, $l = 30\lambda$, $d = 4\lambda$, $r = 2\lambda$; TM_z: —, modal-MM; + + +, GRE-FDTD ($\lambda/20$); ○○○, GRE-FDTD ($\lambda/40$) (three subapertures).

where the correction factor CF is given by

$$\begin{aligned}
 \text{CF} &= \frac{\Delta t}{\mu_0 \Delta y} \left[E_x^{n+1/2} \left(i_m, j_n + \frac{1}{2} \right) - E_x^{n+1/2} \left(i_m, j_n - \frac{1}{2} \right) \right] \\
 &\quad - \frac{\Delta t}{\mu_0 \Delta x} \left[E_y^{n+1/2} \left(i_m + \frac{1}{2}, j_n \right) \right. \\
 &\quad \left. - E_y^{n+1/2} \left(i_m - \frac{1}{2}, j_n \right) \right]. \quad (11)
 \end{aligned}$$

Notice that without CF, (10) is just the regular FDTD equation for updating H_z . Therefore, CF adjusts for the

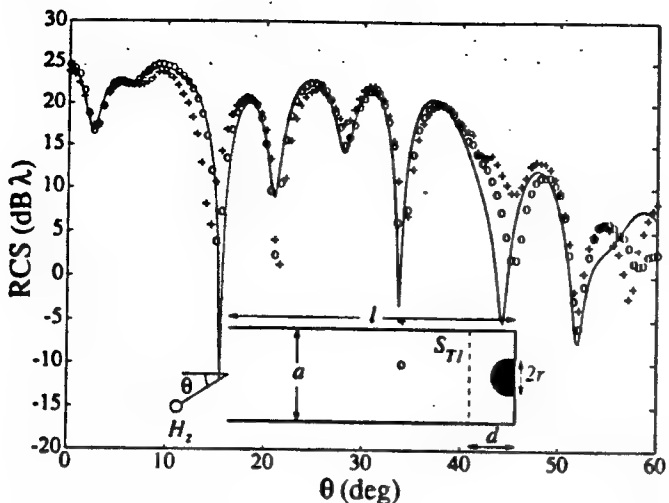


Fig. 10. Radar cross-section patterns of parallel-plate cavity with a semicircular-shaped PEC plug termination using the hybrid modal-MM and GRE-FDTD methods. $a = 9.6\lambda$, $l = 30\lambda$, $d = 4\lambda$, $r = 2\lambda$; TE_z : —, modal-MM: + + +, GRE-FDTD ($\lambda/20$); ○○○, GRE-FDTD ($\lambda/40$) (three subapertures).

H_2 's that are tangent to the wedge surface. Once again, the GRE-FDTD pattern in Fig. 7 shows excellent agreement with the modal-MM pattern except for large θ .

For the final example, a PEC semicircular plug of radius 2λ is substituted for the wedge-shaped plug. The curved surface of the semicircular plug is modeled using its stair-stepped approximation as shown in Fig. 8 for the TM_z case. A similar approximation of the semicircular plug is used for the TE_z case. The RCS patterns of the new cavity are shown in Figs. 9 and 10 for the TM_z and TE_z cases, respectively. In these figures, we have also plotted the patterns obtained with the smaller $\lambda/40$ FDTD grid. The patterns obtained with the $\lambda/20$ grid show some semblance to the reference patterns, while those obtained with the finer grid show better agreement with the reference patterns, particularly for the TE_z case. The significant improvement in the latter case is attributed to the fact that in 2D geometries, TE_z modes suffer dispersion due to the stair-stepped approximation, while TM_z modes does not [25]. This dispersion (or numerical error) reduces when a finer FDTD grid is used. Therefore, the pattern for the TE_z case shows marked improvement, while that of the TM_z case is basically unchanged.

IV. SUMMARY

In this paper, we have introduced a hybrid method which combines ray methods with FDTD. The use of the hybrid method allows us to overcome the deficiencies of a single method. The FDTD calculation, which is computationally intensive, is limited to a small region around the termination. The ray solution is used to evaluate the fields in the remainder of the cavity where it is assumed that the geometry is simple enough for high-frequency approximations to be valid. Results have been presented and com-

pared to a hybrid modal-MM solution to demonstrate its accuracy. From these results, it is evident that the hybrid ray-FDTD method shows great potential for eventually providing an accurate solution for the electromagnetic scattering from a realistic three-dimensional jet engine.

ACKNOWLEDGMENTS

We wish to thank Dr. Ri-Chee Chou and Dr. Bob Burkholder for their advice during the course of this research. Also, we wish to thank the reviewers for providing some very useful suggestions for this paper.

REFERENCES

- [1] R.-C. Chou, *Reduction of the radar cross section of arbitrarily shaped cavity structures*, Ph.D. dissertation, University of Illinois, Urbana-Champaign, IL, 1987.
- [2] R. J. Burkholder, *High-frequency asymptotic methods for analyzing the EM scattering by open-ended waveguide cavities*, Ph.D. dissertation, The Ohio State University, Columbus, OH, 1989.
- [3] R. F. Harrington, *Field Computation by Moment Methods*, New York: MacMillan Co., 1968.
- [4] E. B. Becker, G. F. Carey, and J. T. Oden, *Finite Elements, An Introduction*, vol. I, Englewood Cliffs, NJ: Prentice-Hall, 1981.
- [5] K. S. Yee, "Numerical solution of initial boundary value problems involving Maxwell's equations in isotropic media," *IEEE Trans. Antennas Propagat.*, vol. AP-14, pp. 302-307, May 1966.
- [6] A. Taflove and M. E. Brodwin, "Numerical solution of steady-state electromagnetic scattering problems using the time-dependent Maxwell's equations," *IEEE Trans. Microwave Theory Tech.*, vol. MTT-23, pp. 623-630, Aug. 1975.
- [7] H. Ling, S. W. Lee, and R.-C. Chou, "Shooting and bouncing rays: Calculating the RCS of an arbitrarily shaped cavity," *IEEE Trans. Antennas Propagat.*, vol. 37, pp. 194-205, Feb. 1989.
- [8] —, "High-frequency RCS of open cavities with rectangular and circular cross sections," *IEEE Trans. Antennas Propagat.*, vol. 37, pp. 648-654, May 1989.
- [9] R. J. Burkholder, R.-C. Chou, and P. H. Pathak, "Two ray shooting methods for computing the EM scattering by large open-ended cavities," *Comp. Phys. Commun.*, vol. 68, pp. 353-365, 1991.
- [10] R. J. Burkholder, C. W. Chuang, and P. H. Pathak, *Electromagnetic fields backscattered from an S-shaped inlet cavity with an absorber coating on its inner walls*, Final Report no. 715723-2, ElectroScience Laboratory, The Ohio State University, prepared under grant NAG3-476, for NASA/Lewis Research Center, Cleveland, OH, July 30, 1987.
- [11] J. Baldauf, S. W. Lee, L. in, S.-K. Jeng, S. M. Scarbourough, and C. L. Yu, "High frequency scattering from trihedral corner reflectors and other benchmark targets: SBR versus experiment," *IEEE Trans. Antennas Propagat.*, vol. 39, pp. 1345-1351, Sept. 1991.
- [12] S. W. Lee and R.-C. Chou, "A versatile reflector antenna pattern computation method: Shooting and bouncing rays," *Microwave Opt. Tech. Lett.*, vol. 1, no. 3, pp. 81-87, May 1988.
- [13] R.-C. Chou, T. T. Chia, and R. Lee, "The energy flow inside a waveguide cavity using the SBR and GRE methods," presented at the IEEE AP-S International Symposium, URSI Radio Science Meeting and Nuclear EMP Meeting, Chicago, IL, July 18-25, 1992.
- [14] S. W. Lee, H. Ling, and R.-C. Chou, "Ray-tube integration in shooting and bouncing ray method," *Microwave Opt. Tech. Lett.*, vol. 1, no. 8, pp. 286-289, Oct. 1988.
- [15] G. A. Deschamps, "Ray techniques in electromagnetics," *Proc. IEEE*, vol. 60, pp. 1022-1035, Sept. 1972.
- [16] R. Holland, "Finite-difference solution of Maxwell's equations in generalized nonorthogonal coordinates," *IEEE Trans. Nucl. Sci.*, vol. NS-30, pp. 4589-4591, Dec. 1983.
- [17] K. S. Yee, J. S. Chen, and A. H. Chang, "Conformal finite difference time domain (FDTD) with overlapping grids," *IEEE Trans. Antennas Propagat.*, vol. 40, pp. 1068-1075, April 1992.

- [18] A. Taflove, "Application of the finite-difference time-domain method to sinusoidal steady-state electromagnetic-penetration problems," *IEEE Trans. Electromag. Compat.*, vol. EMC-22, pp. 191-202, Aug. 1980.
- [19] R. L. Higdon, "Absorbing boundary conditions for difference approximations to the multi-dimensional wave equation," *Math. Comp.*, vol. 47, no. 176, pp. 437-459, Oct. 1986.
- [20] ___, "Numerical absorbing boundary conditions for the wave equation," *Math. Comp.*, vol. 49, no. 179, pp. 65-90, July 1987.
- [21] G. Mur, "Absorbing boundary conditions for the finite-difference approximation of the time-domain electromagnetic-field equations," *IEEE Trans. Electromag. Compat.*, vol. EMC-23, pp. 377-382, Nov. 1981.
- [22] P. H. Pathak and R. J. Burkholder, "A reciprocity formulation for the EM scattering by an obstacle within a large open cavity," *IEEE Trans. Microwave Theory Tech.*, vol. MTT-41, pp. 702-707, April 1993.
- [23] C. W. Chuang, P. H. Pathak, and R. J. Burkholder, A hybrid asymptotic modal-moment method analysis of the EM scattering by 2-D open-ended linearly tapered waveguide cavities, Technical Report No. 312436-1, ElectroScience Laboratory, The Ohio State University, prepared for McDonnell Douglas Corporation, St. Louis, MO, Dec. 1988.
- [24] J. Fang, Time-domain finite difference computation for Maxwell's equations, Ph.D. dissertation, University of California, Berkeley, 1989.
- [25] A. C. Cangellaris and D. B. Wright, "Analysis of the numerical error caused by the stair-stepped approximation of a conducting boundary in FD-TD simulations of electromagnetic phenomena," *IEEE Trans. Antennas Propagat.*, vol. 39, pp. 1518-1525, Oct. 1991.



Tse-Tong Chia (S'91) was born in Singapore on March 6, 1961. He received the B.Eng. degree with first class honors from the National University of Singapore, Singapore, in 1986, and the M.S. degree from The Ohio State University, Columbus, Ohio in 1991, all in electrical engineering. Between 1986 and 1989 he was with the Defence Science Organization of the Ministry of Defence, Singapore. He is currently pursuing his Ph.D. at The Ohio State University.

Robert Lee received his BSEE in 1983 from Lehigh University in Bethlehem, PA and his MSEE and Ph.D. in 1988 and 1990, respectively, from the University of Arizona, Tucson. From 1983 to 1984, he worked for Microwave Semiconductor Corporation in Somerset, NJ. From 1984 to 1986, he worked at Hughes Aircraft Company in Tucson, AZ. From 1986 to 1990, he was a research assistant at the University of Arizona. In addition, during the summers of 1987 through 1989, he worked at Sandia National Laboratories in Albuquerque, NM. He is currently an assistant professor at The Ohio State University. His major research interests are in the solution of electromagnetic problems using both differential-based and integral-based techniques.

ON THE CHOICE OF METRONS IN THE MEI METHOD

J. Jevtić and R. Lee
ElectroScience Laboratory
Department of Electrical Engineering
The Ohio State University
Columbus, OH, USA

I. Introduction

Finite element and finite difference methods find increasing application to the numerical analysis of problems involving unbounded solution domains. These problems require special techniques for boundary truncation. A new way to truncate the boundary has been presented in [1] through the use of the measured equations of invariance (MEI). Some of the theoretical aspects and modifications of the MEI method, as well as several examples of its practical implementation, have been reported in the articles [2-6].

We shall present our findings and the fundamentals of the method using the example of the two dimensional electromagnetic wave scattering by a perfectly conducting cylinder. We shall assume TM polarization, as shown in Figure 1. A general linear boundary condition can be expressed in the form:

$$\sum_{i=1}^M \alpha_i E_{z_i}^s = 0 \quad (1)$$

where $E_{z_i}^s$ stands for the scattered field at node i , and M is the number of nodes coupled through this equation.

What is specific to MEI method is how the coefficients α_i are chosen. Namely, one uses the fact that:

$$E_{z_i}^s = \int_{\partial S_c} G_i(s) J_s(s) ds, \quad 0 < s < 1 \quad (2)$$

where s is the normalized coordinate along the conductor surface, $J_s(s)$ is the surface current induced on the cylinder and $G_i(s)$ is the Green's function from point s on the cylinder to node i . One now chooses coefficients α_i such that (1) is exactly satisfied for several different surface currents $M_j(s)$, called metrons:

$$\sum_{i=1}^M \alpha_i \int_{\partial S_c} G_i(s) M_j(s) ds = 0, \quad j = 2, \dots, M \quad (3)$$

We need $M - 1$ metrons since one of the MEI coefficients α_i is arbitrary due to the homogeneous nature of (1).

II. Null Field and Its Minimization

We have shown in [2] that, although (1) is exactly satisfied for metrons $M_j(s)$, $j = 2, \dots, M$, the left-hand side of (1) is not equal to zero for all possible currents $J_s(s)$. We should rather write:

$$\sum_{i=1}^M \alpha_i E_{z_i}^s = R \quad (4)$$

where R is the residual. Indeed, by using (2), (1) becomes:

$$\int_{\partial S_c} E_{null}(s) J_s(s) ds = R \quad (5)$$

where:

$$E_{null}(s) = \sum_{i=1}^M \alpha_i G_i(s) \quad (6)$$

We have introduced the quantity E_{null} in [2]. We call it "the null field" since it physically represents the incident field on the conductor surface due to M line sources of strengths α_i placed at corresponding nodes and because E_{null} should preferably be zero if (1) is to be true for all possible currents $J_s(s)$.

Namely, if (1) is to be an accurate approximation of (4), the MEI coefficients should be chosen so that R in (5) is as small as possible for all possible currents. One solution has been proposed in [2] where we have minimized the null field in the least square sense:

$$\int_{\partial S_c} |E_{null}(s)|^2 ds = \min \quad (7)$$

Using (6), this condition yields:

$$\sum_{i=1}^M \alpha_i \int_{\partial S_c} G_i(s) G_j(s)^* ds = 0, \quad j = 2, \dots, M \quad (8)$$

A comparison with (3) reveals that this is the same result as would be obtained by using the conjugate of Green's functions as metrons:

$$M_j(s) = G_j(s)^*. \quad j = 2, \dots, M \quad (9)$$

III. Spectral Approach to Null Field Minimization

Condition (7) minimizes residual R in (5) for all possible currents $J_s(s)$. This would be the optimum choice if we knew absolutely nothing about the actual current induced on the cylinder. In terms of the spectral representation:

$$J_s(s) = \sum_{n=-\infty}^{+\infty} J_{sn} e^{j2\pi ns}, \quad 0 < s < 1 \quad (10)$$

this assumption would mean that (7) is the optimum choice when all components of the Fourier expansion in (10) are present in the actual current.

However, this is not the case in general, since spectral components of J_s , whose spatial variations are much faster than that of the incident wave are usually negligible. It may therefore be possible to devise a less stringent condition than that in (7) and obtain coefficients that would be more suitable for a particular problem.

This can be done as follows. Introduce Fourier expansions of Green's functions and null field:

$$G_s(s) = \sum_{n=-\infty}^{+\infty} G_{in} e^{j2\pi ns}, \quad (11)$$

and:

$$E_{null}(s) = \sum_{n=-\infty}^{+\infty} E_{nulln} e^{j2\pi ns} \quad (12)$$

Equivalents of the equations (5) and (6) in the spectral representation are then:

$$\sum_{n=-\infty}^{+\infty} E_{nulln} J_{s(-n)} = R \quad (13)$$

and:

$$E_{nulln} = \sum_{i=1}^M \alpha_i G_{in} \quad (14)$$

Assuming that an estimate of the magnitudes of the spectral components of current is available, minimization of the residual R in (13) in the least square sense would be:

$$\sum_{n=-\infty}^{+\infty} |E_{nulln}|^2 |J_{s(-n)}|^2 = \min \quad (15)$$

which is the required substitute for (7).

If we actually perform this minimization through the use of (14), we obtain:

$$\sum_{i=1}^M \alpha_i \sum_{n=-\infty}^{+\infty} G_{in} G_{jn}^* |J_{s_{(-n)}}|^2 = 0, \quad j = 2, \dots, M \quad (16)$$

and with use of (11)

$$\sum_{i=1}^M \alpha_i \int_{\partial S_c} G_i(s) \sum_{n=-\infty}^{+\infty} G_{jn}^* |J_{s_{(-n)}}|^2 e^{-j2\pi ns} ds = 0, \quad j = 2, \dots, M \quad (17)$$

Comparison with (3) reveals that this is the same result as if the metrons defined by:

$$M_j(s) = \left(\sum_{n=-\infty}^{+\infty} G_{jn} |J_{s_{(-n)}}|^2 e^{j2\pi ns} \right)^*, \quad j = 2, \dots, M \quad (18)$$

were used to find the coefficients.

It is interesting to note that if $|J_{sn}| = 1$ for all n , indicating the presence of all spectral components, (18) reduces to (9) as might be expected.

On the other hand, if $|J_{sn}| = 1$ for $|n| < N$ and $|J_{sn}| = 0$ otherwise, indicating that high spatial-frequency components are negligible, (18) gives exactly the same results as if sinusoidal metrons up to N^{th} order were used:

$$M_n(s) = e^{j2\pi ns}, \quad n = -N, \dots, N \quad (19)$$

and the overspecified system of equations for coefficients (3) was solved using the least square method.

IV. Numerical Results

We have encountered three different types of metrons in the preceding analysis. Sinusoidal metrons (19), g^* metrons (9), and optimized metrons (18). When implementing optimized metrons it is more computationally efficient to use (16) instead of (18).

The results that are presented in this section are obtained using a finite difference mesh that has been truncated two cells from the conductor surface. Six nodes are coupled through (1), and therefore $M = 6$ as shown in Figure 1. Nodal density was chosen to be 20 nodes per wavelength and all integrations were performed using ten integration points per cell.

Results in Figures 2 and 3 were obtained for the case of a circular cylinder whose diameter is 10 wavelengths. Figure 2 is a plot of the absolute error in the solution for surface current density J_s , when different metrons are used. Sinusoidal metrons for $N=2$ give

slightly better solution than g^* metrons. The best results are obtained with the use of optimized metrons.

When implementing (16), we have estimated the magnitude of the current spectrum $|\mathbf{J}_{\text{sp}}|$ by using the physical optics solution. The actual spectrum of the current is shown in Figure 3. This figure also shows the spectrum of the null field for all three types of metrons. The spectrum of the null field corresponding to g^* metrons is very large in the frequency domain of interest, although it is minimal when considered over the whole frequency range. On the other hand, the null field spectrum of the optimized metrons is minimal exactly over the frequency range that is most important.

We might expect that the g^* metrons will give better results than the same number of sinusoidal metrons when the current contains strong high frequency components. Figure 4 shows the error in the solution for a rectangular cylinder with a high aspect ratio (5λ by 0.1λ). Forty sinusoidal metrons were necessary to achieve the same accuracy as with the $5g^*$ metrons.

V. References

- [1] K. K. Mei, R. Pous, Z. Chen, Y. W. Liu, "The measured equation of invariance: A new concept in field computation," Joint IEEE AP-S International Symposium and URSI Radio Science Meeting, Chicago, IL, July, 1992.
- [2] J. O. Jevtic and R. Lee, "A theoretical and numerical analysis of the measured equations of invariance," accepted to *IEEE Trans. Antennas and Propagat.*
- [3] A. C. Cangellaris and D. B. Wright, "Application of the Measured Equation of Invariance to Electromagnetic Scattering by Penetrable Bodies," *IEEE Trans. Magnetics*, vol. 29, no. 2, pp. 1628-1631, March, 1993.
- [4] Y. Li, Z. J. Cendes, X. Yuan, "A modified MEI method for solving scattering problems with the finite element method," Joint IEEE AP-S International Symposium and URSI Radio Science Meeting, Ann Arbor, MI, June, 1993.
- [5] R. Janaswamy, "Application of the measured equation of invariance to wave propagation over irregular, inhomogeneous terrain," Naval Postgraduate School, Monterey, CA, report NPS-EC-93018, October, 1993.
- [6] J. L. Young, J. B. Schneider, R. G. Olsen, "The measured equation of invariance and its analytical foundation," Joint IEEE AP-S International Symposium and URSI Radio Science Meeting, Ann Arbor, MI, June, 1993.

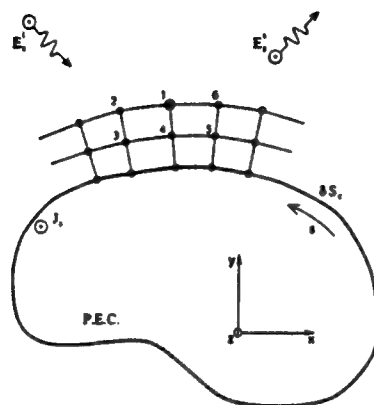


Figure 1. Geometry for a PEC cylinder illuminated with a TM polarized plane wave.

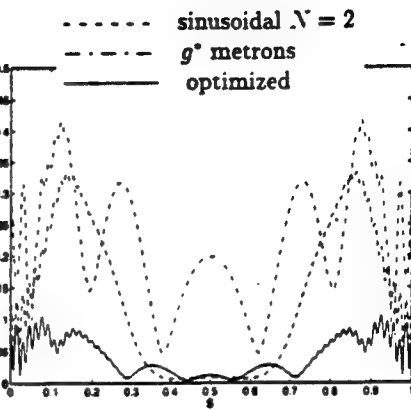


Figure 2. Plot of the error in the surface current on circular cylinder of diameter 10λ . Sinusoidal, g^* and optimized metrons are compared. Wave is incident normally at the point $s = 0.5$.

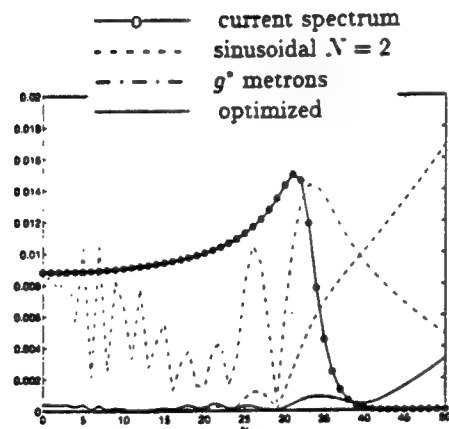


Figure 3. Plot of the spectra of null fields corresponding to three different sets of metrons for the case shown in Figure 2. The normalized spectrum of the surface current is shown for reference.

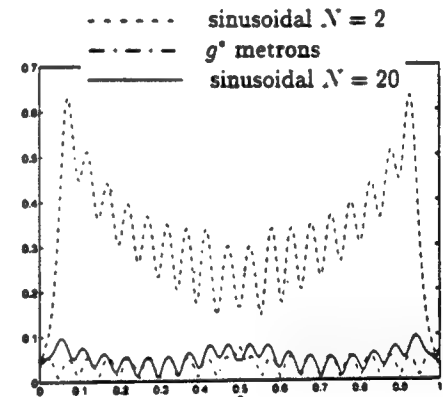


Figure 4. Plot of the error in the surface current on the rectangular cylinder 5λ by 0.1λ . Wave is incident normally to the shorter side. Sinusoidal metrons with $N = 2$ and 20 are compared with the g^* metrons.

A Theoretical and Numerical Analysis of the Measured Equation of Invariance

Jovan O. Jevi \acute{c} , *Student Member, IEEE*, and Robert Lee, *Member, IEEE*

Abstract— The measured equation of invariance (MEI) has been recently introduced to efficiently and accurately handle the boundary truncation for finite methods. In this paper, we present a theoretical analysis that provides several important insights into the capabilities of the MEI. From the numerical study, we can explain why the MEI works better than one would expect. Both the theoretical and the numerical analysis demonstrate that the accuracy of the solution is dependent on the electrical size of the geometry as well as the distance between the mesh boundary and the geometry. From the analysis, we propose a new set of metrons that is less sensitive to the excitation than the previously proposed sinusoidal metrons.

I. INTRODUCTION

THE finite element method (FEM) has always been handicapped in the modeling of electromagnetic phenomena because of its inability to both accurately and efficiently simulate the radiation condition. In the past 25 years, researchers have developed numerous boundary conditions to model the radiation condition. The work can be separated into two classes of methods, local and global. In the local methods [1]–[5], a finite difference (FD) equation is derived for the boundary based on an approximate assumption of the behavior of the field. Usually, the wave is assumed to be outgoing from the computation domain in a direction perpendicular to the boundary. In addition, the FD equations are derived without any consideration of the geometry of interest. The major advantages of the local methods are that they maintain the sparsity of the FEM matrix and that they are easily implemented into an FEM code. The major disadvantage is that they may give inaccurate results when the mesh boundary is placed close to the geometry. To assure an accurate solution, the boundary must be extended a large distance from the geometry, which may dramatically increase both the computation time and the storage requirements. The choice of where to place the boundary is also not clear. Currently, the only way to determine the correct placement of the boundary for complex geometries is empirical. The minimum distance between the scatterer and the grid boundary is dependent upon the geometry, the characteristics of the excitation, and the degree of accuracy desired; so, in principle, numerical tests must be run for each new geometry.

Manuscript received June 1, 1993; revised April 5, 1994. This work was supported by the NSF under Grant ECS-9111266 and the Joint Services Electronics Program under Contract N00014-89-J-1007.

The authors are with the ElectroScience Laboratory, Department of Electrical Engineering, The Ohio State University, Columbus, OH 43212 USA.

IEEE Log Number 9403659.

The global methods are based on a rigorous formulation in which all the nodes on the boundary are coupled together; therefore, an accurate solution can be obtained without regard to the distance between the geometry and the mesh boundary. In some methods [6], [7], the equations that couple the boundary nodes are placed directly in the FEM matrix. However, this has the effect of reducing the sparsity of the matrix, which can result in a significant increase in computation costs. In other global methods [8], [9], the boundary equations are decoupled from the rest of the FEM matrix. Although these methods are usually more efficient than those in [6] and [7], they still require the solution of a dense matrix due to the fully coupled boundary equations. In addition, the computation time required to decouple the boundary equations from the FEM matrix is comparable to the solution time of the FEM matrix without the boundary equations.

Recently, the measured equation of invariance (MEI) [10] has been proposed as a rigorous local method for modeling perfectly conducting cylinders. It is based on the concept that accurate local FD equations can be written at the boundary nodes if the geometry information can somehow be incorporated into the equations. Thus, a general FD equation is used at the boundary where the coefficients in the FD equations are unknown. These coefficients are then determined by the use of a sequence of fields called *measures*. A more detailed discussion of this procedure is described in the next section. The MEI has also been extended to dielectric cylinders [11]. Although both groups were able to show that the MEI works well for several geometries, the method is still in its infancy, and there is very little theoretical foundation to explain why the MEI works. In this paper, we provide some theoretical insights into the MEI. We show that the MEI approach still produces an approximate boundary condition. However, because the geometry information is incorporated into the boundary condition, it is capable of producing very good results with appropriately chosen metrons. The sinusoidal metrons turn out to be very good choices for the geometry we consider, and in our numerical study we will explain the reason for this. The numerical study also demonstrates the effect of changing various parameters in the MEI.

II. THEORETICAL ANALYSIS

A. Review of the MEI

To analyze the MEI, let us consider the problem of electromagnetic scattering from a two-dimensional perfectly conducting cylinder in free space (see Fig. 1). The boundary of

the cylinder is defined to be ∂S_c . The formulation is derived only for the TM (E_z, H_x, H_y) polarization since the same procedure can be used for the TE case. The field solution is obtained from the solution of the Helmholtz equation for E_z . The grid surrounding the cylinder can either be a finite-difference or a finite-element grid. For this analysis, let us consider a finite-difference grid. At the boundary of the grid, we cannot apply the traditional finite-difference approximation because the traditional difference approximation requires grid points that are exterior to the grid. Thus we must find another finite-difference approximation that incorporates the radiation condition. The measured equation of invariance is based on the principle that a linear equation that couples the boundary nodes to the adjacent nodes can be formulated without using the traditional finite-difference approximation. One possible coupling is the six-node coupling shown in Fig. 1, where node 6 is coupled to nodes 1 through 5. To simplify the notation, the analysis is presented in terms of this coupling scheme without any loss of generality. The linear equation at node 6 can be written as

$$\sum_{i=1}^6 a_i E_{zi}^s = 0 \quad (1)$$

where E_{zi}^s is the scattered electric field at node i and a_i are constant coefficients that must be determined. To find these coefficients, Mei *et al.* [10] use three postulates in which they conjecture that the equation in (1) is

- 1) location dependent,
- 2) geometry specific, and
- 3) invariant to field excitation.

The first two postulates can be shown to be true by numerical experimentation. These two postulates are also inherently incorporated into the global methods described in the previous section. The validity of the third postulate is not as clear. If the third postulate is true, then the coefficients in (1) can be determined from the field solutions at the six nodes due to five linearly independent excitations or metrons (only five are needed since the sixth coefficient is arbitrarily specified), which are denoted by the symbol Ψ_k . The five metrons represent five linearly independent surface current density distributions on the conducting cylinder. The metrons are usually chosen to be entire domain and to vary sinusoidally over the cylinder. For example, the choice in [10] is

$$\Psi_k = \begin{cases} \cos \pi k s & k = 0, 2, 4 \\ \sin \pi (k+1)s & k = 1, 3 \end{cases} \quad (2)$$

where $0 \leq s \leq 1$ describes the perimeter of the cylinder. Although the results presented in [10] and [11] seem to indicate that the third postulate is true, there were some unexplainable discrepancies in the numerical results. The reasons for these discrepancies can be determined from an analysis of the MEI.

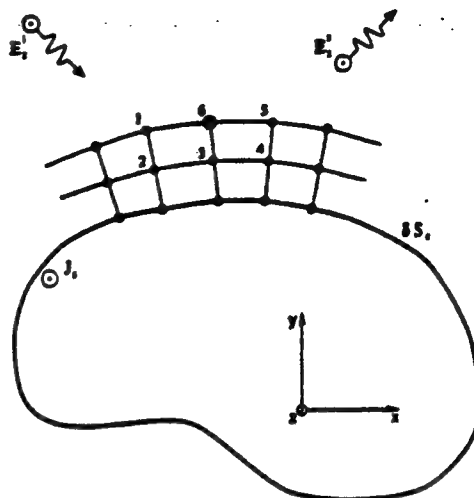


Fig. 1. Perfectly conducting cylinder geometry for analysis of the MEI.

B. Analysis of the MEI

An equation can be written relating E_{zi}^s to the induced electric surface current density J_z on the cylinder, as follows:

$$E_{zi}^s = -j\omega\mu_0 \int_{\partial S_c} g(\vec{r}_i, \vec{r}') J_z(\vec{r}') d\ell' \quad (3)$$

where \vec{r}_i is the position vector to node i and $g(\vec{r}_i, \vec{r}')$ is the free-space Green's function, which is given by

$$g(\vec{r}_i, \vec{r}') = \frac{1}{4\pi} H_0^{(2)}(k_0 |\vec{r}_i - \vec{r}'|). \quad (4)$$

The variable k_0 is the free-space wave number given by $k_0 = \omega\sqrt{\mu_0\epsilon_0}$. The above equations are for the TM polarization. For the TE polarization, the nodal unknown is the z -directed magnetic field, which is related to the electric surface current by $\hat{n} \cdot \nabla g$ where \hat{n} is the unit normal from the conductor surface. Equation (3) is substituted into (1) to obtain

$$\sum_{i=1}^6 a_i \int_{\partial S_c} g(\vec{r}_i, \vec{r}') J_z(\vec{r}') d\ell' = 0. \quad (5)$$

Recognizing the fact that $g(\vec{r}_i, \vec{r}') = g(\vec{r}', \vec{r}_i)$, we rewrite (5) as

$$\int_{\partial S_c} \left[\sum_{i=1}^6 a_i g(\vec{r}', \vec{r}_i) \right] J_z(\vec{r}') d\ell' = 0. \quad (6)$$

The term inside the brackets has a special physical significance. It represents the electric field on ∂S_c due to six line sources of weights a_i located at the corresponding nodes i . Let us define the null field denoted by E_{null} to be

$$E_{\text{null}}(\vec{r}') = \sum_{i=1}^6 a_i g(\vec{r}', \vec{r}_i) \quad \vec{r}' \in \partial S_c. \quad (7)$$

In order for the third postulate to be true, a set of coefficients a_i must be found such that (6) is true for all possible excitations, i.e., all possible $J_z(\vec{r}')$ for $\vec{r}' \in \partial S_c$. This is possible only in the instance that

$$E_{\text{null}}(\vec{r}') = 0 \quad \vec{r}' \in \partial S_c. \quad (8)$$

However, it is impossible to choose a set of coefficients a_i such that (8) is satisfied. Thus, the third postulate is incorrect. It should be noted that we use the notation E_{null} in (7) since the desired value of E_{null} is zero.

Although the third postulate is wrong, the numerical results presented in [10] indicate that the method has some merit. The procedure in which the coefficients are determined from the metrons may provide some insight into the accuracy of the MEI. To find the coefficients, we use the metrons in (2) in place of J_z in (5). The coefficients are then determined from the resulting matrix equation. With this choice of coefficients, the null field is orthogonal to any current distribution on the cylinder that can be represented by a linear combination of the metrons. Thus, any excitation of the cylinder that induces a current distribution that can be represented by a linear combination of the metrons is perfectly absorbed by the boundary condition produced from the MEI. For an arbitrary case, the current density J_z can be broken down into

$$J_z = J_{\text{met}} + J_{\text{res}} \quad (9)$$

where J_{met} is the part of the current density that can be represented by the metrons, i.e.,

$$J_{\text{met}} = \sum_{k=1}^5 c_k \Psi_k. \quad (10)$$

J_{res} is the remainder of the current that produces the error in the solution. Once the coefficients a_i have been determined, the error can be directly incorporated into the boundary equation in (1):

$$\sum_{i=1}^6 a_i E_{z,i} = R \quad (11)$$

where the residual R is defined from (6) and (7) to be

$$R = \int_{\partial S_c} E_{\text{null}}(\bar{\rho}') J_z(\bar{\rho}') d\ell'. \quad (12)$$

Since J_{met} is orthogonal to E_{null} , (12) reduces to

$$R = \int_{\partial S_c} E_{\text{null}}(\bar{\rho}') J_{\text{res}} d\ell'. \quad (13)$$

For small smooth cylinders, J_{res} is small compared to J_{met} because the current distribution can be accurately described by the metrons in (2). Even for cases where J_{res} is locally large, such as near sharp corners of conductors, R may still be a small value since the integration in (13) is performed over the entire cylinder. For cylinders that are electrically large, J_{res} may become larger than J_{met} , which may result in significant errors in the solution unless the residual R due to J_{res} is small.

C. Alternative Metrons

The metrons in (2) seem to have been chosen arbitrarily because of the assumptions of the third postulate. This was a fortunate choice, as we will see in the next section. However, with the above analysis of the MEI, it is now possible to develop a variety of different schemes for the determination of the coefficients a_i . In this section, we propose a scheme

to determine the coefficients without the use of metrons. The ideal boundary condition would be the case where coefficients can be found such that (8) is satisfied. Since this case is not possible, one choice is to find coefficients such that E_{null} is minimized in some manner. By minimizing E_{null} on ∂S_c , the residual R in (12) is minimized independent of J_z . A good method for the minimization of E_{null} is the method of least squares, in which the coefficients are chosen such that

$$\int_{\partial S_c} |E_{\text{null}}(\bar{\rho}')|^2 d\ell' = \text{Minimum.} \quad (14)$$

Substituting (7) into (14) and applying the method of least squares, we obtain the following set of equations for a_i :

$$\int_{\partial S_c} \sum_{i=1}^6 a_i g(\bar{\rho}', \bar{\rho}_i) g^*(\bar{\rho}', \bar{\rho}_j) d\ell' = 0 \quad j = 1, 2, \dots, 5 \quad (15)$$

where g^* is the conjugate of the free-space Green's function and a_6 is assumed to be specified. It is interesting to note that the determination of the coefficients from (15) is mathematically equivalent to choosing g^* as the metron. Thus, g^* can be used as an alternative set of metrons although the derivation is based on the minimization of E_{null} rather than on any concept of "measuring" the FD equations.

III. NUMERICAL STUDY

The major computation cost associated with the MEI is the integration of the metrons. The complexity of the integral evaluation is NM where N is the number of nodes on the boundary of the grid and M is the number of integration points on the cylinder surface. We can choose $M = N$ to perform the integration. However, the coefficients a_i are very sensitive to the integral evaluation, and we found that with the choice of $M = N$ (20 nodes per wavelength), the results are inaccurate when sinusoidal metrons are used and the number of layers is less than four. We were able to obtain good results all the way down to two layers with $M = 4N$. The inaccuracy is due to the singularity of the Green's function, and we expect that good results can be obtained with $M \approx N$ if unequally spaced integration points are used or if the singularity is extracted analytically. For the numerical study here, our interests are not in numerical efficiency but rather numerical accuracy; therefore, we have chosen $M = 10N$ to generate the results. The MEI is not a symmetric formulation, so the resulting finite difference matrix equation is also nonsymmetrical.

A. Initial Observations

Numerical problems that will be considered in this paper all relate to plane wave scattering from a perfectly conducting circular cylinder (see Fig. 2). This geometry is chosen because the series solution is known and also because the sinusoidal metrons are easily identified with terms in the series solution. We will always use a nodal density of 20 nodes per wavelength, two layers of nodes, and sinusoidal metrons given by (2), unless explicitly stated otherwise. It should be noted that the conclusions drawn for the numerical results are not applicable to problems in which the truncation boundary

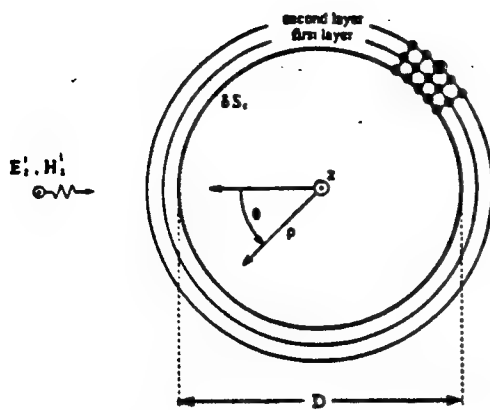


Fig. 2. Perfectly conducting circular cylinder.

is concave. Up to this point, we have been unsuccessful in modeling deep cavities with the MEI.

The application of the MEI method to small smooth cylinders should yield excellent results. This is demonstrated in Fig. 3, where the magnitude of surface current density, computed using the MEI method, is compared to the series solution for the case of a 1-wavelength diameter circular cylinder where the incident plane wave is chosen to be TE polarized. Previously, we argued that the reason for the good agreement lies in the fact that the actual current distribution can accurately be represented by a linear combination of metrons; therefore, there should be very little error since the MEI boundary equations work perfectly for the metrons. To verify this fact we require a quantitative measure of how well the MEI boundary equation absorbs field radiated by a particular current distribution. This measure is provided by the residual R , which has been introduced in (12). A smaller residual indicates a more accurate boundary condition for that current distribution on the cylinder. Let us define R_n to be the harmonic residual due to an electric current density given by $\exp(jn\phi)$. In Fig. 4, the normalized magnitude of R_n is plotted versus n for a 1-wavelength diameter cylinder. As we might expect, residuals corresponding to the zeroth-, first-, and second-order harmonics are zero, indicating perfect absorption, due to the fact that metrons given by (2) are equivalent to these three harmonics. However, it is evident from the figure that higher order current distributions result in much larger residuals. For the sake of comparison, Fig. 4 also shows the normalized magnitude of Fourier spectrum of the actual current distribution. No significant current components are present in the region where the residual attains large values. We have, therefore, verified that for small cylinders, or whenever a current distribution to be computed can be expressed as a linear combination of metrons, the MEI method yields excellent results.

But what happens if the aforementioned conditions are not met, as might be the case with larger cylinders? Fig. 5 is a plot of the magnitude of the surface current density due to a TE-polarized plane wave incident on a cylinder 10 wavelengths in diameter. The MEI and series solutions are compared, and we observe that the error is much more noticeable than in Figure 3 for the 1-wavelength diameter cylinder. However,

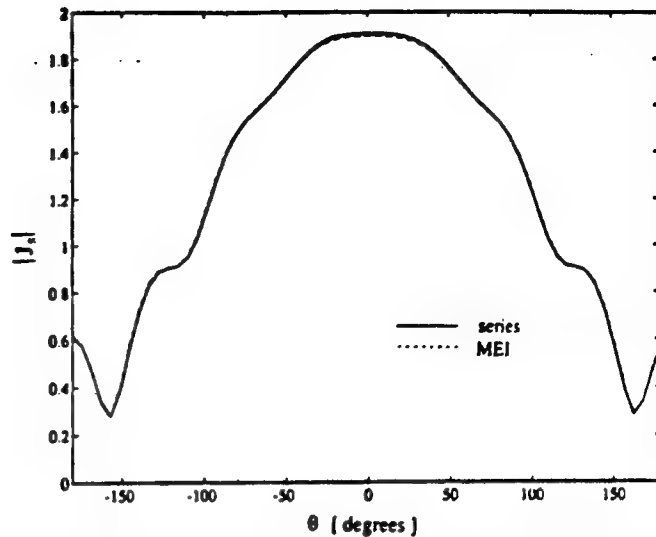


Fig. 3. Plot of the magnitude of the surface current density on a PEC circular cylinder as a function of θ ($D = 1\lambda$, $\Delta\rho = \lambda/20$, $\Delta\theta = 5.7^\circ$, 2 layers, TE polarization). The MEI solution is compared to the series solution.

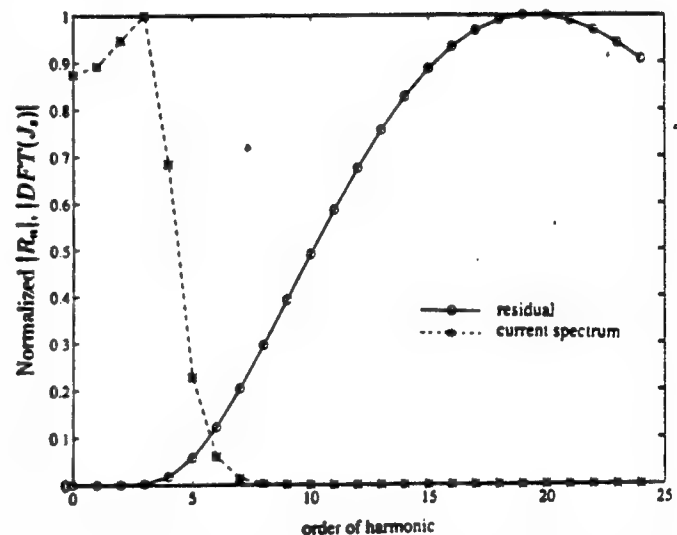


Fig. 4. Plot of the normalized value for $|R_n|$ and plot of the normalized magnitude of the Fourier spectrum of the surface current density for the case shown in Fig. 3.

the MEI solution still follows the general shape of the series solution.

A glance at the spectrum of the current distribution in Fig. 6 indicates that significant harmonic components are present up to approximately the 35th order. The metrons, which are only associated with the first three harmonics, cannot accurately represent the actual current on the cylinder, yet the results in Fig. 5 are satisfactory. Furthermore, a plot of the normalized magnitude of the residual for different harmonics in Fig. 6 reveals that the residual is practically zero for all the harmonics up to approximately the 20th order even though one would expect it to be zero only for the first three harmonics that are used as metrons. It is also evident that the residual becomes significant in the region where there are still significant spectral components of the current. This explains the deterioration in

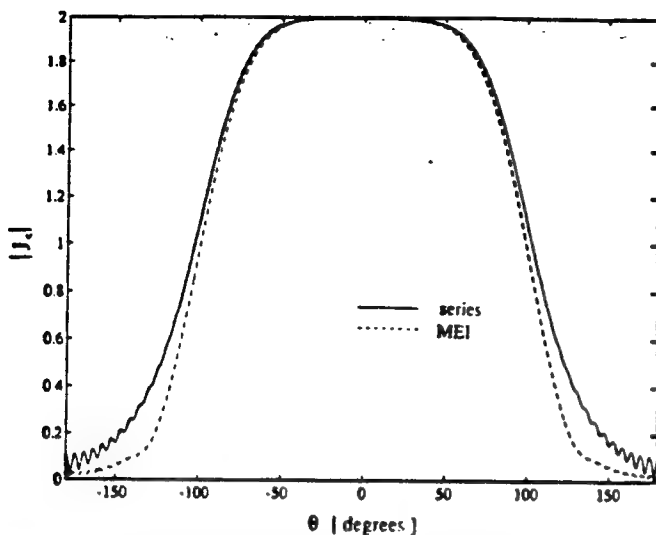


Fig. 5. Plot of the magnitude of the surface current density on a PEC circular cylinder as a function of θ ($D = 10\lambda$, $\Delta\rho = \lambda/20$, $\Delta\theta = 0.57^\circ$, 2 layers, TE polarization). The MEI solution is compared to the series solution.

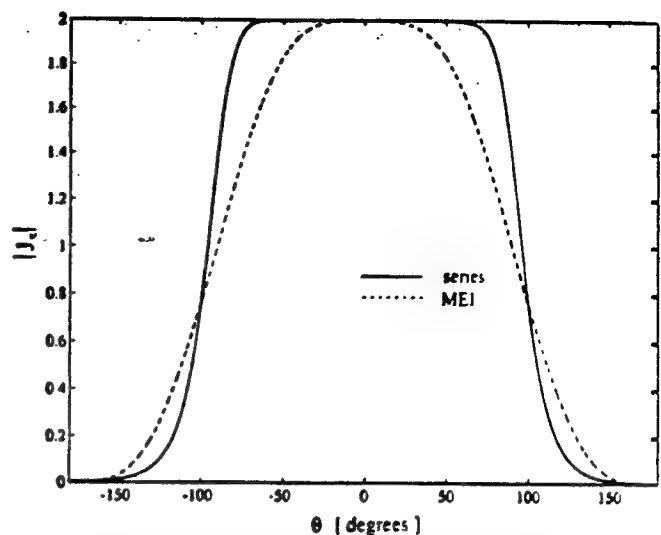


Fig. 7. Plot of the magnitude of the surface current density on a PEC circular cylinder as a function of θ ($D = 100\lambda$, $\Delta\rho = \lambda/20$, $\Delta\theta = 0.057^\circ$, 2 layers, TE polarization). The MEI solution is compared to the series solution.

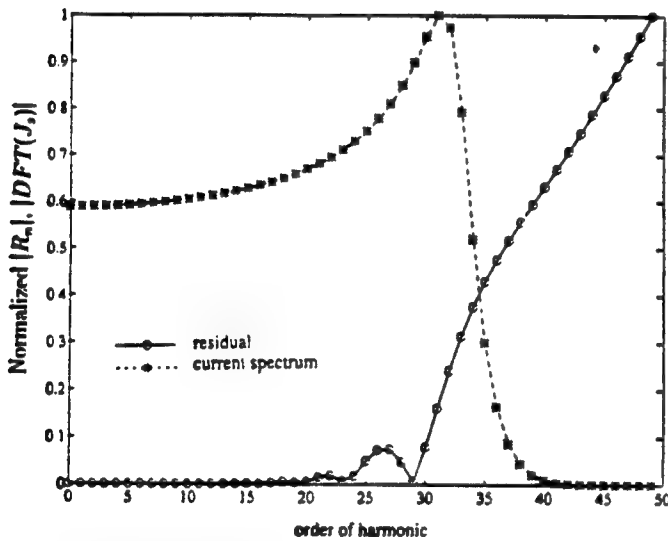


Fig. 6. Plot of the normalized value for $|R_n|$ and plot of the normalized magnitude of the Fourier spectrum of the surface current density for the case shown in Fig. 5.

accuracy when compared to the smaller problem shown in Fig. 3.

The overlap between regions of nonzero residual and nonzero current spectrum becomes even more pronounced as the size of the problem is increased. Fig. 7 is a plot of the magnitude of the surface current for a cylinder that is 100 wavelengths in diameter due to a TE-polarized plane wave. In Fig. 8, we show the normalized magnitudes of corresponding harmonic residuals and current spectrum.

Let us summarize the most important observations made thus far. First, whenever a linear combination of metrons accurately approximates the actual current distribution, the MEI method gives excellent results since the residual is zero for all spectral components of current that are of interest. Second, even if the above-mentioned conditions are

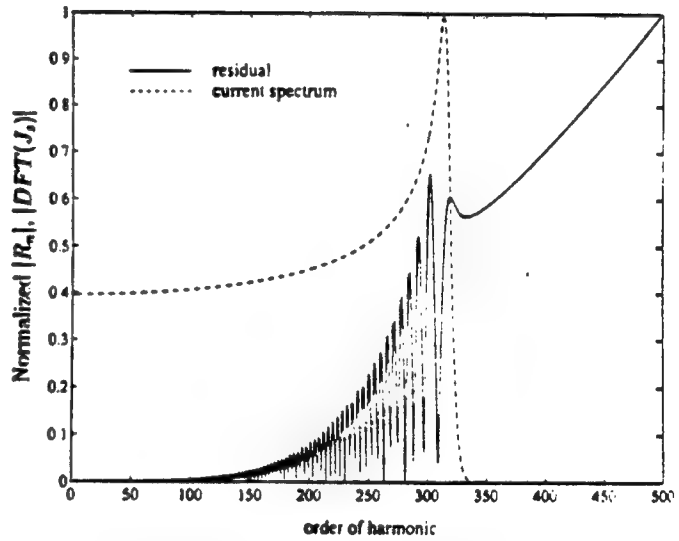


Fig. 8. Plot of the normalized value for $|R_n|$ and plot of the normalized magnitude of Fourier spectrum of surface current density for the case shown in Fig. 7.

not satisfied, the results obtained with the MEI method are very good. Although the residuals for only the first three harmonics are explicitly forced to zero, the residual is relatively small for most of the remaining harmonic components of interest. In other words, currents that are much more rapidly varying than the metrons produce fields that are readily absorbed by the boundary condition. Third, as the size of the problem is increased, the accuracy is impaired. Residuals corresponding to the most rapidly varying current components increase.

It is evident by now that the accuracy of the MEI solution can be judged by observing variations in the harmonic residuals. On the other hand, the behavior of these residuals is essentially determined by the choice of metrons. However, before we proceed into further analysis of these relationships,

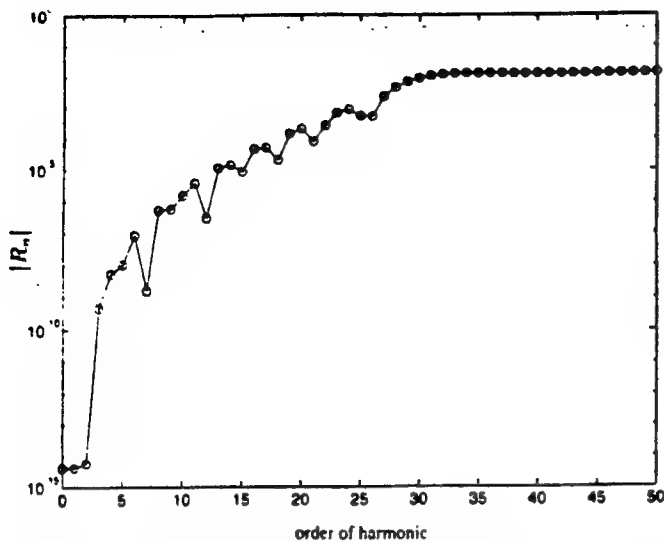


Fig. 9. Semilogarithmic plot of $|R_n|$ for a PEC circular cylinder ($D = 10\lambda$, $\Delta\rho = \lambda/20$, $\Delta\theta = 0.57^\circ$, 2 layers, TM polarization).

a numerical study of certain theoretical concepts introduced in Section II of this paper is considered.

B. Null Field

Throughout the remainder of this paper we shall be referring to results of the MEI method as applied to a 10-wavelength diameter circular cylinder illuminated with a TM-polarized plane wave. However, this is merely a workhorse for our numerical study since we have found that the conclusions hold for circular and square cylinders of various sizes.

Fig. 9 is a plot of the magnitudes of the harmonic residuals when the low order sinusoidal metrons are used to produce the MEI coefficients. A semilogarithmic scale reveals certain details not visible in the corresponding linear scale plot shown by the solid curve in Fig. 12. Only the first three harmonics, that is, only metrons, yield residuals that are exactly zero (finite numbers due to numerical roundoff). Three regions in the variation of harmonic residuals are now evident. The first region, where the residuals are exactly zero, coincides with the metrons. Within the second region, the residuals are not exactly zero, but they are insignificant for all practical purposes. The reason for the existence of this region will be explained in this and the following subsection. The fact that the MEI produces an excellent boundary condition for the harmonics in this region is the reason for its success when applied to large geometries. Finally, after a certain threshold spatial frequency, the residual abruptly increases, indicating the failure of the boundary equation to absorb fields radiated by these rapidly varying currents. The abrupt increase is not discernible on the semi-log plot, but it is very evident on the linear plot in Fig. 12. It is the overlap of this third region with the region of nonzero spectrum of the current distribution that ultimately determines the amount of error in the MEI solution.

Based on the above discussion of the behavior of the harmonic residuals, we can provide some additional insight into the theoretical concept of the null field, defined by (7). The null field is simply a linear combination of individual

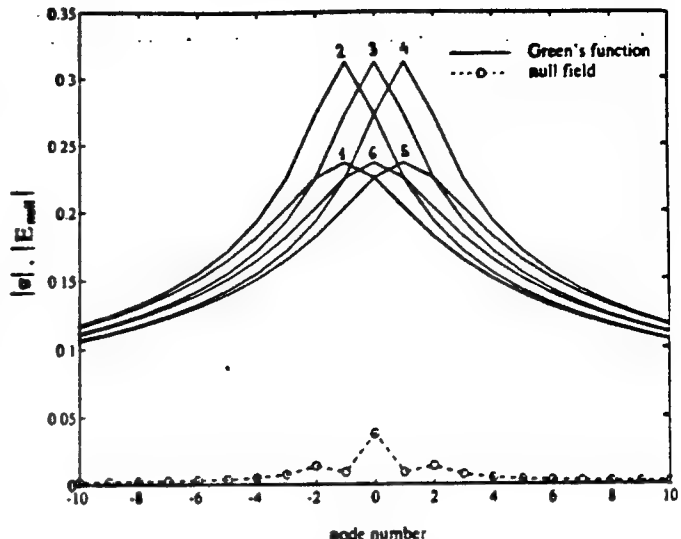


Fig. 10. Plot of the magnitudes of the Green's functions due to line source located at the six boundary nodes and plot of the magnitude of the null field for the case shown in Fig. 9.

fields radiated by unit line sources placed at all the nodes that are coupled through the MEI equation. This situation is shown in Fig. 10. The magnitudes of all six line source fields are plotted along with the magnitude of the null field that has been obtained by linearly combining these six fields through the use of the MEI coefficients. Fields are sampled along the cylinder surface. According to (14), the null field should preferably be as small as possible in order for the MEI method to be accurate. Indeed, as we can see in Fig. 10, the null field is much smaller than any of the six components. It is the purpose of the MEI coefficients to weight each one of the line source fields in such a way that they cancel each other as thoroughly as possible.

The null field bears a very close relationship to the harmonic residuals. In fact, since R_n is the residual due to n th harmonic current, it is easy to show from (12) that the R_n is the same as the n th term in the Fourier series of the null field. It is therefore possible to obtain the harmonic residuals simply by finding the Fourier spectrum of the null field. Following this direction, we show in Fig. 11 the magnitude of the Fourier spectra for the fields radiated by line sources placed at the six nodes on the mesh boundary where the MEI equations are to be applied. One thing is immediately brought to our attention. The spectra are almost identical up to approximately the 20th order, where the harmonic residuals were found to be significant. Indeed, we argue that it is exactly this property of the Green's functions emerging from nearby points, i.e., that they differ significantly only in higher spatial frequencies, which is responsible for the high accuracy of the MEI equation even when applied to currents that are much more rapidly varying than the metrons and are not expressible as the linear combination of the latter. We shall make this point clearer in the next section.

C. Parameter Study

In the MEI method, the coefficients were chosen such that the first three harmonics of the null field are zero. However,

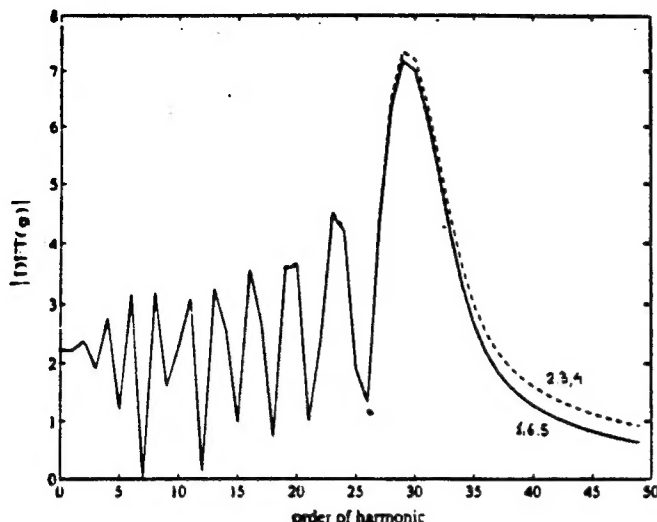


Fig. 11. Plot of the magnitudes of the Fourier spectra of six Green's functions that were shown in Fig. 10.

since the spectra of the six Green's functions are virtually identical up to the 20th harmonic, we should be able to use any arbitrary set of harmonics between 0 and 20 and obtain essentially the same coefficients. In Fig. 12 we see that this is actually the case. The null field spectra are plotted for different choices of metrons. The traditional choice of metrons, i.e., zeroth, first, and second harmonic as metrons, yields almost an identical spectrum to that obtained from the use of the zeroth, fifth, and tenth harmonics as metrons. On the other hand, the use of metrons outside the interval where Green's function spectra are identical, as for example using the zeroth, 24th, and 35th harmonic as metrons, gives radically different results that are actually better.

For the sake of comparison, Fig. 13 shows the magnitude of error in the MEI solution for the above-mentioned metron choices. It is evident that the solution is insensitive to the choice of metrons as long as they are chosen from the spatial frequency interval where the Green's function spectra do not differ much. It is also evident that a smaller residual leads to a better solution.

One obvious way to reduce residual and thereby improve the solution is to move the boundary of the mesh farther away from the cylinder. One can perform a simple analysis to show that the differences between the Green's functions due to the six line sources decrease as the boundary of the mesh is moved farther from the cylinder. Evidence of this is shown in Fig. 14, where the magnitudes of harmonic residuals are plotted for the mesh consisting of two, four, and six layers. The corresponding magnitude of the error in the current on the cylinder is shown in Fig. 15. Thus, moving the boundary farther from the scatterer reduces the residual and improves the solution.

There are other ways to improve the solution, such as selecting a suitable set of metrons. We have already seen in Fig. 13 that by choosing the zeroth, 24th, and 35th harmonics to be the metrons, we obtain better results than for the other two choices that were investigated. One way to systemize this choice is to use more metrons than unknown coefficients—in

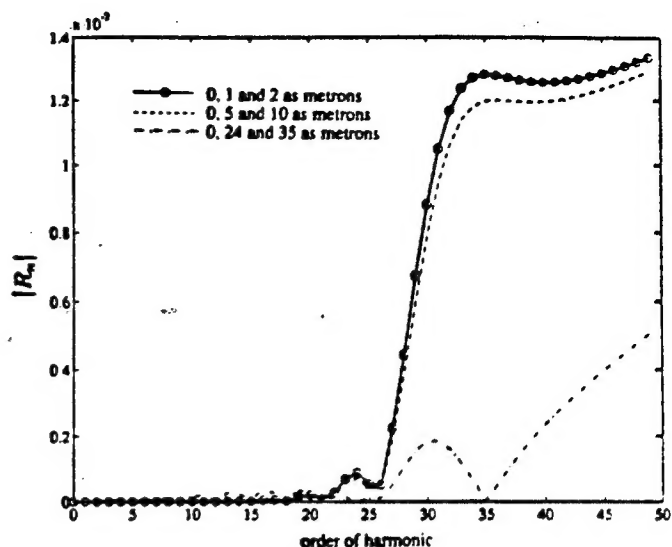


Fig. 12. Plot of $|R_n|$ for the case shown in Fig. 9, but for three different sets of metrons. Zeroth, first, and second harmonics; then the zeroth, fifth, and tenth harmonics; and finally the zeroth, 24th, and 35th harmonics were used as metrons.

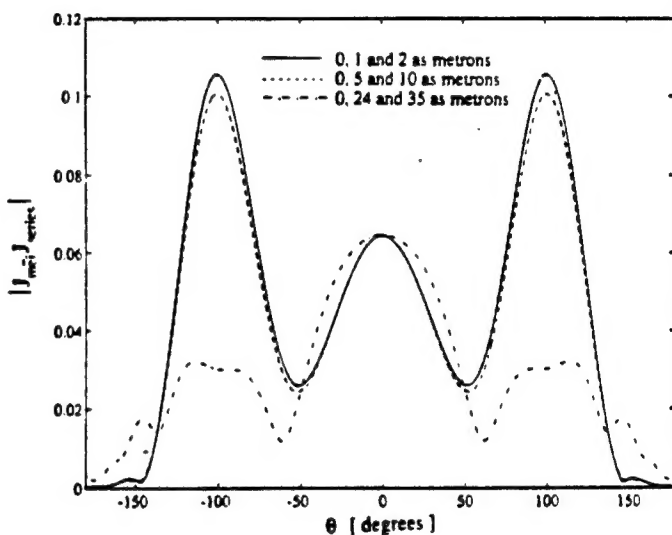


Fig. 13. Plot of the magnitude of the error in the MEI solution for the surface current density as a function of θ for the three cases shown in Fig. 12.

this case, more than five—and then to solve for the coefficients with the least square approach. Fig. 16 shows what happens with the magnitude of harmonic residuals as the number of metrons is increased from 5 to 50 and 100. In Fig. 17, we demonstrate the effect of this upon the magnitude of error in the MEI solution. It decreases with an increasing number of metrons, though the rate of decrease in the solution is not as fast as the rate of decrease in the residual.

It is natural now to ask what happens if we keep increasing the number of metrons to infinity. Would the MEI coefficients be stable and, if they are, what would they converge to? Using an infinite number of metrons intuitively corresponds to the requirement that the residual given by (13) be as small as possible for *all* possible currents. That brings us back to the argument expressed in (14), whose solution was found to be

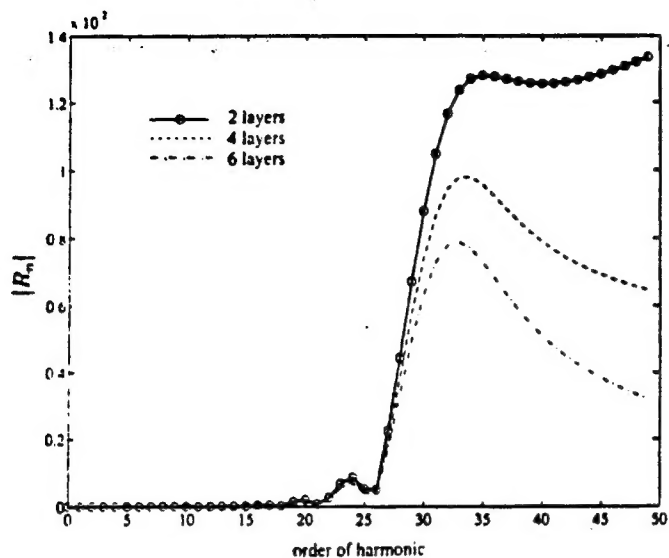


Fig. 14. Plot of $|R_n|$ for the case shown in Fig. 9, but for three different separations between the boundary of the mesh and the cylinder surface. Results for two, four, and six layers of nodes are shown.

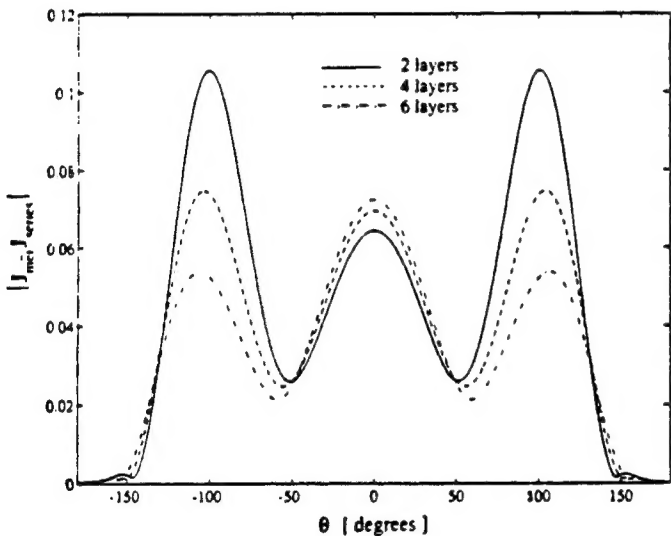


Fig. 15. Plot of the magnitude of the error in the MEI solution for the surface current density as a function of θ , for the three cases shown in Fig. 14.

(15). In other words, one could use five metrons equal to the conjugates of the Green's functions to obtain the same solution as if one were to use an infinite number of sinusoidal metrons. This is verified numerically in Table I.

Fig. 18 shows the magnitudes of the harmonic residuals corresponding to 300 sinusoidal, 500 sinusoidal, and g^* metrons. The convergence towards the g^* solution is evident.

The sinusoidal metrons usually perform either as well as or better than the g^* metrons for the cases shown here. We expect this behavior because the problem of plane wave scattering from circular cylinders results in surface currents whose spectral content is located at the lower harmonics. Since the g^* metrons optimize the coefficients for all the harmonics, the residual for the lower order harmonics are not as well minimized as for the case where the low-order sinusoidal metrons are used. It should be noted, however, that for sources and cylinder shapes that induce surface currents with a broader

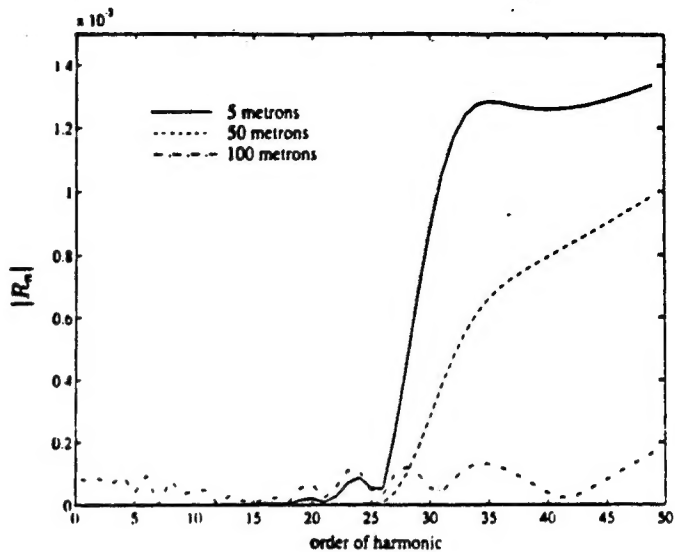


Fig. 16. Plot of $|R_n|$ for the case shown in Fig. 9, but using 5, 50, and 100 lowest order harmonics as metrons.

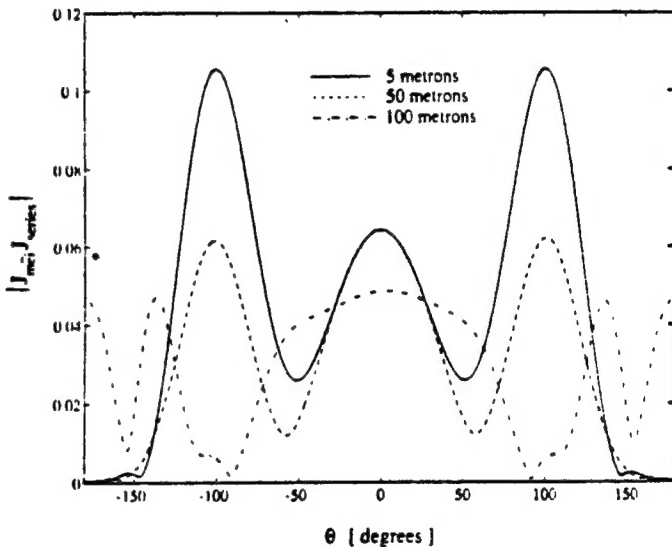


Fig. 17. Plot of the magnitude of the error in the MEI solution for the surface current density as a function of θ for the three cases shown in Figure 16.

TABLE I

Type of metrons	Number of metrons	MEI coefficient a_3
sinusoidal	5	-0.4821+j0.8103
sinusoidal	500	-0.3027+j0.0520
g^*	5	-0.2993+j0.0464

range of harmonics, we expect the g^* metrons to perform better than the sinusoidal metrons. The choice of metrons is really dependent on the geometry and excitation in the problem.

IV. CONCLUSION

In this paper, a theoretical foundation has been provided for the MEI. It was shown that the method is a local approx-

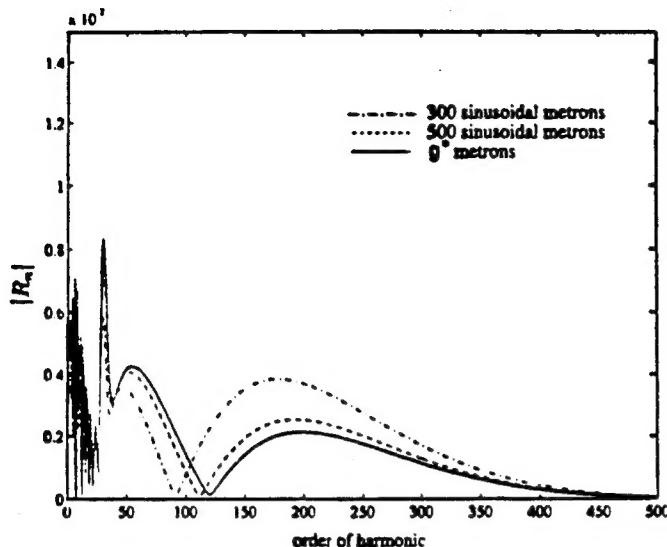


Fig. 18. Plot of $|R_{11}|$ for the case shown in Fig. 9, but using 300 harmonics, 500 harmonics, and the conjugates of Green's functions as metrons.

imate boundary condition. However, because this boundary condition incorporates geometrical information, it can be expected to produce better results than other local boundary conditions. A numerical study has been performed showing the influence that various parameters have on the MEI solution. The parameters include the electrical size of the scatterer, the distance between the mesh boundary and the scatterer, and the choice of metrons. The theoretical analysis has been verified by the numerical results. We have shown why the MEI method successfully handles current distributions that are not expressible as linear combination of metrons. We have also identified the major sources of error. It was shown that the performance of the boundary condition can be predicted before the actual problem is solved. We have also proposed a new set of metrons that gives the same results as those obtained using an infinite number of sinusoidal metrons.

The results presented here and in previous papers are only the initial work on this new method. Based on our experiences with this method, we believe that major improvements on the method can be made in the future.

REFERENCES

- [1] B. Engquist and A. Majda, "Radiation boundary conditions for the numerical simulation of waves," *Math. Comput.*, vol. 31, pp. 629-651, 1977.
- [2] A. Bayliss, M. Gunzburger, and E. Turkel, "Boundary conditions for the numerical solution of elliptic equations in exterior regions," *SIAM J. Appl. Math.*, vol. 42, pp. 430-451, 1982.

- [3] A. Chatterjee, J. M. Jin, and J. L. Volakis, "Edge-based finite element and vector ABC's applied to 3-D scattering," *IEEE Trans. Antennas Propagat.*, vol. 41, pp. 221-226, Feb. 1993.
- [4] A. F. Peterson, "Absorbing boundary conditions for the vector wave equation," *Microwave Opt. Tech. Lett.*, vol. 1, pp. 62-64, 1988.
- [5] J. P. Webb and V. N. Kanellopoulos, "Absorbing boundary conditions for finite element solution of the vector wave equation," *Microwave Opt. Tech. Lett.*, vol. 2, pp. 370-372, 1989.
- [6] P. Silvester and M. S. Hsieh, "Finite-element solution of 2-dimensional exterior field problems," *Proc. Inst. Elec. Eng.*, vol. 118, pp. 1743-1747, Dec. 1971.
- [7] D. R. Lynch, K. D. Paulsen, and J. W. Strohbehn, "Hybrid finite element method for unbounded electromagnetic problems in hyperthermia," *Int. J. Num. Meth. Eng.*, vol. 23, pp. 1915-1937, 1986.
- [8] K. K. Mei, "Unimoment method of solving antenna and scattering problems," *IEEE Trans. Antennas Propagat.*, vol. 22, pp. 760-766, Nov. 1974.
- [9] A. C. Cangellaris and R. Lee, "The bymoment method for two-dimensional electromagnetic scattering," *IEEE Trans. Antennas Propagat.*, vol. 38, pp. 1429-1437, Sept. 1990.
- [10] K. K. Mei, R. Pous, Z. Chen, and Y. W. Liu, "The measured equation of invariance: A new concept in field computation," in *Proc. Joint IEEE AP-S Int. Symp. and URSI Radio Science Meeting*, Chicago, July 1992.
- [11] A. C. Cangellaris and D. B. Wright, "Application of the measured equation of invariance to electromagnetic scattering by penetrable bodies," *IEEE Trans. Magn.*, vol. 29, Mar. 1993.

Jovan O. Jevtić (S'92) was born in Belgrade, Serbia, in 1970. He won the physics track championship of Yugoslavia in 1986. He received the Diploma degree in electrical engineering from the University of Belgrade in 1991.



fields, the high-voltage

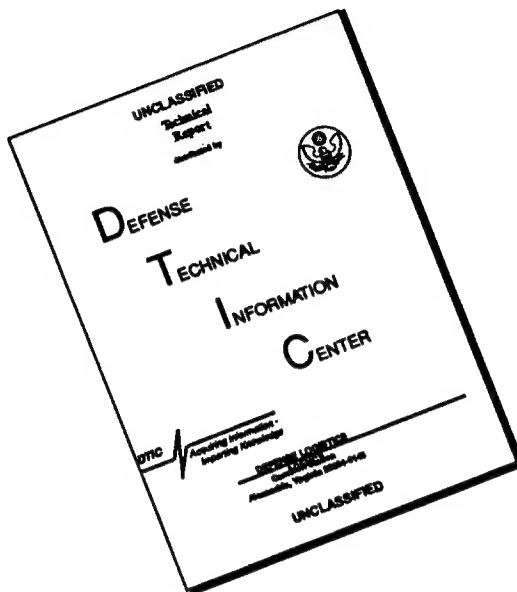
From March to September 1991 he worked as a Research Assistant in the Nikola Tesla Museum, Belgrade. He has been a Research Assistant in the ElectroScience Laboratory, Ohio State University, since March 1992. His major research interests are in the finite element analysis of electromagnetic and high-frequency phenomena, and the history of engineering.

Robert Lee (S'82-M'83-S'85-M'90) received the BSEE degree in 1983 from Lehigh University, Bethlehem, PA, and the MSEE and Ph.D. degrees in 1988 and 1990, respectively, from the University of Arizona, Tucson.

From 1983 to 1984 he worked for Microwave Semiconductor Corporation, Somerset, NJ. From 1984 to 1986, he worked at Hughes Aircraft Company, Tucson. From 1986 to 1990, he was a Research Assistant at the University of Arizona. In addition, during the summers of 1987 through 1989, he worked at Sandia National Laboratories, Albuquerque, NM. He is currently an Assistant Professor at Ohio State University, Columbus. His major research interests are in the development of finite element techniques for electromagnetic problems.



DISCLAIMER NOTICE



THIS DOCUMENT IS BEST
QUALITY AVAILABLE. THE COPY
FURNISHED TO DTIC CONTAINED
A SIGNIFICANT NUMBER OF
PAGES WHICH DO NOT
REPRODUCE LEGIBLY.